

First Measurement of Structure Dependent

$$K^+ \rightarrow \mu^+ \nu_\mu \gamma$$

Mark R. Convery

A DISSERTATION

PRESENTED TO THE FACULTY

OF PRINCETON UNIVERSITY

IN CANDIDACY FOR THE DEGREE

OF DOCTOR OF PHILOSOPHY

RECOMMENDED FOR ACCEPTANCE

BY THE DEPARTMENT OF

PHYSICS

NOVEMBER 1996

UMI Number: 9707305

UMI Microform 9707305
Copyright 1996, by UMI Company. All rights reserved.

**This microform edition is protected against unauthorized
copying under Title 17, United States Code.**

UMI
300 North Zeeb Road
Ann Arbor, MI 48103

© Copyright 1996 by Mark R. Convery.

All rights reserved.

Abstract

This thesis describes an experimental study of the decay $K^+ \rightarrow \mu^+ \nu_\mu \gamma$, which can proceed via two distinct diagrams. The first, called Inner Bremsstrahlung, is simply a radiative version of the familiar $K^+ \rightarrow \mu^+ \nu_\mu$ decay. Its branching ratio can be readily calculated in the Standard Model, and it has been well measured. The second diagram, called structure dependent, involves the emission of a photon from internal hadronic states, and is therefore much more difficult to calculate.

Observing decays due to this diagram would give important information on the structure of the K^+ and test models of low-energy QCD such as Chiral Perturbation Theory. Structure dependent decays may be distinguished from Inner Bremsstrahlung by the different spectra they produce, but to date, no structure dependent components have yet been observed. The previous best limit on the “SD⁺” component was $BR(\text{SD}^+) < 3.0 \times 10^{-5}$.

Using the E787 experiment at Brookhaven National Laboratory, which was designed to search for $K^+ \rightarrow \pi^+ \nu \bar{\nu}$, we have observed a structure dependent component in $K^+ \rightarrow \mu^+ \nu_\mu \gamma$ for the first time. Our branching ratio measurement is $BR(\text{SD}^+) =$

$(1.331 \pm 0.120 \pm 0.181) \times 10^{-5}$, where the first error is statistical and the second systematic. This corresponds to a measurement of the associated form factors of $|F_V + F_A| = 0.165 \pm 0.007 \pm 0.011$.

Acknowledgments

My wife, Wendy, is the one person who is most responsible for my finishing this thesis. Her patience and faith have been a constant source of strength and inspiration for me and I could not have done it without her. I hope someday to repay this mountainous debt of support, but with her competence and determination, I somehow doubt she'll ever need it.

The support of an incredible group of colleagues, whom I also call my friends, has likewise been essential. Peter Meyers always seemed to have the right idea at the right time. Stew Smith inspired through his sheer level of energy and enthusiasm. Mark Ito taught me about statistics as applied both to Physics and to Texas Hold 'em. Frank Shoemaker and Dan Marlow showed me the beauty of a well-designed instrument.

The time I've spent with my fellow students, Rob McPherson, Jesse Stone and Mehran Ardebili will, I'm sure, be what I remember most about Graduate School. While working on E787 is not quite akin to going to war, I think the feeling of camaraderie it engenders between its "foot soldiers" may be much the same.

I'd also like to thank the guys in the EP lab, who routinely went "beyond the call" on the Straw Chamber project. A lesser bunch could never have finished it.

Finally, I'd like to thank the rest of my family — my Mother, for holding an opinion of me that I hope someday to live up to; my Father, for teaching me to "do it right"; and my sisters, Kris and Linda, for telling me what I needed to know when I needed to know it.

We shall not cease from exploration, and the end of all our exploring will be to arrive where we started and to know the place for the first time. — T.S. Eliot

Contents

Abstract	iii
Acknowledgments	v
1 Introduction	1
1.1 Theoretical Considerations	4
1.1.1 Muon Decay	4
1.1.2 The Decay $K^+ \rightarrow \mu^+ \nu_\mu$	6
1.1.3 The Decay $K^+ \rightarrow \mu^+ \nu_\mu \gamma$	9
1.1.4 Form Factor Calculation— Chiral Perturbation Theory	13
1.2 Current Experimental Information on $K^+ \rightarrow \mu^+ \nu_\mu \gamma$	15
1.3 Measuring $K_{\mu\nu\gamma}(\text{SD}+)$	17
2 The E787 Experiment	20
2.1 E787 Overview	22
2.2 Kaon Production and Selection	24

2.3	Beam Line Instrumentation	27
2.4	The K^+ Stopping Target	29
2.5	Charged Track Measurement	32
2.5.1	The Drift Chamber	32
2.5.2	The Range Stack	35
2.6	Photon Measurement	37
2.6.1	The Barrel Veto	37
2.6.2	The Endcaps	38
2.6.3	Other Photon Vetoes	39
2.7	Trigger	39
2.7.1	The $K_{\mu\nu\gamma}$ Trigger	40
2.7.2	Monitor Triggers	43
2.8	Data Acquisition	44
2.9	The Data	44
2.10	Simulation	45
3	Event Reconstruction	48
3.1	Reconstruction Overview	49
3.2	Beam Reconstruction	51
3.3	Reconstruction of the Charged Track	52
3.3.1	The Drift Chamber	52

3.3.2	The Range Stack	53
3.3.3	The Target	56
3.3.4	Integration of Charged Track Information	58
3.4	Photon Reconstruction	60
3.4.1	Barrel Veto Z Measurement	61
3.4.2	Clustering	65
3.5	Final Kinematic Calibration	67
3.6	Charged Track Consistency	71
3.7	Muon/Photon Kinematics	72
3.8	Kinematic Fitting	73
3.8.1	Setting the Errors	75
3.8.2	Checking with $K_{\pi 2}$	75
3.9	Photon Vetoing	77
4	Background Rejection	80
4.1	Cut Definitions	81
4.2	Background Study Organization	81
4.3	Background Sources in the $K_{\mu\nu\gamma}$ Data Set	88
4.4	Accidental Background Study	91
4.4.1	Accidental Tagging	92
4.4.2	Accidental Rejection	95

4.4.3	Accidental Spectrum	100
4.5	π^0 Background Studies	101
4.6	No-Overlap Background Study	103
4.6.1	Photon Vetoing	103
4.6.2	Endcap Tagging — ECIN_REQT	107
4.6.3	Barrel Veto Tagging — BV_REQT	108
4.6.4	Mis-Tagging	109
4.6.5	No-Overlap Rejection	110
4.6.6	No-Overlap Spectrum	114
4.7	Overlap Background Study	116
4.7.1	Overlap Tagging	117
4.7.2	Mis-tagging	122
4.7.3	Overlap Rejection	123
4.7.4	Overlap Spectrum	123
4.7.5	An Amusing Aside — K_{e2}	125
4.8	Final Photon Energy Cut	128
4.9	Summary of Background Studies	128
4.10	Detailed Background Study Charts	129
5	Spectrum Analysis	138
5.1	Constructing the Final Spectrum	139

5.2	Opening Angle Fitting	141
5.3	Two Dimensional Fitting	146
5.4	Check of Inner Bremsstrahlung Branching Ratio	153
5.4.1	Calculation of $N_{K_{\mu 2}}$	155
5.4.2	Calculation of $A_{K_{\mu 2}, UMC}$ and $A_{IB, UMC}$	157
5.4.3	Check of Prescale Factor	158
5.4.4	Calculation of ϵ_{γ}	158
5.4.5	Calculation of IB Branching Ratio	159
5.5	Systematic Error	162
5.5.1	Charged Track	162
5.5.2	Photon Analysis	169
5.5.3	Background Subtraction	173
5.5.4	Binning	177
5.5.5	Photon Energy Cutoff	178
5.5.6	Summary of Systematic Errors	179
5.6	Conclusion	180
5.7	Detailed Cut Lists	181

List of Tables

2.1	Prescale factors and total number of events recorded for each of the three triggers used in the $K_{\mu\nu\gamma}$ analysis. Prescale factors include the “hardware” prescale of 16 applied in the prescale boards.	45
2.2	The number of Monte Carlo events generated and the number that passed the $K_{\mu\nu\gamma}$ trigger for each component of $K_{\mu\nu\gamma}$	46
3.1	Definitions of beam variables saved in the n-tuple.	51
3.2	Definitions of drift chamber variables saved in the n-tuple.	53
3.3	Definitions of Range Stack variables saved in the n-tuple.	56
3.4	Definitions of Target variables saved in the n-tuple.	58
3.5	Definitions of variables saved in the n-tuple from analysis combining results from the three charged track measuring detector components.	60
3.6	Definitions of variables saved for re-constructed Barrel Veto photons.	66
3.7	Kinematic correction factors for data and Monte Carlo. The smearing factor c is only applied to Monte Carlo data.	68
3.8	Table of peak positions and resolutions for data and UMC.	70

3.9	Definitions of variables saved for the kinematics of the μ^+ and photon.	72
3.10	Definitions of measured variables and their errors used in kinematic fitting.	74
3.11	Definitions of variables saved from kinematic fitting.	75
3.12	Definitions of second photon energy sums.	79
4.1	List of all cuts used in background rejection. The section in which the n-tuple variables involved in each cut are discussed is listed under "Ref."	82
4.2	List of tags used in background studies and cuts used in other parts of the analysis. The section in which the n-tuple variables involved in each cut are discussed is listed under "Ref."	83
4.3	Definitions of the four spectral regions and some of the sources of events in those regions.	90
4.4	Numbers inferred from Figure 4.5	94
4.5	Results from rejection branch of accidental background study. The number of events measured in each spectral region is shown. The expected number in each region after all cuts have been applied is obtained by multiplying by the N_R/N_e normalization. Regions do not sum to "Pre-spectrum" total, because events with EREG < 90MeV are not included in any of the regions. The "Reference" gives the table number in which the number was calculated.	102

4.6	Results from tagging branch of No-Overlap background study.	109
4.7	Results from mis-tagging study performed with $K_{\mu 2}(1)$ events including an estimate of the number of $K_{\mu\nu\gamma}$ events that will be mis-tagged and will end up in the regions 1 and 4.	111
4.8	Results from kinematic branch of No-Overlap background study. For each type of tagging the number of tagged events in each spectral region is shown. The expected number in each region after all cuts have been applied is obtained by multiplying by the N_R/N_ϵ normalization.	115
4.9	Results of CTEX tagging efficiency study	122
4.10	Results from mis-tagging study performed with $K_{\mu 2}(1)$ events including an estimate of the number of $K_{\mu\nu\gamma}$ events that will be mis-tagged.	123
4.11	Results from kinematic branch of overlap background study. For each type of tagging the number of events in each spectral region is shown. The expected number in each region after all cuts have been applied is obtained by multiplying by the N_R/N_ϵ normalization.	126
4.12	Summary of all background studies.	129
4.13	Setup cuts run on $K_{\mu\nu\gamma}$ triggers for all studies unless noted. Cuts are mostly of the “fiducial volume” type.	130
4.14	NOTPROMPT cut used to tag events where photon was not in time with charged track. The result is $N_{tag,acc}$	130

4.15	Cuts applied in rejection branch of Accidental study. Includes all cuts up to final spectrum cut. The result is $N_{pre-spec,acc}$.	131
4.16	Cuts applied for setup of “tagging” branch of No-Overlap study. $K_{\pi 2}(2)$ triggers were used. The result is N_{γ} .	132
4.17	Cuts applied to determine photon veto rejection. The result is N_R .	132
4.18	Setup cuts for No-Overlap mis-tagging study. $K_{\mu 2}(1)$ triggers are used. The result is $N_{K_{\mu 2},setup}$.	133
4.19	Accidental Photon Veto losses.	133
4.20	Cuts applied for setup of “rejection” branch of No-Overlap study. They are applied for both the Endcap and the Barrel Veto studies. The result is $N_{other,nov}$.	134
4.21	Pre-spectrum cuts for Endcap tagging.	134
4.22	Pre-spectrum cuts for Barrel Veto tagging.	134
4.23	Setup cuts applied to UMC events for Overlap tagging branch. Monte Carlo $K_{\pi 2}$ and $K_{\mu 3}$ events are used. The result is $N_{setup,ov}$.	135
4.24	Setup cuts applied to $K_{\mu 2}(1)$ events in Overlap mis-tagging study.	136
4.25	Cuts applied to tag overlap events. The result is $N_{tag,ov}$.	137
4.26	Pre-spectrum cuts applied to CTEX_REQT tagged events.	137
5.1	Constants used to convert fitted γ to SD^+ branching ratio.	145

5.2	COSOP Fitting Numbers. Note that BR(IB) is the theoretical value which is used as a normalization.	146
5.3	C and N_{gen} numbers used in two-dimensional fit.	150
5.4	Numbers extracted from the two-dimensional fit of Figure 5.8.	152
5.5	IB branching ratio calculation.	161
5.6	Measured SD^+ branching ratio for several different choices of binning of the final EREG_FIT vs. ETOT_TR histogram. The top entry is the nominal binning used in the branching ratio calculation.	177
5.7	Summary of systematic errors.	180
5.8	Cuts applied to produce final sample. The last two cuts are the final spectrum cuts in the photon energy EREG and the muon energy ETOT_TR.	182
5.9	Cuts applied to produce final UMC IB spectrum.	183
5.10	Cuts applied to produce final UMC SD^+ spectrum.	184
5.11	Cuts applied to produce final UMC INT^- spectrum.	185
5.12	Cuts applied to produce final UMC INT^+ spectrum.	186
5.13	Cuts applied to $K_{\mu 2}(1)$ monitors. The result is $N_{K_{\mu 2}}$	187
5.14	Cuts applied to UMC $K_{\mu 2}$ events that passed the $K_{\mu 2}(1)$ trigger. The result is $N_{K_{\mu 2}, UMC}$	188
5.15	Cuts applied to $K_{\pi 2}(2)$ monitor triggers for the photon efficiency check.	189

5.16 Cuts applied to UMC $K_{\pi 2}$ events that passed the $K_{\pi 2}(1)$ trigger for the photon efficiency check.	189
5.17 Effect of EREG2 cut on $K_{\pi 2}$ sample in data.	189
5.18 Effect of EREG2 cut on $K_{\pi 2}$ sample in UMC.	190
5.19 Effect of all photon cuts on $K_{\pi 2}$ sample in data.	190
5.20 Effect of all photon cuts on $K_{\pi 2}$ sample in UMC.	190
5.21 Cuts applied to $K_{\mu\nu\gamma}$ data as part of range counter thickness study. .	191

List of Figures

1.1	Feynman diagrams for $K^+ \rightarrow \pi^+ \nu \bar{\nu}$. The loop structure and the spectator role of the up quark are shown.	3
1.2	Feynman diagram for charged muon decay.	5
1.3	Proposed Feynman diagram for the decay $K^+ \rightarrow \mu^+ \nu_\mu$	7
1.4	Diagram for the decay $K^+ \rightarrow \mu^+ \nu_\mu$	8
1.5	Diagrams for $K^+ \rightarrow \mu^+ \nu_\mu \gamma$	9
1.6	Spectral shapes of $K^+ \rightarrow \mu^+ \nu_\mu \gamma$ components. The normalizations are arbitrary.	12
1.7	Theoretical muon momentum spectrum for different components of $K_{\mu\nu\gamma}$ and for $K_{\mu 3}$. Photon energy has been integrated up from 100 MeV. The relative normalization of the $K_{\mu\nu\gamma}$ components is set by assuming $F_V + F_A = F_V - F_A = 0.15$. The $K_{\mu 3}$ spectrum has been greatly suppressed.	18

1.8	Photon energy spectrum for different components of $K_{\mu\nu\gamma}$. μ^+ energy has been integrated from 137.0 MeV to 152.5 MeV. Normalization of components is set by assuming $F_V + F_A = F_V - F_A = 0.15$	19
2.1	Side (a) and end (b) views of the E787 detector. Only the top half of the detector is shown; it is actually azimuthally symmetric.	22
2.2	An end view of a typical $K_{\pi 2}$ event in the E787 detector.	24
2.3	Side view of E787 detector.	25
2.4	Layout of the C4-LESBIII beamline.	26
2.5	Schematic side view of Čerenkov counter. The path of light emitted by incident π^+ 's and K^+ 's is shown.	28
2.6	End view of the K^+ Stopping Target. The locations of the I- and V-counters are also shown.	30
2.7	Event display of typical event in the target. The first picture shows the energy measured in each fiber (in MeV) and the second picture shows the time measured in each fiber (in ns). Fibers belonging to the K^+ and μ^+ are readily distinguishable.	31
2.8	Side view of the Target, I- and V- counters. The K^+ beam enters from the left and charged decay products may exit the target through the I-counters. The active length of the I-counter is only 24.2 cm.	31
2.9	Design of the Ultra Thin Chamber.	33

2.10	End view of a typical track in the UTC. The small circles represent the isochrones of the anode wire hits. The large arc represents the best fit track tangent to each of the isochrones.	34
2.11	Schematic view of an RSSC.	36
2.12	Layout of CsI crystals in the Endcap Photon Veto	38
3.1	Diagram illustrating search order used in RD_TRK track finding. . . .	54
3.2	Diagrams describing SWATH Target analysis. Figure (a) shows use of the drift chamber track (shown as heavy curved line) to define a swath (shown as light curved line). Fibers identified as belonging to the K^+ are marked "K" and those belonging to the charged track are marked " π ." Figure (b) is a "blow-up" of the K^+ stopping region. The K^+ fibers at extreme clockwise and counter-clockwise positions, yet within the swath, are indicated by dots.	57
3.3	Illustration of the type of cosmic ray events used to measure the speed of light in the Barrel Veto.	62
3.4	End-to-end time difference measured in the Barrel Veto for cosmics of the type shown in Figure 3.3.	63
3.5	Measured z position of photons from $K_{\pi 2}$ in UMC and in data.	64

3.6	Event picture illustrating the BV cluster-finding procedure. The hatched counters have been grouped together into a cluster because they are contiguous. The unhatched counter has been left out of the cluster. The numbers indicate the visible energy in MeV in each counter. . . .	66
3.7	Line shapes of kinematic variables after final kinematic calibration. Note change in scale for $K_{\pi 2}$ photon energy.	69
3.8	Kinematic fitting histograms for fits of $K_{\pi 2}$ events. The first histogram shows the measured photon energy spectrum of the events that were used. The middle histogram shows the confidence level of the fit. The last histogram is a scatter-plot of the expected vs. measured ϕ -position of the second photon.	76
3.9	Event picture showing special excluded region in the Range Stack. Photon energy in the hatched region is added separately so that small amounts of splash back energy from the BV photon do not cause the event to be vetoed.	78
4.1	The simplest form of background study where one has two independent sets of cuts for rejecting the background.	84

4.2	Block diagram of “tagging” type background study. Study is composed of two branches — one finds the rejection for tagged events and the other finds the efficiency and rejection associated with the tagging method.	86
4.3	Flow chart defining background studies for $K_{\mu\nu\gamma}$ analysis.	89
4.4	Comparison of photon time distribution measured relative to the charged track time for $K_{\mu\nu\gamma}$ triggers and for lightly selected $K_{\pi 2}(2)$. A large accidental component is visible in the $K_{\mu\nu\gamma}$ triggers. The cuts defining the prompt window are shown.	92
4.5	The structure of the Accidental Background Study. Plot (a) shows the “rejection” branch of the study in which events tagged by NOT-PROMPT are used to measure the rejection of the rest of the cuts. Plot (b) shows the calculation of the efficiency of NOTPROMPT and the rejection of PROMPT. Single-hatched region indicates events that would be tagged by NOTPROMPT, and double-hatched indicates those that would not be cut by the PROMPT cut.	94
4.6	The time of a second beam particle measured in the Beam Wire Chamber shown relative to the charged track time and relative to the photon time. Cut positions are shown on the second plot.	96

4.7	Scatter plot of photon energy vs. photon z -position for events tagged as accidentals and passing Beam Wire Chamber cuts.	97
4.8	Histograms of photon shape variables used to distinguish accidentals from real photons. To be compared to Figure 4.9. The arrows show the cut positions.	98
4.9	Histograms of photon shape variables for real photons from $K_{\pi 2}(2)$ triggers. The arrows show the cut positions. While we do not know that the ZREG distribution will be the same for $K_{\mu\nu\gamma}$ as for $K_{\pi 2}$, we can at least see that there is a difference between real photons and the fake ones in Figure 4.8	99
4.10	Histogram of kinematic fit probability for tagged accidentals. Zero bin has been reduced to show other bins. Actual zero bin content is much higher.	100
4.11	Final spectra of surviving tagged events in the accidental background study. The first plot shows the charged-track kinetic energy and the second plot shows the photon energy versus the charged-track kinetic energy.	101
4.12	Chart describing No-Overlap background study. There are actually two independent studies being performed simultaneously — one employing an Endcap tag and the other a Barrel Veto tag.	104

4.13	Minimum possible photon energy is plotted as a function of momentum of the π^0 that produced the photon.	105
4.14	Energy and time of hits recorded in photon veto sub-systems for raw $K_{\mu\nu\gamma}$ triggers. Positions of time and energy windows are indicated. . .	106
4.15	Histograms of kinetic energy and momentum for EC tagged events. Note the cutoff at ETOT_TR=134 MeV and large momentum tails. . .	113
4.16	Histograms of confidence level for momentum energy comparison and for kinematic fitting for EC tagged events.	113
4.17	Final Spectra of surviving tagged events for the No-Overlap background using Endcap tagging.	114
4.18	Final Spectra of surviving tagged events for the No-Overlap background using Barrel Veto tagging.	115
4.19	Event picture showing charged track excluded (CTEX) region. The unhatched counters show the charged track region, as determined by the RD_TRK algorithm and the hatched region indicates the CTEX region associated with it. In this event there was some energy in the CTEX region and so the event would be tagged by the CTEX.REQT cut.	118

4.20	Chart describing Overlap background study. Overlap events are tagged by requiring energy in the CTEX region. The efficiency of this tag and the rejection obtained by vetoing on energy in the CTEX region is measured with Monte Carlo.	119
4.21	Histograms of the two variables used in overlap tagging. CTEX_ENER is the energy in the CTEX region and CTEX_TIME is the average time of this energy.	120
4.22	Spectra of tagged events in overlap background study.	121
4.23	Histograms of variables with high rejection for CTEX tagged events. PHO_CHISQ measures deviations from the expected $\frac{dE}{dx}$ pattern within a charged track. PRB_COM compares the momentum and kinetic energy measurements. PRB_MGN is the confidence level of a fit to a $K_{\mu\nu\gamma}$ hypothesis. Cut positions are indicated.	124
4.24	Histograms of PHO_CHISQ, PRB_COM, for $K_{\mu 2}(1)$ events. To be compared to Figure 4.23.	124
4.25	Final spectrum from overlap background study.	125
4.26	Momentum spectrum at different stages of the K_{e2} analysis. Last histogram shows prominent K_{e2} peak.	127

4.27	Measurement of threshold of BVHI trigger bit as a function of the measured photon energy. The arrow indicates the position of the EREG_FIN cut, which is set so that the BVHI bit is fully efficient.	129
5.1	Event sample after applying all cuts except the final spectrum cuts. .	140
5.2	Cosine of opening angle between muon and photon (COSOP) for UMC simulated IB and SD ⁺ components of $K_{\mu\nu\gamma}$ in spectral regions 1 and 4.	142
5.3	COSOP distributions for raw data, the sum of the backgrounds, and background subtracted data.	142
5.4	Fits of the data COSOP distribution to UMC generated distributions. The first plot uses only the Inner Bremsstrahlung component. The second plot uses both an IB and an SD ⁺ component.	144
5.5	COSOP distributions generated by UMC for SD ⁺ and INT ⁻ . Distributions are quite similar in appearance.	147
5.6	EREG_FIT vs. ETOT_TR distributions for UMC generated IB, SD ⁺ , INT ⁻ and INT ⁺ components.	148
5.7	EREG_FIT vs. ETOT_TR distributions for background subtracted data, No Overlap background, Accidental background and Overlap background.	148

5.8	χ^2 contours for the two-dimensional fit. The first plot is of the whole range of plausible values of the form factors. Each contour represents 50 units of χ^2 . The second plot narrows the focus to the χ^2 minimum. In this plot, each contour corresponds to one unit of χ^2 . The one standard deviation uncertainty for $F_V + F_A$ and the 90% confidence limit for $F_V - F_A$ are shown.	151
5.9	Comparison of data spectrum to one composed of $K_{\mu\nu\gamma}$ components weighted by the values of $F_V - F_A$ and $F_V + F_A$ found in the fit to the EREG_FIT vs. ETOT_TR spectrum. In each case the solid histogram is the background-subtracted data and the dots are the $K_{\mu\nu\gamma}$ spectrum.	153
5.10	Structure of IB branching ratio calculation.	156
5.11	Study of relative efficiency of photon cuts as a function of energy. The first column shows raw EREG_CALC histograms for UMC and data. The second column shows the efficiency of the photon cuts as a function of EREG_CALC for UMC and data. The last plot in the first row compares the UMC EREG_CALC variable with the true photon energy in UMC. The last plot in the second row compares the efficiency of the photon cuts in UMC and data. The cuts are found to be 7.4 % less efficient in data than in UMC.	160

5.12	Plot (a) shows relative efficiency for three different decay modes as a function of range counter thickness. Plot (b) shows the stopping layer distribution for the three decay modes for a counter thickness of 1.90 cm.	165
5.13	Measured SD^+ branching ratio as a function of range counter thickness.	166
5.14	Stopping layer distribution for real $K_{\mu 2}$ events compared to UMC generated $K_{\mu 2}$'s at different range counter thicknesses. Solid histogram is data. First plot shows whole range of thicknesses checked. Second narrows down to region around 1.90 cm. All histograms are normalized to unit area.	168
5.15	Similar plots as in Figure 5.14 but with the additional requirement that the K^+ stop position be near the center of the Target.	169
5.16	Illustration of EREG_RAN technique of simulating a disagreement between UMC and real photon efficiency. The first plot shows the definition of ϵ for positive values and the second shows it for negative values.	171
5.17	The first plot shows the measured SD^+ branching ratio as a function of the photon spectrum shaping parameter ϵ . The second shows the χ^2 of the fit to the spectrum as a function of ϵ	171

5.18	Estimation of ϵ parameter. EREG.FIT is plotted for K_{π^2} events in data and in UMC. The third plot is the normalized data histogram divided by the normalized UMC histogram.	172
5.19	Sensitivity of measured SD^+ branching ratio to background weights. .	175
5.20	Systematic error associated with calculation of Accidental background weight. Expected number of accidental events in the prompt (hatched) region is calculated using a flat and parabolic extrapolation.	176
5.21	Measured SD^+ branching ratio using a number of different values for the minimum value of EREG. Note the suppressed zero of the y -axis. .	179

Chapter 1

Introduction

As the study of Particle Physics enters its second century, ¹ we find that the state of our understanding of fundamental particle interactions is at once stunningly complete and yet still unsatisfying. The “Standard Model” of particle interactions can accommodate all observed phenomena, yet requires many more arbitrary parameters than one would hope would be needed by a truly fundamental theory. As experimenters, our charge is to study the phenomena of particle interactions with ever increasing precision with the hope of finding phenomena that the Standard Model cannot explain. In this way, we hope to shine light on what lies beyond, or beneath the Standard Model.

It is hard to think of a technique that has been more successful in this regard than the study of Kaon decays. Kaons are mesons consisting of one strange quark and one “light” quark — an up or a down and therefore come in charged (K^+ and K^-) and

¹Taking the discovery of the electron as its starting point.

neutral versions (K^0 and \overline{K}^0). As the lightest of the flavored mesons, Kaons are easier to produce and their decays are simpler to interpret than their heavier cousins. These advantages have allowed their decays to be studied with unprecedented precision and this has led to numerous invaluable insights bearing directly on the Standard Model.

One of the most important of these insights involves the suppression of decays requiring “Flavor Changing Neutral Currents” (FCNC), such as $K^+ \rightarrow \pi^+ \nu \bar{\nu}$ and $K_L^0 \rightarrow \mu^+ \mu^-$. Historically, attempts to explain this suppression led to the GIM mechanism and the prediction of the charmed quark [1]. Currently, we take advantage of this suppression to study second order processes. Since the GIM mechanism forbids FCNC completely at first order and only partially at second order, studying decays that require FCNC allows us to study the loops of second order diagrams without fear of contamination from the first order. The diagrams for the $K^+ \rightarrow \pi^+ \nu \bar{\nu}$ are shown in Figure 1.1. Since these loops contain very massive particles, such as the top quark, we can essentially study very high energy phenomena using only comparatively low energy tools.

$K^+ \rightarrow \pi^+ \nu \bar{\nu}$ is an especially interesting FCNC decay because it involves only the heavy gauge bosons, which, due to their high mass, operate over distances short compared to the typical meson radius. This allows us to study the strange quark directly — the up quark only participates as a spectator. Calculation of the rate for the decay is thus free of uncertainties involved in including the effects of other

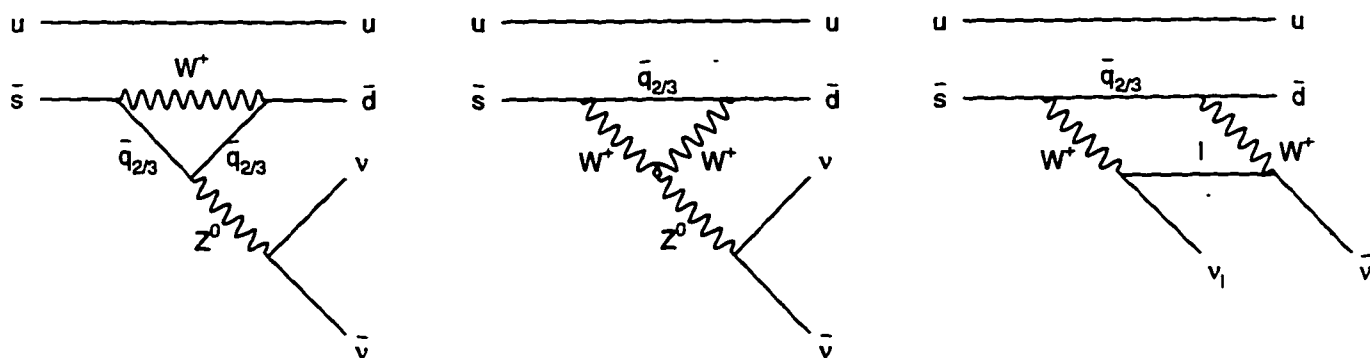


Figure 1.1: Feynman diagrams for $K^+ \rightarrow \pi^+ \nu \bar{\nu}$. The loop structure and the spectator role of the up quark are shown.

quarks. The price of this clean access to second order processes, however, is steep. The expected branching ratio for $K^+ \rightarrow \pi^+ \nu \bar{\nu}$ is very small — $\mathcal{O}(10^{-10})$ in the Standard Model.

About 10 years ago, the E787 experiment [2] was begun at Brookhaven National Laboratory (BNL) to look for $K^+ \rightarrow \pi^+ \nu \bar{\nu}$. This experiment would take advantage of the high flux of K^+ mesons available from the AGS to search for $K^+ \rightarrow \pi^+ \nu \bar{\nu}$ at levels approaching the Standard Model prediction. E787 has published a 90% confidence level upper limit of $BR(K^+ \rightarrow \pi^+ \nu \bar{\nu}) < 2.4 \times 10^{-9}$ from data taken in the years 1989 to 1991 [3]. It has also taken enough data to lower this limit by an additional factor of five in the years 1995 and 1996. This data is currently being analyzed.

While E787 was designed to study $K^+ \rightarrow \pi^+ \nu \bar{\nu}$, its capabilities are general enough and its K^+ flux is high enough to allow the study many other interesting decays of the K^+ [4, 5]. For this thesis, I will use data from the E787 detector. But, rather than

studying the strange quark directly, I will back up a step and look at the structure of the K^+ meson. I will do this through the study of the decay $K^+ \rightarrow \mu^+ \nu_\mu \gamma$, which I will call $K_{\mu\nu\gamma}$. The spectral shape of this decay will depend on the K^+ structure and therefore on the low energy structure of Quantum Chromodynamics (QCD). While such calculations are notoriously difficult, Chiral Perturbation Theory (χ PT) has recently shown great promise in providing a framework within which different low energy processes may be related to one another. The decay $K_{\mu\nu\gamma}$, with its non-hadronic final state, provides an especially clean testing ground for χ PT or any other theory that purports to predict low energy hadronic processes.

The rest of this chapter will contain a theoretical discussion leading to predictions of the shape of the spectrum of $K_{\mu\nu\gamma}$ as well as a description of general experimental considerations bearing on how one might go about measuring this spectrum. Subsequent chapters will describe the experimental apparatus of E787, and the data analysis that was applied to measure the $K_{\mu\nu\gamma}$ spectrum.

1.1 Theoretical Considerations

1.1.1 Muon Decay

As an introduction to the structure of weak decays, we can consider the simplest example — charged muon decay ($\mu^- \rightarrow e^- \nu_\mu \bar{\nu}_e$).² This decay illustrates many of the

²References [6] and [7] are used throughout this discussion.

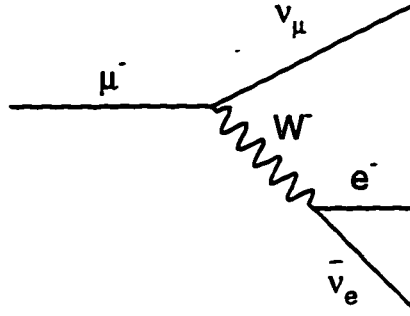


Figure 1.2: Feynman diagram for charged muon decay.

features common to all weak decays. The Feynman diagram for the decay is shown in Figure 1.2.

Using the Feynman rules as established for weak decays, the matrix element of this decay can be written:

$$\mathcal{M} = \left[\frac{-ig}{2\sqrt{2}} \bar{v}_{\nu_\mu} \gamma_\lambda (1 - \gamma_5) u_\mu \right] \left(\frac{g^{\lambda\sigma} - q^\lambda q^\sigma / m_W^2}{q^2 - m_W^2} \right) \left[\frac{-ig}{2\sqrt{2}} \bar{u}_e \gamma_\sigma (1 - \gamma_5) v_{\bar{\nu}_e} \right],$$

where \bar{v}_{ν_μ} , u_μ , \bar{u}_e , and $v_{\bar{\nu}_e}$ are spinors for the ν_μ , μ^- , e^- and $\bar{\nu}_e$; $q^\lambda = p_e^\lambda + p_{\bar{\nu}_e}^\lambda$; and m_W is the mass of the W^+ boson.

In muon decay, q^2 is much less than m_W^2 and so the propagator can be greatly simplified

$$\left(\frac{g^{\lambda\sigma} - q^\lambda q^\sigma / m_W^2}{q^2 - m_W^2} \right) \rightarrow -\frac{g^{\lambda\sigma}}{m_W^2}.$$

The matrix element then becomes

$$\mathcal{M} = \frac{G_F}{\sqrt{2}} \bar{v}_{\nu_\mu} \gamma_\lambda (1 - \gamma_5) u_\mu \bar{u}_e \gamma^\lambda (1 - \gamma_5) v_{\bar{\nu}_e},$$

with $G_F = \sqrt{2}g^2/8M_W^2$.³ This has the form of a current-current point interaction

$$\mathcal{M} = \frac{G_F}{\sqrt{2}} \mathcal{J}_{m\lambda} \mathcal{J}_e^{\lambda\dagger},$$

where $\mathcal{J}_{m\lambda} \equiv \bar{v}_{\nu_\mu} \gamma_\lambda (1 - \gamma_5) u_m$ is the “weak current” associated with the μ^+ . This is identical to an earlier form of the weak interaction suggested by Feynman and Gell-Mann, before the existence of the W^+ was even established.

Once the matrix element has been determined, the calculation of the branching ratio and spectrum are straightforward if somewhat involved.

1.1.2 The Decay $K^+ \rightarrow \mu^+ \nu_\mu$

We now wish to extend the ideas of the previous section to the decay $K^+ \rightarrow \mu^+ \nu_\mu$, called $K_{\mu 2}$.⁴ Since we know that a K^+ is composed of one \bar{s} quark and one u quark, it is tempting to use a diagram such as the one in Figure 1.3 and calculate in analogy with the previous section. Such a procedure would be incorrect, however, because the quarks in a K^+ are not free particles and cannot be represented by free-particle spinors. Rather, they are bound in the K^+ and are subject to the non-perturbative strong forces which bind them.

What is done instead is to use a diagram of the type shown in Figure 1.4. Where the “blob” represents the hadronic interactions leading to the emission of a virtual

³Experimentally, $G_F = 1.16639 \times 10^{-5} \text{ GeV}^{-2}$

⁴This theoretical analysis was first developed for the decay $\pi^+ \rightarrow \mu^+ \nu_\mu$ but it applies equally well to $K^+ \rightarrow \mu^+ \nu_\mu$ with only minor modifications.

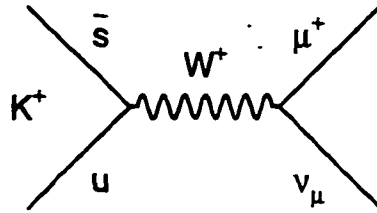


Figure 1.3: Proposed Feynman diagram for the decay $K^+ \rightarrow \mu^+ \nu_\mu$.

W^+ . We then return to the “current-current” interaction of the previous section.

$$\mathcal{M} = \frac{G_F}{\sqrt{2}} \mathcal{J}_{m\lambda} \mathcal{J}_h^\lambda,$$

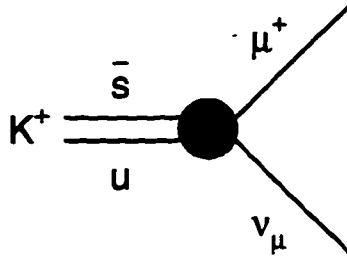
where, as before, $\mathcal{J}_{m\lambda} \equiv \bar{v}_{\nu_\mu} \gamma_\lambda (1 - \gamma_5) u_m$, and \mathcal{J}_h^λ represents the “hadronic current.”

We do not *a priori* know the form of this current, but we do know that it has to be a vector or axial-vector, since the matrix element must be a Lorentz scalar. The only four-vector available in the problem is q — the four-momentum of the K^+ . So, we can write the hadronic current as

$$\mathcal{J}_h^\lambda = V_{us} F(q^2) q^\lambda \equiv V_{us} F_K q^\lambda,$$

where $F(q^2)$ is some function of the only available scalar — q^2 . q^2 is just the K^+ mass, though, so $F(q^2)$ is called the K^+ decay constant F_K . The CKM matrix element V_{us} , which reflects the mixing of the mass eigenstates into the weak-interaction states, is separated from the decay constant by convention.

After squaring the matrix element and including the phase space factor, we find that the rate for the decay is given by

Figure 1.4: Diagram for the decay $K^+ \rightarrow \mu^+ \nu_\mu$.

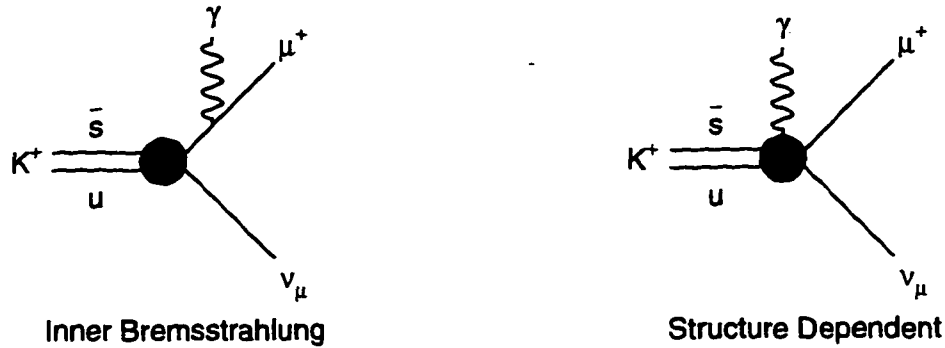
$$\Gamma_{K_{\mu 2}} = \frac{|V_{us}|^2 G_F^2}{8\pi} F_K^2 m_K m_\mu^2 \left(1 - \frac{m_\mu^2}{m_K^2}\right)^2.$$

By itself, this expression is not very useful, since we don't know the value of F_K .⁵

We can, however, check the validity of the expression by noting that the only change necessary to calculate the rate for the process $K^+ \rightarrow e^+ \nu_e$, called K_{e2} , is substitution of m_e for m_μ . We can then take the ratio of the rates for the two processes

$$\frac{\Gamma_{K_{e2}}}{\Gamma_{K_{\mu 2}}} = \frac{BR(K_{e2})}{BR(K_{\mu 2})} = \left(\frac{m_e}{m_\mu}\right)^2 \left(\frac{m_K^2 - m_e^2}{m_K^2 - m_\mu^2}\right)^2 = 2.449 \times 10^{-5}$$

Experimentally, this ratio is found to be $(2.45 \pm 0.11) \times 10^{-5}$, in excellent agreement with the theory [8].

Figure 1.5: Diagrams for $K^+ \rightarrow \mu^+ \nu_\mu \gamma$.

1.1.3 The Decay $K^+ \rightarrow \mu^+ \nu_\mu \gamma$

We now turn to the decay of interest for this thesis. The decay $K^+ \rightarrow \mu^+ \nu_\mu \gamma$ can proceed by either of the diagrams in Figure 1.5. The first diagram is called Inner Bremsstrahlung and is simply a radiative correction to the $K^+ \rightarrow \mu^+ \nu_\mu$ decay. It is completely calculable within the framework of Quantum Electrodynamics (QED). The second diagram, called structure dependent, involves the emission of a photon from internal hadronic lines and is therefore not directly calculable.

However, we can return to the idea of a hadronic current from the previous section as a way to analyze it. We will again construct a hadronic current from the available 4-vectors. In this case we have considerably more freedom in constructing the current than we did for $K^+ \rightarrow \mu^+ \nu_\mu$. The available 4-vectors are the K^+ momentum (p_K^μ), the γ momentum (k^μ) and the photon polarization (ϵ^μ). The only scalar available is

⁵In fact, this expression could be taken as a *definition* of F_K . Using the experimental value of $\Gamma_{K_{\mu 2}} = 3.379 \times 10^{-17}$ GeV, one finds $F_K = 159.8 \pm 1.4 \pm 0.44$ MeV, where the first error is due to the uncertainty on $|V_{us}|$ [8].

$q^2 = (p_K - k)^2$. It can be shown that the most general hadronic current does not contain arbitrary combinations of these vectors, but rather has the form [9, 10]

$$\mathcal{J}_h^\lambda = \frac{eV_{us}}{m_K} \epsilon_\nu^* [F_V(q^2) \epsilon^{\lambda\nu\alpha\beta} p_{K\alpha} k_\beta + iF_A(q^2) (g^{\lambda\nu} (p_K \cdot k) - k^\lambda p_K^\nu)],$$

where $F_V(q^2)$ and $F_A(q^2)$ are two form factors related to the vector and axial part of the current. While in principle they can depend on q^2 , I will treat them as constants for simplicity's sake. As we will see in the section 1.1.4, there is good theoretical reason to believe they should be approximately constant.

The structure dependent matrix element can then be written as before

$$\begin{aligned} \mathcal{M}_{SD} &= \frac{G_F}{\sqrt{2}} \mathcal{J}_{m\lambda} \mathcal{J}_h^\lambda \\ &= \left(e \frac{G_F}{\sqrt{2}} \frac{V_{us}}{m_K} \right) \epsilon_\nu^* [\bar{v}_{\nu\mu} \gamma_\lambda (1 - \gamma_5) u_m] [F_V \epsilon^{\lambda\nu\alpha\beta} p_{K\alpha} k_\beta + iF_A (g^{\lambda\nu} (p_K \cdot k) - k^\lambda p_K^\nu)]. \end{aligned}$$

This matrix element is then added to the one for Inner Bremsstrahlung to form the total matrix element for $K^+ \rightarrow \mu^+ \nu_\mu \gamma$

$$\mathcal{M}_{K_{\mu\nu\gamma}} = \mathcal{M}_{IB} + \mathcal{M}_{SD}.$$

Then, squaring the matrix element, summing over polarizations and integrating phase space leads to the following expressions for the differential rate for $K^+ \rightarrow \mu^+ \nu_\mu \gamma$ in the K^+ rest frame [11]: ⁶

$$\begin{aligned} \frac{d^2\Gamma}{dx dy} &= A_{IB} f_{IB}(x, y) + A_{SD} [(F_V + F_A)^2 f_{SD+}(x, y) + (F_V - F_A)^2 f_{SD-}(x, y)] \\ &\quad + A_{INT} [(F_V + F_A) f_{INT+} + (F_V - F_A) f_{INT-}], \end{aligned}$$

⁶We use the convention of the Particle Data Book, where the form factors F_V and F_A are dimensionless.

where

$$\begin{aligned}
 f_{IB}(x,y) &= \left[\frac{1-y+r}{x^2(x+y-1+r)} \right] \\
 &\quad \times \left[x^2 + 2(1-x)(1-r) - \frac{2xr(1-r)}{x+y-1-r} \right], \\
 f_{SD+} &= [x+y-1-r][(x+y-1)(1-x)-r], \\
 f_{SD-} &= [1-y+r][(1-x)(1-y)+r], \\
 f_{INT+} &= \left[\frac{1+y+r}{x(x+y-1-r)} \right] [(1-x)(1-x-y)+r], \\
 f_{INT-} &= \left[\frac{1+y+r}{x(x+y-1-r)} \right] [x^2 - (1-x)(1-x-y) - r],
 \end{aligned}$$

$$\begin{aligned}
 x &= \frac{2E_\gamma}{M_K}, \\
 y &= \frac{2E_\mu}{M_K}, \\
 r &= \left[\frac{M_\mu}{M_K} \right]^2, \\
 A_{IB} &= \Gamma_{K\mu^2} \frac{\alpha}{2\pi} \frac{1}{(1-r)^2}, \\
 A_{SD} &= \Gamma_{K\mu^2} \frac{\alpha}{8\pi} \frac{1}{r(1-r)^2} \left[\frac{M_K^2}{F_K} \right]^2, \\
 A_{INT} &= \Gamma_{K\mu^2} \frac{\alpha}{2\pi} \frac{1}{(1-r)^2} \frac{M_K^2}{F_K}.
 \end{aligned}$$

Note that the IB component contains no unknown factors. The spectral shape and the absolute rate are completely predicted. The structure dependent components, on the other hand, contain the unknown form factors F_V and F_A and so the absolute

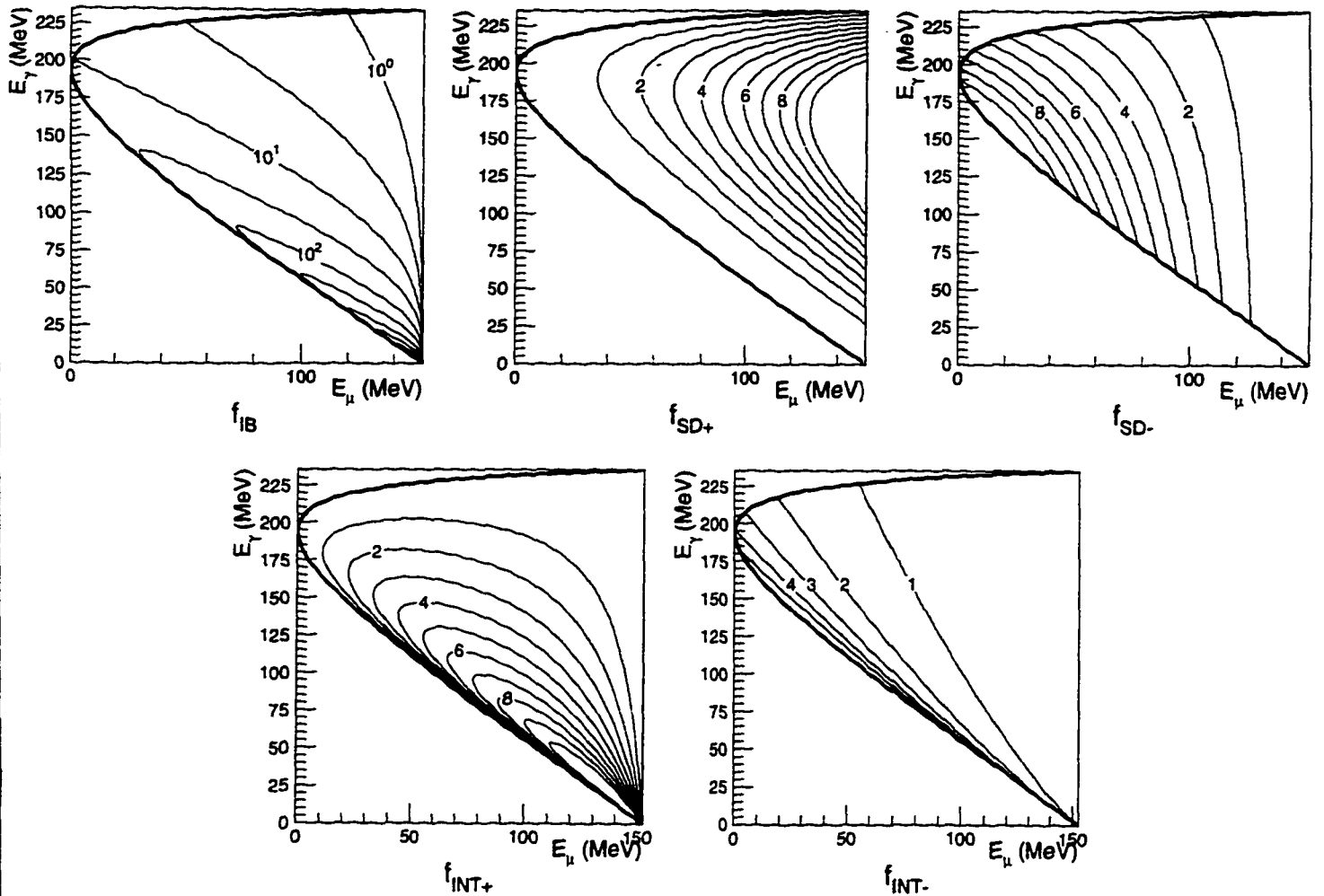


Figure 1.6: Spectral shapes of $K^+ \rightarrow \mu^+ \nu_\mu \gamma$ components. The normalizations are arbitrary.

rate is not predicted. If one neglects q^2 dependence of the form factors, however, the spectral shape of each of the components is predicted. Figure 1.6 shows these spectral shapes f_{IB} , f_{SD^+} , f_{SD^-} , f_{INT^+} and f_{INT^-} . The IB component is strongly peaked at high μ^+ and low γ energy, while the SD^+ component is peaked at high μ^+ energy and high γ energy.

1.1.4 Form Factor Calculation—Chiral Perturbation Theory

While the above analysis is quite general and depends only on very well accepted principles, such as Lorentz Invariance and conservation of electromagnetic current, it offers no prediction of the form factors F_V and F_A . Chiral Perturbation Theory (χ PT) provides a framework within which these form factors may be related to parameters of other processes. An effective Lagrangian of $\mathcal{O}(p^4)$ is defined that contains 12 undetermined coefficients L_1^r, \dots, L_{12}^r . The coefficients may be pinned down using a set of previously measured processes and then used to make predictions about other processes.

At $\mathcal{O}(p^4)$ of perturbation theory, there is no q^2 dependence of the form factors and no dependence on the mass of the strange quark. The predicted values of F_V and F_A are therefore the same for $K^+ \rightarrow \mu^+ \nu_\mu \gamma$ as for $\pi^+ \rightarrow e^+ \nu_e \gamma$, up to a factor of the meson mass. The form factors for $K_{\mu\nu\gamma}$ can be written in terms of renormalized versions of the L -coefficients (L_i^r) as [12]:

$$\begin{aligned} F_A &= -\frac{4M_K}{F_\pi}(L_9^r + L_{10}^r) \\ F_V &= -\frac{M_K}{4\pi^2 F_\pi} \\ \gamma &= \frac{F_A}{F_V} = 32\pi^2(L_9^r + L_{10}^r). \end{aligned}$$

F_V contains no unknown quantities, and γ has been measured in $\pi^+ \rightarrow e^+ \nu_e \gamma$ and found to be [8] ⁷

⁷This makes use of the Conserved Vector Current prediction $F_V = 0.0259 \pm 0.0005$

$$\gamma_{\pi e \nu \gamma} = 0.45 \pm 0.06$$

We therefore have

$$L_9^r + L_{10}^r = (1.42 \pm 0.19) \times 10^{-3}$$

The $\mathcal{O}(p^4)$ predictions for the $K_{\mu\nu\gamma}$ form factors and for the branching ratios of the associated components of $K_{\mu\nu\gamma}$ are therefore

$$F_V = -0.095 \pm 0.000$$

$$F_A = -0.043 \pm 0.006$$

$$F_V + F_A = -0.137 \pm 0.006$$

$$F_V - F_A = -0.052 \pm 0.006$$

where the errors shown come solely from errors on the experimental input.⁸ The corresponding branching ratios for each of the components are

$$BR(IB, E_\gamma > 20\text{MeV}) = 2.97 \times 10^{-3}$$

$$BR(SD^+, E_\gamma > 20\text{MeV}) = 9.22 \times 10^{-6}$$

$$BR(SD^-, E_\gamma > 20\text{MeV}) = 1.33 \times 10^{-6}$$

$$BR(INT^+, E_\gamma > 20\text{MeV}) = 1.40 \times 10^{-5}$$

⁸The errors shown are in fact somewhat smaller than are usually shown in theory papers, since they often include an estimate of the size of the corrections that will be found at higher order.

$$BR(\text{INT}^-, E_\gamma > 20\text{MeV}) = -3.74 \times 10^{-5}$$

Note that for negative values of $F_V - F_A$, the INT^- contribution to the differential rate is negative and the interference is *destructive*. This component could be said to have a negative branching ratio. For the INT^+ component, on the other hand, the spectral shape f_{INT^+} is negative throughout phase space, therefore for negative values $F_V + F_A$, the INT^+ causes *constructive* interference.

At higher order in perturbation theory, dependence on q^2 and m_s should appear. $\mathcal{O}(p^6)$ calculations have been completed for F_V [13], but not for F_A . These should be available soon, however, and the corrections coming from them could be as large as 30% [14]. The $\mathcal{O}(p^4)$ calculations should therefore be considered only a first approximation.

1.2 Current Experimental Information on $K^+ \rightarrow \mu^+ \nu_\mu \gamma$

Akiba *et al.* [11] have measured the branching ratio for $K^+ \rightarrow \mu^+ \nu_\mu \gamma$ going down to very low γ energies — a measurement which is therefore dominated by the IB component. The result is

$$BR(K^+ \rightarrow \mu^+ \nu_\mu \gamma, 214.5 < p_\mu < 231.5\text{MeV}/c) = (3.02 \pm 0.10) \times 10^{-3}$$

This agrees very well with the prediction for the IB component

$$\text{experiment/theory} = 0.991 \pm 0.013(\text{stat}) \pm 0.03(\text{syst})$$

Several experiments have tried to measure Structure Dependent $K^+ \rightarrow \mu^+ \nu_\mu \gamma$ [11, 15]. But so far, due to insufficient statistics, none has been successful. The best limits come from [11] which reports

$$BR(SD^+) < 3.0 \times 10^{-5}; \quad BR(SD^- + INT^-) < 1.3 \times 10^{-3}$$

In terms of these form factors, the limit becomes

$$M_K |F_V + F_A| < 0.23; \quad -2.5 < M_K (F_V - F_A) < 0.3$$

The related decay, $K^+ \rightarrow e^+ \nu_e \gamma$ has also been studied [16, 17]. The PDB reports a combined result for the form factors of [8]

$$M_K |F_V + F_A| = 0.148 \pm 0.010; \quad M_K |F_V - F_A| < 0.49$$

In the absence of q^2 dependence of the form factors, these should be directly comparable to those measured in the $K^+ \rightarrow \mu^+ \nu_\mu \gamma$ decay.

1.3 Measuring $K_{\mu\nu\gamma}(\text{SD}^+)$

While we would like to measure all of the form factors, including their signs, we are severely limited by background from other decays such as $K^+ \rightarrow \pi^0 \mu^+ \nu_\mu$ (called $K_{\mu 3}$). Since the π^0 in $K_{\mu 3}$ will immediately decay to two photons, the final state will appear similar to the final state of $K_{\mu\nu\gamma}$. The branching ratio of $K_{\mu 3}$ is 0.0318 compared to $\mathcal{O}(10^{-5})$ for the structure dependent $K_{\mu\nu\gamma}$ components and so $K_{\mu 3}$ can represent a significant background.

As can be seen in Figure 1.7, $K_{\mu 3}$ has an endpoint at a μ^+ momentum of 215.1 MeV/c, corresponding to a kinetic energy of 134.0 MeV. If we restrict our attention to the region above this endpoint, we will get a large amount of rejection for $K_{\mu 3}$. Of the structure dependent components, the SD^+ component is the most prominent in this high momentum part of the spectrum and will therefore be the easiest to observe. The INT^- and INT^+ components also extend into this region, but are somewhat smaller than the SD^+ component and are thus harder to identify. As we will see in later chapters, our sensitivity to these components is not nearly as good as for SD^+ . Since SD^+ depends on $(F_V + F_A)^2$, the only information we can hope to get about the form factors from this component is the absolute value of the sum $F_V + F_A$.

Another source of potential background is a $K_{\mu 2}$ decay accompanied by an accidental photon. This background is potentially severe and in previous attempts to find the structure dependent components it has caused experimenters to narrow the search

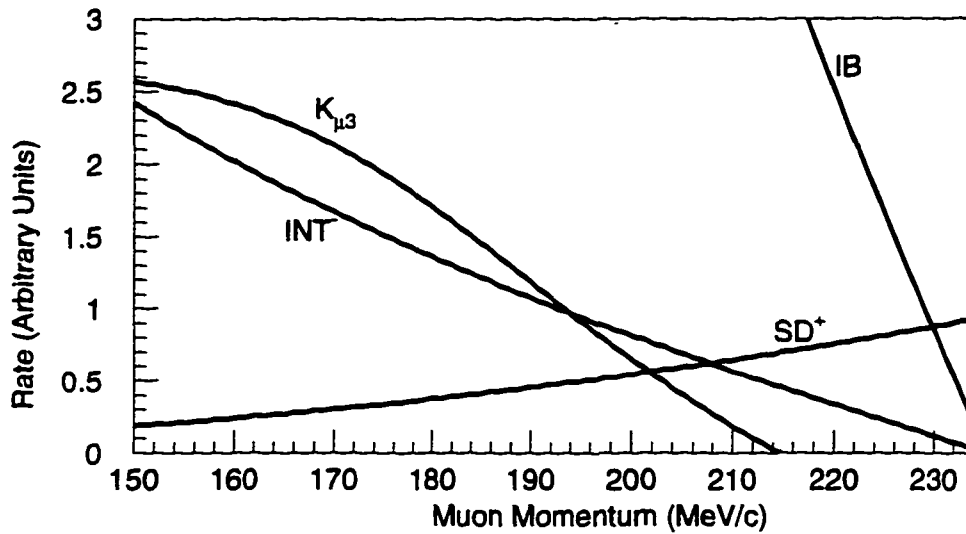


Figure 1.7: Theoretical muon momentum spectrum for different components of $K_{\mu\nu\gamma}$ and for $K_{\mu 3}$. Photon energy has been integrated up from 100 MeV. The relative normalization of the $K_{\mu\nu\gamma}$ components is set by assuming $F_V + F_A = F_V - F_A = 0.15$. The $K_{\mu 3}$ spectrum has been greatly suppressed.

region to the region between the $K_{\mu 3}$ endpoint and the $K_{\mu 2}$ peak [11]. Nonetheless, we will find that for our search we are able to use the region of phase space all the way up to the kinematic limit of the muon momentum. This is especially advantageous for measuring the SD^+ component since it peaks at that point.

Assuming that we can distinguish the $K^+ \rightarrow \mu^+ \nu_\mu \gamma$ events from all background sources, we will still have the problem of distinguishing the SD^+ component from the IB. This will be possible due to the higher photon energy of the SD^+ spectrum. This can be seen in Figure 1.8 which shows the photon spectrum for different components of $K^+ \rightarrow \mu^+ \nu_\mu \gamma$ when the μ^+ energy is integrated from a kinetic energy of 137.0 MeV to the kinematic limit at 152.5 MeV.

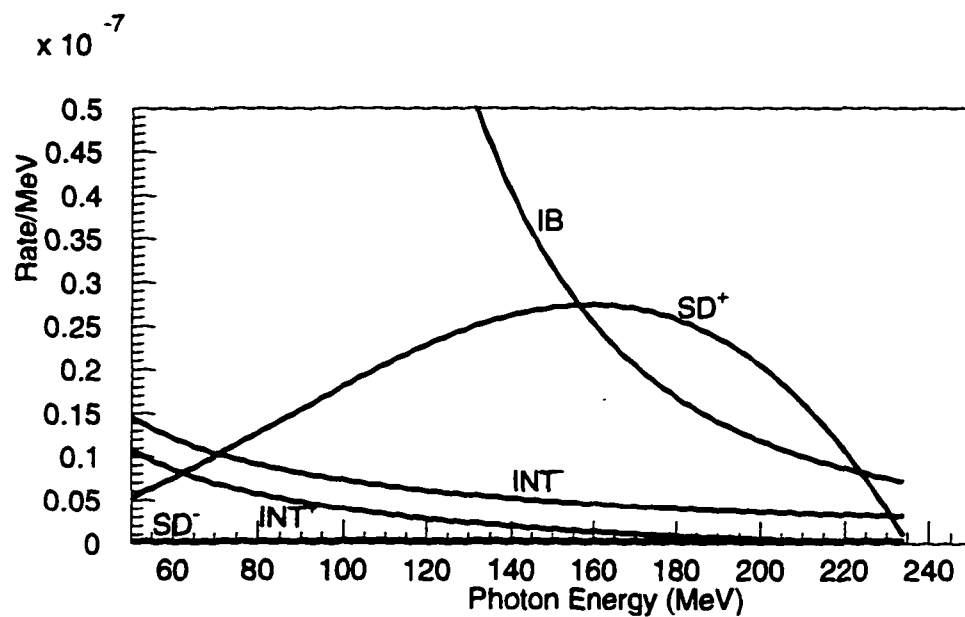


Figure 1.8: Photon energy spectrum for different components of $K_{\mu\nu\gamma}$. μ^+ energy has been integrated from 137.0 MeV to 152.5 MeV. Normalization of components is set by assuming $F_V + F_A = F_V - F_A = 0.15$.

The E787 Experiment

The E787 experiment was designed to search for the rare decay $K^+ \rightarrow \pi^+ \nu \bar{\nu}$. As we will see, however, it is also quite well suited to study $K^+ \rightarrow \mu^+ \nu_\mu \gamma$. Since the expected branching ratio for $K^+ \rightarrow \pi^+ \nu \bar{\nu}$ is $\mathcal{O}(10^{-10})$ times smaller than that of the backgrounds, the design of the experiment is driven by the need to reject these copious backgrounds while still maintaining reasonable efficiency for $K^+ \rightarrow \pi^+ \nu \bar{\nu}$.

The two main sources of background to $K^+ \rightarrow \pi^+ \nu \bar{\nu}$ are the decays $K^+ \rightarrow \mu^+ \nu_\mu$ and $K^+ \rightarrow \pi^+ \pi^0$ (called $K_{\pi 2}$). Both decays produce mono-energetic charged particles in the K^+ rest frame — the $K_{\mu 2}$ at a momentum of 235.5 MeV/c and the $K^+ \rightarrow \pi^+ \pi^0$ at 205.1 MeV/c. Rejection of both of these backgrounds can be achieved by restricting the search for $K^+ \rightarrow \pi^+ \nu \bar{\nu}$ to the kinematic region between the two peaks. Redundant measurement of the charged-track kinematics, i.e. its momentum, range and kinetic energy, gives information on the identity of the charged particle and protects against spurious measurements. Using a cylindrically symmetric geometry and only

measuring charged tracks in the “central region,” greatly simplifies the construction. Since the π^0 decays immediately to two photons, further rejection of $K_{\pi 2}$ background can be achieved by vetoing on any energy arising from photons.

These considerations suggest the following set of guidelines for the design of E787:

- Maintain the mono-energetic nature of the $K_{\mu 2}$ and $K_{\pi 2}$ backgrounds by bringing the K^+ beam to rest at the center of the detector.
- Measure the momentum, range and kinetic energy of the charged decay products in a 2π solid angle central region.
- Surround the central region with a highly-segmented 4π photon detector.

These guidelines turn out to be almost exactly the same as one would follow were one to build a detector to study $K_{\mu\nu\gamma}$. The stopped K^+ requirement and the redundant measurement of the charged-track kinematics are effective in maintaining a clean endpoint for $K_{\mu 3}$ decays. The 4π photon detector is useful both for measuring the single photon from $K_{\mu\nu\gamma}$ and for vetoing on second photons from events containing π^0 's. These features, combined with the high data rates of which E787 is capable, make the E787 experiment an ideal place to study $K_{\mu\nu\gamma}$.

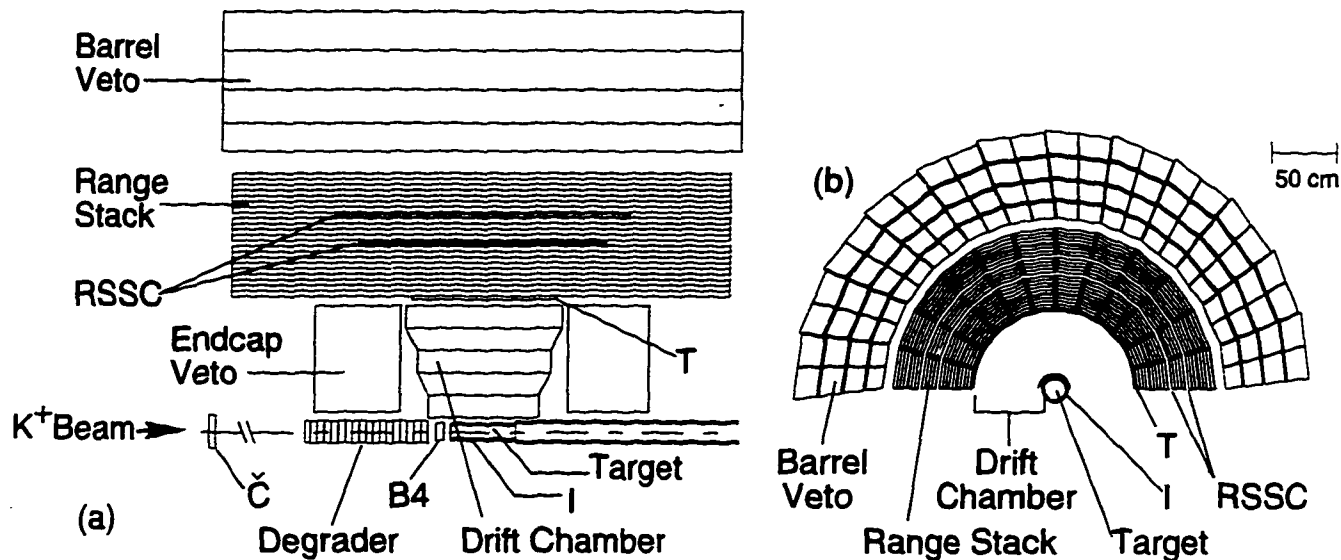


Figure 2.1: Side (a) and end (b) views of the E787 detector. Only the top half of the detector is shown; it is actually azimuthally symmetric.

2.1 E787 Overview

Figure 2.1 shows schematic side and end views of the E787 detector. As an introduction to the E787 detector, let me briefly discuss each of the components shown in those views.

The K^+ beam enters from the left of Figure 2.1(a). Its direction defines the z axis of the cylindrically symmetric detector. The properties of the beam are measured by the Čerenkov counter (Č) and the B4 counter. The beam is slowed down by the degrader and finally brought to a stop in the Target.

Charged decay products may then leave the target and those in the “equatorial” region of the detector pass through the I-counter. They then pass through the Drift Chamber, where their curvature due to an external magnetic field, and thus their

momentum, is measured. After the Drift Chamber, they enter the Range Stack, where almost all charged decay products of K^+ 's will come to a stop, thus allowing a kinetic energy and range measurement. The first layer of the Range Stack, called the T-layer, is shorter than the others and is used in conjunction with the I-counter to define the central region of the detector where charged tracks are measured. The Range Stack Straw Chambers (RSSC's) embedded in the Range Stack help to measure the total range. Dedicated photon detector systems are located in the Barrel region outside of the Range Stack and in the Endcap region. In the search for $K^+ \rightarrow \pi^+ \nu \bar{\nu}$ these photon detectors are used solely as photon-veto. In the $K_{\mu\nu\gamma}$ analysis, however, the Barrel Veto is used to measure the required photon.

A typical $K^+ \rightarrow \pi^+ \pi^0$ event is shown in Figure 2.2. Figure 2.3 shows a much more detailed view of the E787 detector, where the locations of the magnet coil and the phototubes of the various components are shown.

The rest of this chapter will describe the E787 detector in more detail. While this has been done previously in many different places, [2, 18, 19] the emphasis here will be on the elements that were important for the $K_{\mu\nu\gamma}$ analysis. Also, E787 has recently undergone an extensive upgrade in which many detector elements were replaced and this will be one of the the first descriptions of the new detector elements.

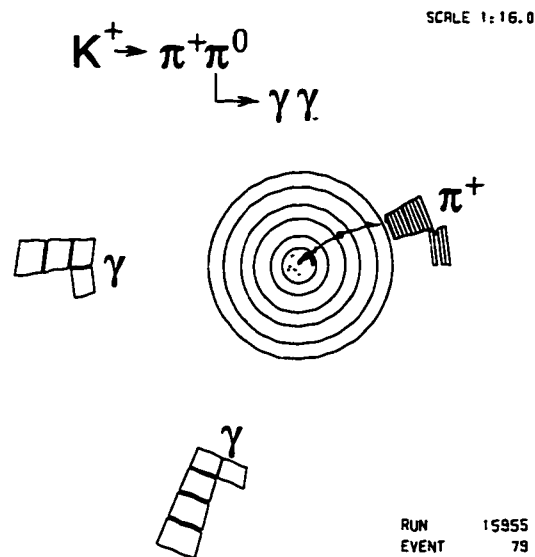


Figure 2.2: An end view of a typical $K_{\pi 2}$ event in the E787 detector.

2.2 Kaon Production and Selection

The E787 detector sits at the end of the C4-LESBIII beamline of the Alternating Gradient Synchrotron (AGS) at BNL. The purpose of the beamline is to produce a beam of K^+ mesons within a narrow momentum range and of high purity. Figure 2.4 shows the layout of the beam line. The 24 GeV proton beam of the AGS hits a Platinum production target and produces secondary particles at a wide variety of momenta and angles. Particles produced in a 12 msr angular region around the forward direction and in a 4% FWHM “momentum bite” around 800 MeV/c are brought into the beam line by the D1 magnet.

The particles then pass through a number of focusing and bending magnets, collimators, and two electrostatic separators. These separators use an electrostatic field, which causes different deflections for particles with the same momentum but with

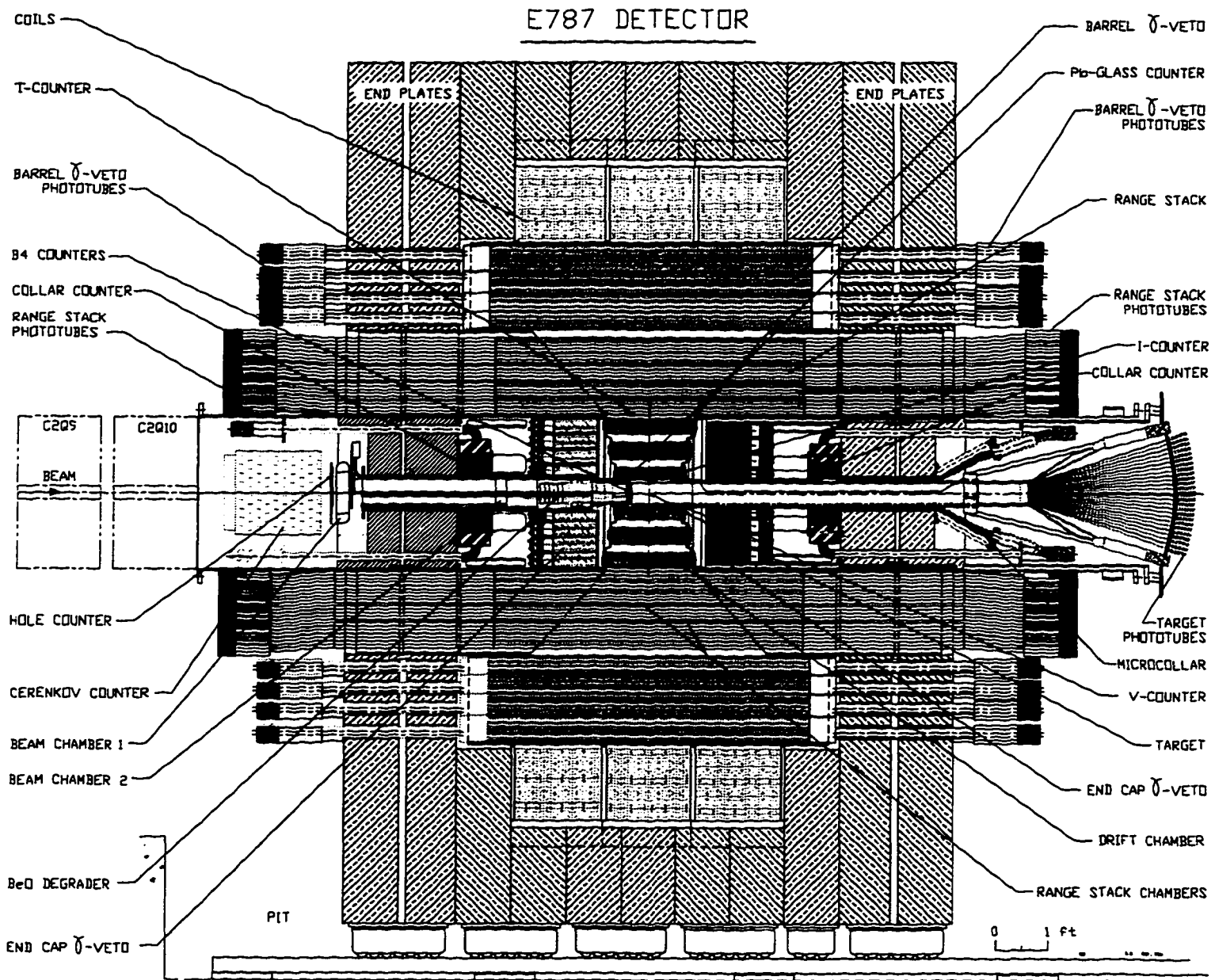


Figure 2.3: Side view of E787 detector.

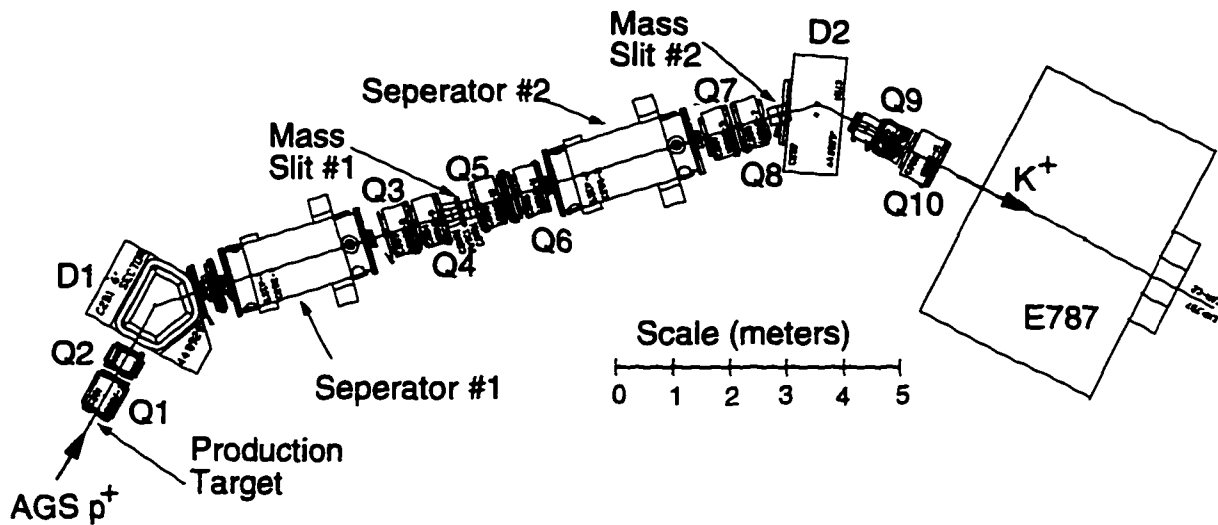


Figure 2.4: Layout of the C4-LESBIII beamline.

different mass. A “mass slit” follows each separator to select particles with the K^+ mass. In this way, it is possible to reject the much more copiously produced π^+ 's and protons and to produce a relatively pure beam of K^+ 's, which is then delivered to E787.

The AGS acceleration and extraction cycle takes approximately 3.4 seconds. Protons are delivered to the experiments during a 1.3 second “spill.” While the beamline is capable of accepting up to 2.0×10^{13} protons per spill, thus delivering about 10^7 K^+ 's to the experiment, the data for this thesis was taken at a somewhat lower rate of 7×10^{12} protons per spill resulting in about 1.2×10^6 K^+ 's delivered to the experiment. The purity of the beam was excellent — approximately 5 K^+ 's for every π^+ .

2.3 Beam Line Instrumentation

Although the beam is quite pure by the time it passes into the detector, it is still necessary to ensure that a given particle coming down the beam is a K^+ . It is also desirable to detect any second particles that come down the beam line in coincidence with the primary K^+ . These are the functions of the beam line counters, which are arranged between the last quadrupole magnet (Q10) and the stopping target where the K^+ 's are brought to rest. The configuration of the beam counters can be seen in Figure 2.3.

The first counter, at the far left of Figure 2.3 is the Čerenkov, which is used to determine whether an incoming particle is a K^+ or a π^+ . Figure 2.5 shows the operation of the counter schematically. The angle θ_C at which Čerenkov light is emitted from a charged particle is given by

$$\cos \theta_C = \frac{1}{\beta n}$$

where β is the velocity of the charged particle and n is the index of refraction of the material. The angle for particles of a given momentum therefore depends on the mass of the particle. The index of refraction of the radiator is chosen such that Čerenkov light from π^+ 's at the beam momentum is totally internally reflected and is transmitted efficiently to the Photomultiplier tubes (PMT's) labeled " π PMT." Čerenkov light from K^+ 's at the beam momentum is not totally internally reflected and is guided towards the " K PMT." By counting the number of struck tubes in each

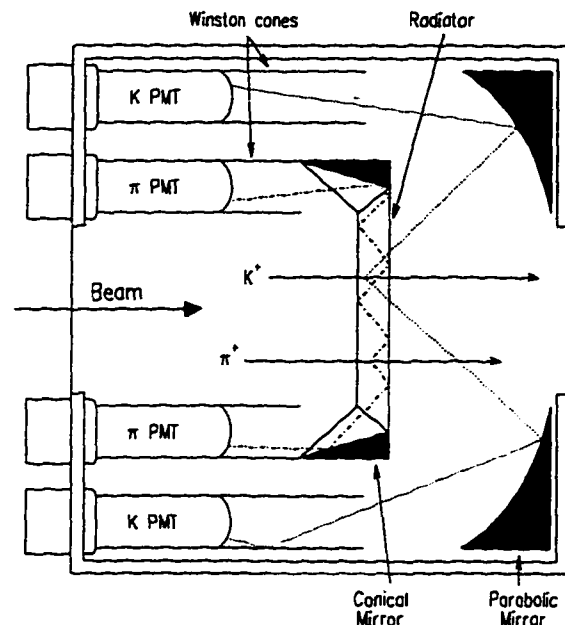


Figure 2.5: Schematic side view of Čerenkov counter. The path of light emitted by incident π^+ 's and K^+ 's is shown.

ring, one can unambiguously identify an incoming particle as π^+ or K^+ .

After the Čerenkov counter, the beam passes through two separate beam wire chambers (BWPC's), one located just after the Čerenkov counter and one located just before the degrader. Each of these chambers has three planes of wires at different orientations. The fine pitch of the wires allows one to identify events where there was an extra particle in the beam in coincidence with the primary K^+ .

The beam then passes through the degrader, where the energy of K^+ 's is reduced by ionization energy loss to a low enough energy that they will stop in the relatively short stopping Target. The degrader is composed of two parts. This first is made of Beryllium Oxide, a relatively dense material (3.0 g/cm^3), but with a low average atomic number to minimize multiple scattering. The second part is made of Lead

Oxide doped glass. This is instrumented with PMT's to allow detection of Čerenkov light. In principle, this can be used either to detect π^+ 's in the beam or to look for γ 's coming from the K^+ decay, although it is used for neither purpose in the $K_{\mu\nu\gamma}$ analysis. The B4 counter, a scintillator hodoscope located just after the degrader, is used in the trigger to detect those K^+ 's that made it through the degrader. Only about 20% of the K^+ 's that go through the Čerenkov make it into the Target.

2.4 The K^+ Stopping Target

After the B4 counter, the K^+ 's enter the stopping Target. The Target is made of 413 square scintillating fibers, 5mm on a side. There are also a small number of smaller fibers filling in the gaps around target edge, so that the overall shape is roughly circular. Scintillation light, produced in the fibers both by the stopping K^+ and any charged decay products, travels down the length of the fibers and outside the magnet. There, an array of PMT's detects the light, yielding time and energy information about each struck fiber. Figure 2.6 shows an end on view of the Target.

Figure 2.7 shows a typical event in the target. The fibers struck by the stopping K^+ have relatively large amounts of energy and occur at times close to 0.¹ Charged decay products, on the other hand, deposit energy at later times and, since they are lightly ionizing particles, at low energy. The analysis of the target data is described

¹This time is taken relative to the Čerenkov and is calibrated so that K^+ 's appear near $t = 0$.

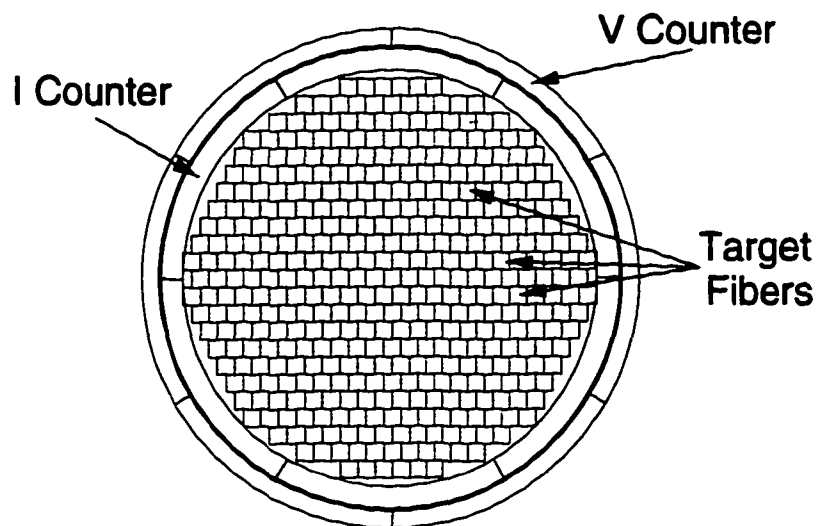


Figure 2.6: End view of the K^+ Stopping Target. The locations of the I- and V-counters are also shown.

in Section 3.3.3.

The I-counters surround the Target and are used primarily to define a fiducial region in z within which K^+ 's are allowed to decay. As shown in Figure 2.8, the I-Counters have an active length of only 24.2 cm. Seeing an I-Counter hit, therefore, ensures that the charged track is coming from the fiducial region of the target. The time of the charged track in the I-counter is used in the "Delayed Coincidence," which is a requirement that the time of the charged track be delayed from the time of the K^+ by at least 2 ns. Applying this requirement ensures that the K^+ came to a stop before decaying. Since the I-counters are rigidly attached to the Target, they are considered part of the Target system.

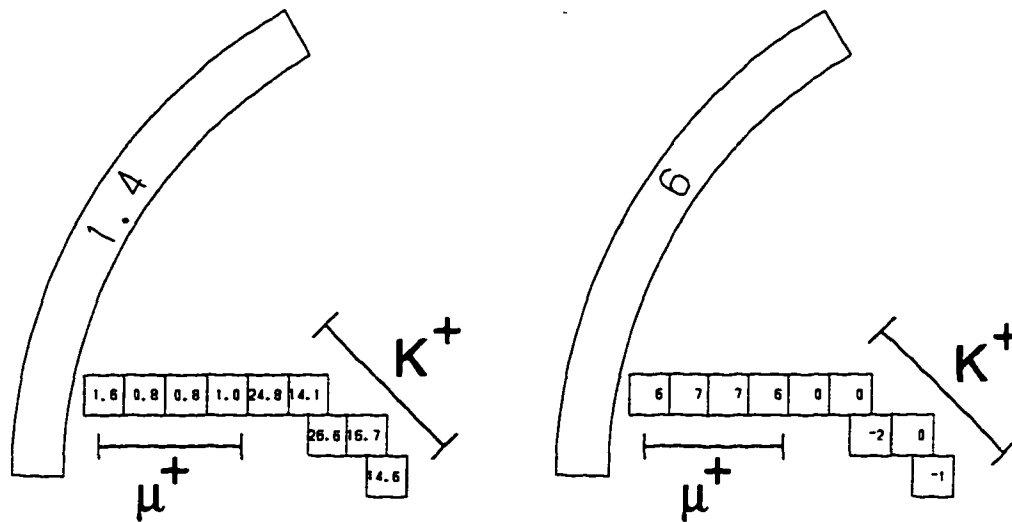


Figure 2.7: Event display of typical event in the target. The first picture shows the energy measured in each fiber (in MeV) and the second picture shows the time measured in each fiber (in ns). Fibers belonging to the K^+ and μ^+ are readily distinguishable.

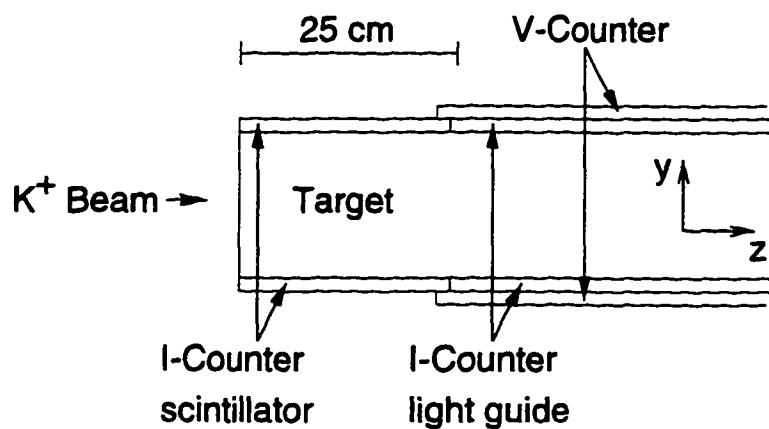


Figure 2.8: Side view of the Target, I- and V- counters. The K^+ beam enters from the left and charged decay products may exit the target through the I-counters. The active length of the I-counter is only 24.2 cm.

2.5 Charged Track Measurement

After charged decay products exit the Target, they may enter central region of the detector, which covers about half of the solid angle. In this region, the momentum, energy and range of the charged particles are measured. The redundancy of these measurements may be used to identify the type of particle and to provide protection against spurious measurements.

2.5.1 The Drift Chamber

The first detector that charged decay products encounter after leaving the Target is the Drift Chamber, which measures the curvature of charged tracks in the 1 Tesla magnetic field provided by the coil. The chamber, called the Ultra Thin Chamber (UTC), is composed of 5 superlayers separated by very thin ($25\ \mu\text{m}$) metallized kapton “foils,” which form concentric cylinders about the z -direction [20]. Figure 2.9 shows the design of the chamber. Three of the superlayers — the inner, the middle and outer — are “active” and are filled with an Argon/Ethane/Ethanol gas mixture. The other two are filled with a light, inert gas such as Nitrogen, to minimize multiple scattering. Each layer is held at a slightly lower pressure than the one inside of it, thus holding the foils rigid.

The active layers contain four layers each of drift cells. Each cell contains a $20\ \mu\text{m}$ anode wire at its center and $100\ \mu\text{m}$ cathode wires arranged so that the field

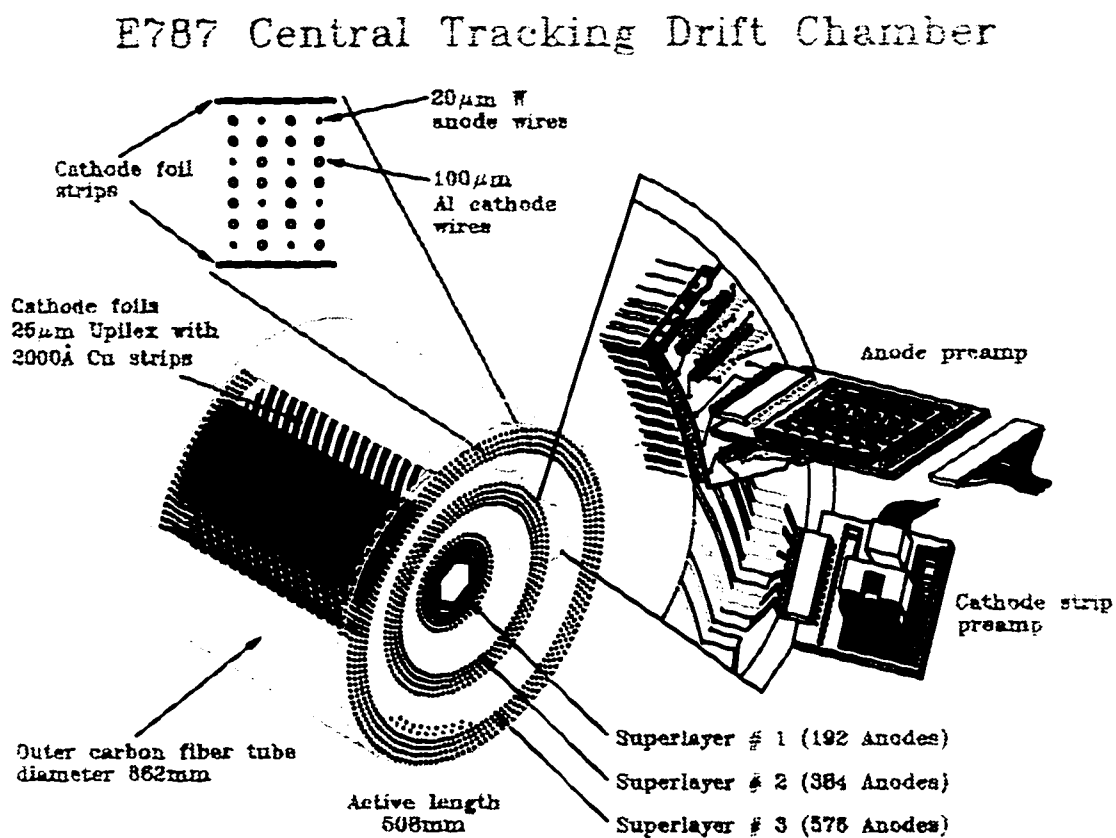


Figure 2.9: Design of the Ultra Thin Chamber.

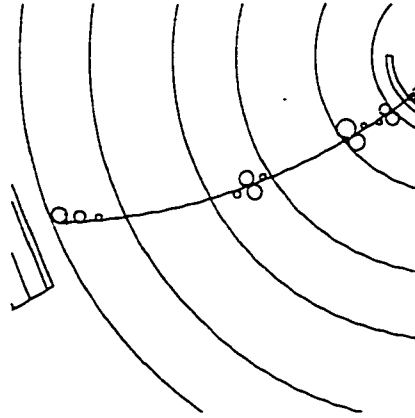


Figure 2.10: End view of a typical track in the UTC. The small circles represent the isochrones of the anode wire hits. The large arc represents the best fit track tangent to each of the isochrones.

at the anode is approximately radial. Ionization caused by charged particles passing through the active layers of the chambers drifts at an approximately constant velocity toward the anode wires under the influence of the radial field. Near the anode wire, the high electric field causes an avalanche multiplication of the charge resulting in a gas gain of approximately 10^5 . The relatively large signals thus induced on the anode wires are amplified and their time measured. A circular track can then be fit to the roughly circular “isochrones” representing the distance of closest approach of the track to each struck wire. Figure 2.10 shows such a fit for a typical event in the chamber. The radius of the fit track then measures the component of momentum in the plane perpendicular to the z -axis.

In order to measure the track in the z -direction, cathode strips are etched into the foils, on which the avalanches at the anode wire induce signals. The strips form helices centered around z -axis, and so knowledge of which strips were “hit” and which anode

wires caused the hit gives a measurement of the z -position of the track. A track can then be fit to the 6 z -measurements (one from each foil), and the dip-angle measured. This dip-angle is then combined with the radius of the fit track to give the measured momentum in the Drift Chamber.

2.5.2 The Range Stack

After the Drift Chamber, charged decay products enter the Range Stack (RS), which is composed of flat plastic scintillator counters. The counters are arranged in a cylindrical array with 24 sectors in the azimuthal direction and 21 layers in the radial direction. This segmentation can be seen in Figure 2.1. Each of the counters is approximately 1.90 cm thick and 182 cm long, except for those in the first layer (T-counters), which are 52 cm long and 0.64 cm thick. The T-counter length defines the accepted angular region for charged tracks and they are kept thin to minimize photon conversions in the first layer. The RS is thick enough that almost all charged decay products come to a stop in it, which allows for a “calorimetric” measurement of the kinetic energy of charged particles. The total range of the charged particles is also measured and gives, together with momentum and kinetic energy, a third measurement of the charged-track kinematics.

Scintillation light is piped out the ends of each counter and through the endplates of the magnet where it is detected by a PMT on each end of each counter. The

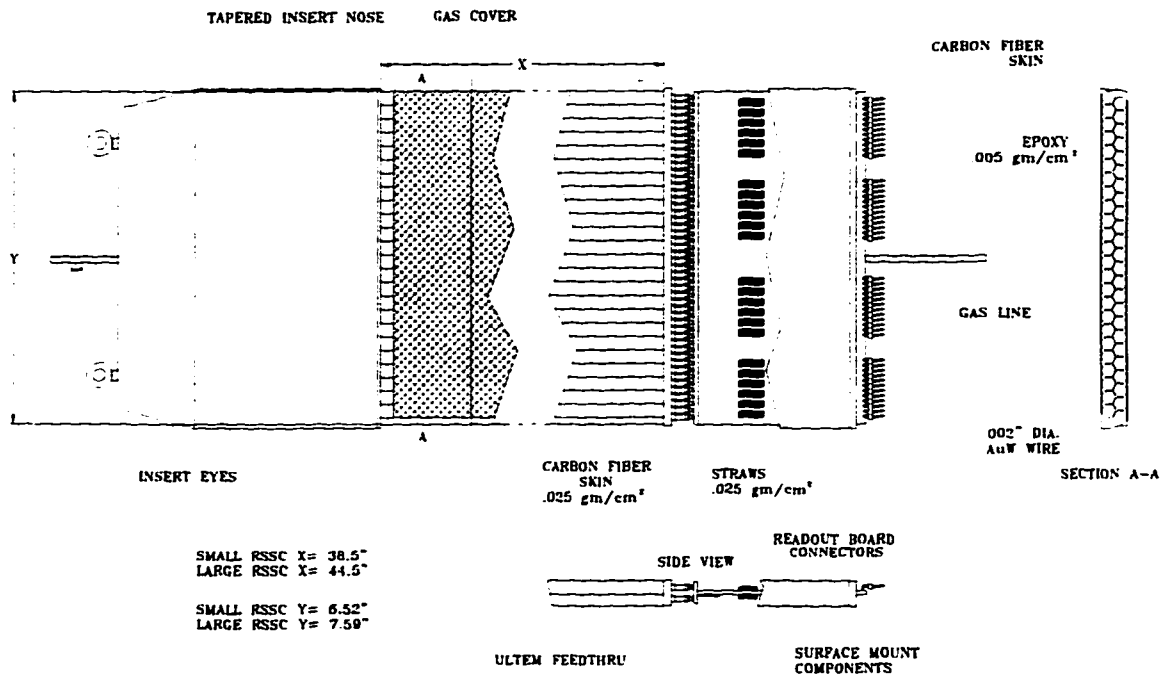


Figure 2.11: Schematic view of an RSSC.

signals from the PMT's are recorded using both 500 MHz Transient Digitizers (TD's) and integrating Analog to Digital Converters (ADC's). For the $K_{\mu\nu\gamma}$ analysis, the pulse-area from the ADC's is used to measure the energy deposited in each counter, and TD's are used only to measure the leading-edge time.

The Range Stack Straw Chambers (RSSC's) are embedded in each sector of the RS, after the 10th and 14th scintillator layers. The purpose of the RSSC's is to give a measurement of the position of the charged track, both in ϕ and in z , to aid in the measurement of total range. These chambers were designed to have very low mass, so that the amount of dead material that the charged particles see is minimized. Figure 2.11 shows a schematic view of the an RSSC.

2.6 Photon Measurement

The photon measuring system is composed of two major parts — the Barrel Veto (BV) and the Endcaps (EC). These systems were optimized for photon vetoing rather than for precisely measuring photon energies. However, in this analysis, we will find that the BV is also quite suitable for measuring photons.

2.6.1 The Barrel Veto

The BV lies just outside of the RS and is segmented into modules which are organized into 4 layers and 48 sectors, as shown in Figure 2.1. Each layer is made up of a lead-scintillator sandwich with approximately twenty layers of each in each module. The total thickness is equivalent to approximately 15 radiation lengths. Essentially, the lead serves to convert photons to electron pairs and *vice versa*, thus causing an electromagnetic shower. The scintillator “samples” this shower, and gives a measurement of the total energy in the shower. The resolution of this measurement, however, is limited by “shower fluctuations.” Most of the energy of the shower is deposited in the lead, so one must apply a correction to convert from energy observed in the scintillator to true measured energy. This “visible energy fraction” is about 0.3.²

Light from the scintillator is piped through the magnet in a similar way as for the RS, and detected with PMT's, one on each end of each module. Each PMT

²See Section 3.5 for more details

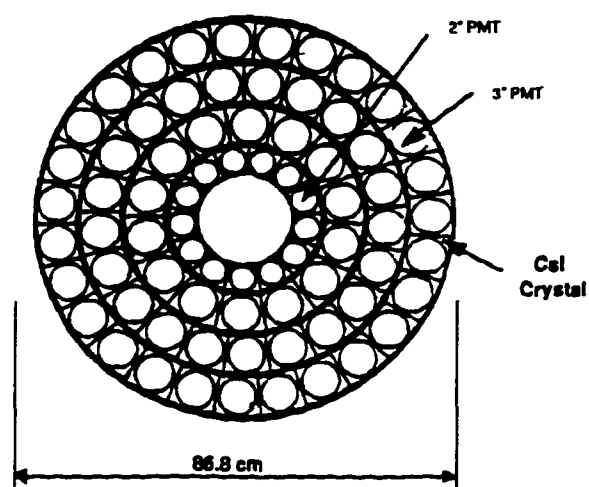


Figure 2.12: Layout of CsI crystals in the Endcap Photon Veto

is instrumented with ADC's and TDC's to allow measurement of pulse-area and leading-edge time.

2.6.2 The Endcaps

The two Endcaps abut the ends of the Drift Chamber as shown in Figure 2.1, and are composed of pure Cesium Iodide scintillating crystals [21]. The crystals in each endcap are arranged into four rings as shown in Figure 2.12. Since the radiation length of CsI is quite short (1.86 cm), the Endcaps require no extra converter material (e.g. the lead in the BV), and are therefore 100 % active. Rather than piping the light out of the magnet, "Fine-Mesh" PMT's are directly coupled to the crystals of the EC. Each of the PMT's is instrumented with a 500 MHz transient recorder made with a Gallium Arsenide Charge Coupled Device (CCD).

2.6.3 Other Photon Vetoes

Photons coming from decays of K^+ 's in the target can also convert and be detected in the Target or the Range Stack. Though these elements are designed for measuring charged tracks, they also detect photons with high efficiency. Since they are both highly segmented, the fibers or counters that were struck by the charged track can usually be distinguished from any that were struck by photons.

2.7 Trigger

In order to get to the desired levels of sensitivity to rare decay modes in a reasonable amount of time, it is necessary to examine several hundred thousand K^+ decays per spill. However, it is only possible to write to tape the data from several hundred events per spill. What is needed then, is a way to reject the vast majority of events before reading out their data. This is the role of the trigger. For $K^+ \rightarrow \pi^+ \nu \bar{\nu}$, with its poor experimental signature, a very sophisticated trigger with multiple levels is required. For $K_{\mu\nu\gamma}$, however, it is possible to get sufficient rejection using only the "Level 0" trigger.

For the Level 0 trigger, signals from the PMT's of the RS, the BV, the EC, and the beam system are "split" and a fraction of the charge is sent directly to the trigger. Another part of the charge goes through 375 ns delay lines before reaching the ADC's.

The Level 0 trigger decision based on the trigger signals must be made before the delayed signals reach the ADC's, and this sets a very stringent limit on the amount of time available for this decision. The information available is therefore limited to discriminated PMT signals, which are presented as "trigger bits." These bits can then be logically combined in any desired combination to form a trigger for a specific physics process.

2.7.1 The $K_{\mu\nu\gamma}$ Trigger

For the $K_{\mu\nu\gamma}$ trigger, the signal process has a high energy muon, a high energy photon and no other photons in the event. The muon is required to be in the central part of the detector and the photon is required to be in the Barrel Veto. The trigger is thus designed to have high efficiency for these type of events and low efficiency for all potential backgrounds.

The first trigger bit requires that a K^+ has come down the beam line and entered the target. This is known as the KB bit, and is formed by ANDing signals from the Čerenkov (CK), the B4 counter (B4) and the stopping Target (TTSum).

Next is the Delayed Coincidence bit (DC), which ensures that the K^+ came to a stop before decaying. It is formed by requiring that the I-counter came at least 2 ns later than would be expected from a prompt decay. This is done by comparing the I-counter time to the Čerenkov counter time after calibrating the I-counters so that

prompt events come at $t = 0$ ns.

The next two bits have to do with the charged track. The $T \bullet 2$ bit is set when there is a hit in the T-layer and in the second layer of the RS within one RS sector. This ensures that the charged track entered the Range Stack and is thus in the fiducial volume for charged track measurement. The charged track (CT) region of the RS is defined as the $T \bullet 2$ sector plus the next two clockwise sectors. This allows for track curvature in the RS. Note, however, that only clockwise curving, i.e. positive, tracks are properly treated by this. Each of the CT bits then indicates whether a given layer within this region was struck. For example, 9_{CT} indicates whether any of the layer 9 counters in the CT region were struck. For the $K_{\mu\nu\gamma}$ trigger, CT bits 6 through 16 were all required, which means that the charged track must penetrate at least to layer 16 of the RS, and is thus quite high energy. π^+ 's from $K_{\pi 2}$ only rarely go this deep, and only the highest energy part of the $K_{\mu 3}$ spectrum can go this far.

Analog energy sums are formed in each of the photon veto systems. The pulse height of this sum then roughly corresponds to the total energy deposited in that system. For the $K^+ \rightarrow \pi^+ \nu \bar{\nu}$ trigger, these signals are discriminated at quite low equivalent energy levels (≈ 5 MeV visible in the BV) and used as vetoes.³ For the $K_{\mu\nu\gamma}$ trigger, however, we require a photon in the Barrel Veto, so we discriminate the BV energy at a somewhat higher level (≈ 20 MeV visible) and use this as a *requirement* called BVHI.

³Recall that only about 30% of the energy deposited in the BV is "visible."

We also wish to *veto* on any extra energy in the BV, such as would come from a second photon from a π^0 . Essentially, we wish to count the clusters of photon energy in the BV and veto if there is more than one. We first sum the energy of adjacent BV sectors pair-wise and discriminate these signals at levels corresponding to approximately 10 MeV visible energy. This gives us 24 “sector-pair” signals which are put into a special “cluster counter” module (LeCroy MALU 4413). This module then gives a signal corresponding to the number of clusters of energy. If two neighboring sector-pairs are hit, it counts as only one cluster. If however, there are two non-adjacent sector-pairs hit, it counts as two clusters. The trigger bit NG2 is true if there were two or more clusters, and we veto on this occurrence.

Other bits used in the $K^+ \rightarrow \mu^+ \nu_\mu \gamma$ trigger include the EC bit which vetoes on energy in the Endcaps; the HX bit which vetoes on energy in the RS outside of the one- or two-hexant charged track region. A veto is also applied when there is any energy in the last layer of the Range Stack (layer 21). This bit, called $\overline{21}$ vetoes $K_{\mu 2}$ events where the μ^+ passes all the way through the RS, stops in the BV and thus satisfies the other trigger bits single-handedly.

The definition of the $K_{\mu\nu\gamma}$ trigger thus reads

$$KB \cdot DC \cdot T \bullet 2 \cdot \overline{EC} \cdot HX \cdot 6_{CT} - 16_{CT} \cdot BVHI \cdot \overline{NG2} \cdot \overline{21}$$

In a Monte Carlo simulation, the acceptance of the trigger was found to be 6.4% for $K^+ \rightarrow \mu^+ \nu_\mu \gamma (SD^+)$ and 1.7% for the IB component with $E_\gamma > 60\text{MeV}$ and $E_\mu >$

100MeV. In contrast, the acceptance for $K_{\mu 3}$ was 0.028%.

2.7.2 Monitor Triggers

In addition to the triggers designed to find the rare K^+ decay of interest, it is also useful to take data using simpler combinations of the trigger bits, called “monitor triggers.” The triggers are designed to give events which mostly come from a single one of the common decay modes of the K^+ , such as $K_{\pi 2}$. The data samples produced by these triggers are much purer samples of events of known origin than are produced by the rare decay triggers and are very useful for understanding the performance of the detector. For example, $K_{\pi 2}$ events can be used in assessing the photon veto efficiency. Since the branching ratios of the decays selected by the monitor triggers are known quite well, they can also be used as normalizations for the rare decays.

For the $K_{\mu\nu\gamma}$ analysis, the most important of the monitor triggers are $K_{\mu 2}(1)$, $K_{\pi 2}(1)$ and $K_{\pi 2}(2)$, defined as

$$K_{\mu 2}(1) = \text{KB} \cdot \text{T} \bullet 2 \cdot (6_{\text{CT}} + 7_{\text{CT}}) \cdot (19_{\text{CT}} + 20_{\text{CT}} + 21_{\text{CT}})$$

$$K_{\pi 2}(1) = \text{KB} \cdot \text{T} \bullet 2 \cdot (6_{\text{CT}} + 7_{\text{CT}}) \cdot \overline{(19_{\text{CT}} + 20_{\text{CT}} + 21_{\text{CT}})}$$

$$K_{\pi 2}(2) = \text{KB} \cdot \text{IC} \cdot \text{DC} \cdot \text{T} \bullet 2 \cdot (6_{\text{CT}} + 7_{\text{CT}}) \cdot \overline{(19_{\text{CT}} + 20_{\text{CT}} + 21_{\text{CT}})} \cdot \text{HX} \cdot \text{L1.1}$$

where the + indicates the logical OR of a number of conditions; IC is an I-counter requirement in addition to that already in the DC requirement; and L1.1 is a higher

level trigger which uses the Transient Digitizers to identify π^+ 's in the final state. As the names indicate, $K_{\mu 2}(1)$ selects mostly $K_{\mu 2}$ events and $K_{\pi 2}(1)$ and $K_{\pi 2}(2)$ select mostly $K_{\pi 2}$ events.

2.8 Data Acquisition

Once the trigger has indicated that a given event is to be recorded, the Data Acquisition system reads out the individual digitizing modules (ADC's, TDC's, TD's, etc.) and writes the data to 8mm magnetic tape [22]. For this data set, three data tapes were written in parallel for an output bandwidth exceeding 1 MByte/s.

2.9 The Data

The data for this thesis was taken during a very short run from July 22 to July 24, 1994. For this data set the $K_{\mu\nu\gamma}$ trigger was active as were several monitor triggers. The monitor triggers were prescaled by a large factor before being written to tape, since otherwise they would dominate the data stream. It is advantageous to record the monitor triggers at the same time as the rare decay triggers. That way, when they are used to assess the detector performance, any time-dependent changes will be automatically accounted for. The $K_{\mu 2}(1)$ and $K_{\pi 2}(1)$ data was taken at the same prescale throughout the run. Through an oversight, however, the $K_{\pi 2}(2)$ trigger was

Trigger	Prescale Factor	Events Recorded
$K_{\mu\nu\gamma}$	1	1517733
$K_{\mu 2}(1)$	20160	95115
$K_{\pi 2}(1)$	80000	17118
$K_{\pi 2}(2)$	640	34304

Table 2.1: Prescale factors and total number of events recorded for each of the three triggers used in the $K_{\mu\nu\gamma}$ analysis. Prescale factors include the “hardware” prescale of 16 applied in the prescale boards.

not turned on until about half way through the run. Due to the very short duration of the run, this is not expected to cause any serious problems.

The number of each type of trigger recorded during the $K_{\mu\nu\gamma}$ run is shown in Table 2.1. The run numbers were in the range 15865 to 15962, and the tape numbers were in the range 10177 to 10197. A total of 19 sets of tapes were used with two $K_{\mu\nu\gamma}$ tapes and one tape of monitor events in each set. There was also another data set taken on July 30 to July 31, 1994, but that data is not used here.

2.10 Simulation

The Monte Carlo program that is used to simulate the E787 detector is called UMC and is based on the EGS electromagnetic shower package [23]. K^+ decays with arbitrary final states can be generated and run through the detector simulation. The desired trigger is then applied to these events, and those that pass the trigger can be written to disk and saved. These events can then be run through the standard offline analysis,

$K_{\mu\nu\gamma}$ Component	Conditions	# Generated	# Triggers
IB	$E_\mu > 100 \text{ MeV}, E_\gamma > 20 \text{ MeV}$	8.390×10^6	142482
SD ⁺	$E_\gamma > 20 \text{ MeV}$	3.050×10^5	19343
INT ⁺	$E_\gamma > 20 \text{ MeV}$	4.932×10^6	50003
INT ⁻	$E_\gamma > 20 \text{ MeV}$	5.809×10^6	26536

Table 2.2: The number of Monte Carlo events generated and the number that passed the $K_{\mu\nu\gamma}$ trigger for each component of $K_{\mu\nu\gamma}$.

to be described in the next chapter, and the results compared to what is observed in real data.

In the $K_{\mu\nu\gamma}$ analysis, the most important application of UMC is the simulation of the different components of the $K_{\mu\nu\gamma}$ spectrum : IB, SD⁺, SD⁻, INT⁺ and INT⁻. Events of each type were generated according to the spectrum described by the f functions of Section 1.1.3. After the detector simulation, the $K_{\mu\nu\gamma}$ trigger as described above was applied and the events that passed written to disk. In Table 2.2 I tabulate the number of each component of $K_{\mu\nu\gamma}$ generated and the number that passed the trigger. Note that no SD⁻ events were generated, since that component is very small in the kinematic region of interest.

The $K_{\mu\nu\gamma}$ spectra were not generated over the whole accessible region of phase space, but only in the kinematic regions shown in the table. For example, the IB component was generated in the region $E_\mu > 100\text{MeV}, E_\gamma > 20\text{MeV}$. It is necessary to apply a minimum energy to the IB component because the spectrum diverges at very low γ energy. The E_μ condition was applied in order to speed up the simulation.

The validity of applying this condition was checked by running a large number of events without it in and verifying that very few events with $E_\mu < 100\text{MeV}$ passed the trigger.

A number of other “speed-ups” were put in place to minimize the CPU time required by the simulation. The μ^+ track was simulated first and if it did not cause a $T \bullet 2$, then the event was thrown away immediately without completing the simulation. This gives a good factor of speed improvement because the μ^+ simulation takes much less CPU time than the γ . Another speed-up involves throwing away immediately any events where the K^+ does not come to a stop. Even with these speed-ups in place, the IB data set took more than 30 CPU-days to complete on 200 Mhz R4400 processors.

A K^+ stopping distribution based on data taken in 1994 was used and the events were generated with nuclear and photo-nuclear interactions turned off, as these were not thought to be important for this analysis.

Event Reconstruction

The strategy for analysis of the $K_{\mu\nu\gamma}$ data is two-fold. First, methods have to be found to reject “background” events — i.e. those that passed the trigger described in Chapter 2.7.1, but were nonetheless not really $K_{\mu\nu\gamma}$. These methods will produce a list of “cuts” which when applied to the data will yield a sample of events which is free of background, or at least has understandable backgrounds. Second, the spectrum of events which are considered genuine $K_{\mu\nu\gamma}$, i.e. those which passed all the cuts, is analyzed to see if it is consistent with being only Inner Bremsstrahlung, or if a Structure Dependent contribution is present. In satisfying the first objective, it is important to keep in mind the second so that the resulting spectrum is not so “damaged” as to make it difficult to determine whether there is any structure dependent contribution.

In this Chapter, I will describe the methods that are used to reconstruct individual events and the event variables that are produced. In Chapter 4, I will describe

how cuts, based on these variables, are combined into “background studies” to provide estimates of the remaining backgrounds. Finally, in Chapter 5, I will take up the analysis of the events that remain after all background rejecting cuts have been applied.

3.1 Reconstruction Overview

The first step in the analysis of the data is the basic reconstruction of each event. This involves turning the raw digital data written onto the magnetic tapes during data taking into quantities useful for analysis such as charged track momentum. Once these higher level quantities have been calculated for each event, they are saved to disk in a form called an “n-tuple,” which is a data format defined by the CERNLIB HBOOK software package. An n-tuple consists of a list of variables describing each event. These might include things like the momentum and energy of the charged track.

Subsequent analysis is performed using *only* these n-tuple variables without ever referring back to the raw data. This style differs from previous analyses of E787 data, which reduced the data by cutting events in a multi-pass process. The advantage of the n-tuple method is that the CPU time required to analyze the n-tuple is approximately a factor of one hundred less than that required to analyze the raw data. The amount of disk space required to store events in n-tuple form is also approximately 100 times smaller — thus allowing the entire data sample to be stored on

disk. It takes only about 6 hours ¹ to run through the entire reconstructed data set. Background studies can thus be run on the entire data set rather than on separately selected data sets as is necessary in the multi-pass style of analysis.

The disadvantage of using the n-tuple method is that some information is necessarily lost in the reduction of the data to an n-tuple. Therefore, one must be careful to ensure that all of the necessary information is stored in the n-tuple and that the variables were calculated correctly. The goal of the reconstruction then, is the production of this n-tuple which represents each event as completely as possible.

The reconstruction is done with the help of a collection of subroutines written by the E787 collaboration called KOFIA. KOFIA version 2.0 was used for this analysis. KOFIA routines handle all of the most basic reading of data from tape and unpacking of data words into FORTRAN arrays. Also included in KOFIA are the reconstruction routines that were written by the experts on each particular component. These routines apply the relevant calibrations and do any required analysis before passing the results onto the user. Selected results are then saved in the n-tuple for later analysis. This often necessitates a change in the name of the variables. I will use the variable names that are used in the n-tuple. I will describe the reconstruction of the different detector components paying special attention to the variables which are saved in the n-tuple and are used in later analysis.

¹Conveniently, this represents a good night's sleep for a graduate student.

Variable	Definition
BW1TRS	Time of second beam particle in first BWPC
BW2TRS	Time of second beam particle in second BWPC

Table 3.1: Definitions of beam variables saved in the n-tuple.

3.2 Beam Reconstruction

For the purposes of the $K_{\mu\gamma}$ analysis, the primary use of the beam measuring elements is to ensure that no extra beam particles came into the detector in coincidence with the K^+ decay time. The main weapons that are used to detect this occurrence are the Beam Wire Proportional Chambers (BWPC's). The analysis of the chambers is done by a KOFIA subroutine called ANAL_BM. In each wire chamber, hits in the three planes are grouped by time to form "sets." Hits in at least 2 of the 3 planes are required to form a set. Normally, with only one K^+ in the beam line, there should be only one set in each chamber. If two or more sets were found in a chamber, then the set with time closest to the time of the original K^+ is removed from consideration. Of the remaining sets, the one whose time is closest to the to the time of the charged track in the Range Stack (TRS) is identified with a second beam particle. The time of this set relative to TRS is saved as BW1TRS for the first chamber and BW2TRS for the second. Finding a set in time coincidence with the charged track indicates that the track, or the photon, may have been caused not by the decay of the first K^+ but rather by a second particle.

3.3 Reconstruction of the Charged Track

The reconstruction of the charged track involves three separate detector components — the Target, the Drift Chamber (DC) and the Range Stack (RS). Before going into a more detailed discussion of the reconstruction of each component, it is helpful to have an overview of the whole procedure. The analysis proceeds by first fitting all the good tracks in the drift chamber. A single track is then found in the Range Stack and matched to a single DC track. The track is then extrapolated back into the Target to aid in the Target reconstruction. Calling of the charged track reconstruction routines and integration of the information from the three separate components is done by a routine called `SETUP_KINE`.

3.3.1 The Drift Chamber

The drift chamber analysis seeks to measure the charged track momentum and direction by fitting a helix to the space points measured on the strips and wires of the chamber. The first step is to measure tracks in the $x - y$ plane. Raw hits on neighboring wires in each super-layer are combined into “vectors” which give a rough estimate of the track direction in each superlayer. These vectors are then “linked” to try to form a track that passed through all three super-layers. Using the track found in this step as a seed, a χ^2 minimization procedure is used to find the final $x - y$ track parameters.

Variable	Definition
PDC	Momentum measured in the drift chamber
COS3D	Dip-Angle of charged track

Table 3.2: Definitions of drift chamber variables saved in the n-tuple.

The z -fit uses the the $x - y$ track parameters to convert struck foil strips into z positions. The z positions are then fit to a straight line as a function of the turning angle of the track. From this fit, the dip-angle of the track can be determined and the helix of the charged track is defined. The parameters of the track that are saved in the n-tuple are shown in Table 3.2. It is possible that several good charged tracks will be found in the drift chamber. For the purposes of this analysis, only one track is selected in a manner which will be described in the next section and the variables for that track are saved in the n-tuple.

3.3.2 The Range Stack

The first stage of the Range Stack reconstruction is a pattern recognition program called RD_TRK. RD_TRK looks for a single track in the Range Stack that follows a pattern of energy deposition that would be made by a single charged track. The track starts at the T • 2 closest in time to the Detector Strobe time. The counters surrounding the 2 counter are then searched for prompt hits and as soon as one is found, it is added to the track and made the “current counter.” The search order is

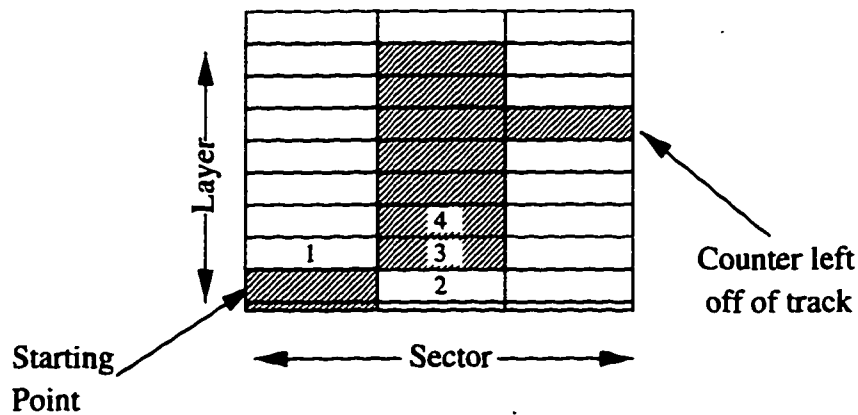


Figure 3.1: Diagram illustrating search order used in RD_TRK track finding.

shown in Figure 3.1, where the counters with prompt hits are shown hatched. The numbers in the counters indicate the order in which the counter is checked for a prompt hit. Thus, in this case RD_TRK will first look in the counter labeled "1" for a prompt hit. Failing to find one it will then look in the counter marked "2." Again failing it will look in the counter marked "3," where it will find a prompt hit and thus make it current counter. The procedure will then be repeated until no more counters can be found along the track. Note that this procedure will not put the counter in the third sector of Figure 3.1 on the track. Note also that the procedure is only capable of finding positive, i.e. clockwise curving tracks.

The layer of the last counter in the track is called the stopping layer and is saved as LAY. The energy of each counter is saved in the n-tuple as the array EMOD_RD and the times of the counters are combined to form a single "track time" (TRS), which is used as the main time reference for the rest of the analysis.

The Drift Chamber track that best lines up with the single RD_TRK track is

then selected. This DC track is extrapolated and used in conjunction with precise measurements of z and ϕ provided by the RSSC's to calculate the range in each counter and the total range of the track in the Range Stack. Corrections are made for dead material in the RS and total energy deposited in the RS, ERST is calculated.

The measured ranges in each layer were used to provide the dx to calculate the expected energy loss $\frac{dE}{dx}$ in each layer (EEXP) via the Bethe-Block equation for ionization energy loss. The EEXP array is then compared to the measured energy in each layer to reject events where the energy deposition pattern differs from what one would expect from a μ^+ simply coming to a stop. This could happen, for example, if a photon overlapped the charged track, thus depositing extra energy.

The comparison was done by adding up the expected and measured energies in each set of three consecutive layers and then forming a χ^2 out of their difference. The error used was proportional to the square root of expected energy in the three layers. The χ^2 starting at the i th layer is then written:

$$\chi^2_i = \frac{[\sum_{j=i}^{i+2} \text{EEXP}(j) - \sum_{j=i}^{i+2} E(j)]^2}{\sum_{j=i}^{i+2} \text{EEXP}(j)}$$

where $E(i)$ is the observed energy in the i th layer, derived from EMOD_RD. The largest χ^2_i was then saved as an n-tuple variable called PHO_CHISQ.

Variable	Definition
LAY	Stopping Layer
ERST	RS energy
TRS	Time as measured by the RS
NHITRD	Number of counters on the RS track
EMOD_RD(NHITRD)	Energy deposited in each counter of the track
PHO_CHISQ	Measures deviation from expected $\frac{dE}{dx}$

Table 3.3: Definitions of Range Stack variables saved in the n-tuple.

3.3.3 The Target

The first step in the Target analysis is to identify each of the struck fibers as coming from one of three sources: the K^+ , the outgoing charged track, or a photon. The Target analysis is called SWATH because it uses a “swath” defined by the drift chamber track to assist in identifying the charged track fibers [24]. SWATH is also given the time of the charged track in the Range Stack to help identify the charged track fibers. Figure 3.2(a) shows how the drift chamber track is used to define the swath. A likelihood analysis is then done on each fiber individually to identify which fibers were associated with the K^+ which with the charged track and which with any photon. In rough terms the assignments are as follows:

- Fibers with high energy and with times near to zero are identified as coming from the K^+ .
- Fibers with low energy, in time with the Range Stack time and on the swath are identified as coming from the charged track.

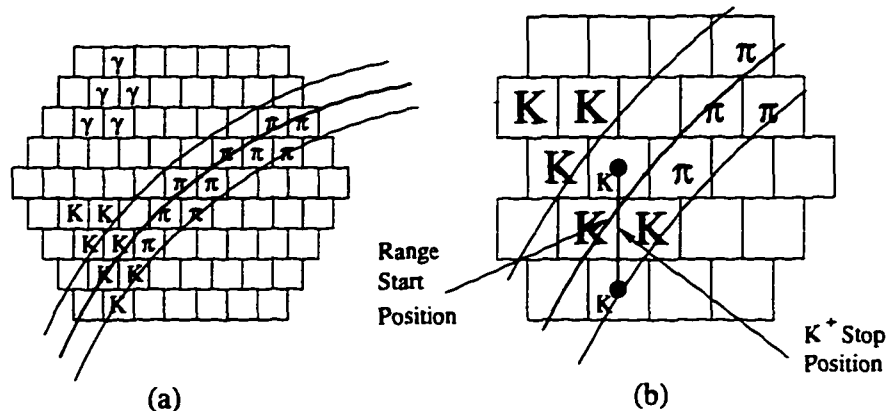


Figure 3.2: Diagrams describing SWATH Target analysis. Figure (a) shows use of the drift chamber track (shown as heavy curved line) to define a swath (shown as light curved line). Fibers identified as belonging to the K^+ are marked "K" and those belonging to the charged track are marked " π ." Figure (b) is a "blow-up" of the K^+ stopping region. The K^+ fibers at extreme clockwise and counter-clockwise positions, yet within the swath, are indicated by dots.

- Fibers in time with the Range Stack track and off the swath are identified as coming from a photon.

Fibers identified as coming from the K^+ are then used in conjunction with the DC track to determine the K^+ stopping position as shown in Figure 3.2(b). The two K^+ fibers whose centers are at extreme clockwise and counter-clockwise positions along the track, yet are inside the swath are identified. The K^+ stop position is then defined as the mid-point of the line joining the two fibers. The Target range is defined as the distance along the track from the angular position midway between the two extreme K^+ fibers to the edge of the Target. Energy in fibers identified as coming from a photon is summed and saved as ETGPHO.

Variable	Definition
TGX,TGY	x and y coordinates of K^+ stopping position
TIMEPI	The time of the charged track as determined by the Target
TIMEK	The time of the K^+ as determined by the Target
RTGT	Charged track range in the Target, corrected by DC dip-angle
ETGT	Total energy of charged track fibers in the Target
ETGPHO	Energy identified as coming from photons.
EIC	I-Counter Energy
RIC	I-Counter Range

Table 3.4: Definitions of Target variables saved in the n-tuple.

Since the Target yields only two-dimensional information, the dip-angle of the DC track is used to calculate the three-dimensional range. The drift chamber track is also used to estimate the range of the charged track in the I-counter. The variables saved in the n-tuple are listed in Table 3.4.

3.3.4 Integration of Charged Track Information

Once the charged track reconstruction has been performed on all of the charged track measuring sub-systems, the information is combined to give over-all results. The first of these results is ISKCODE which indicates whether the charged track was successfully reconstructed in all of the sub-systems.

To calculate the total momentum of the charged track, PTOT_TR, we need to correct the momentum measured in the drift chamber (PDC) for the energy that is lost in the Target and in the material that the track traverses up to the middle of

the Drift Chamber. We first convert the drift chamber momentum to an equivalent range RDC using the integrated Bethe-Block equation. We can then add in the range measured in the Target (RTGT) and I-counters and correct for various pieces of dead-material:

$$\text{RTOT_DC} = \text{RDC} + \text{RTGT} + \text{RIC} + \text{RIWALL} + 0.5 \times \text{RGAS},$$

where RIWALL and RGAS are the estimated ranges in the inner wall of the drift chamber and in the drift chamber gas, respectively. Finally we convert RTOT_DC back to momentum PTOT_TR using the inverse of the integrated Bethe-Block equation.

A similar procedure is used to calculate the total kinetic energy, ETOT_TR from the RS energy ERST. In both cases Target range is used rather than Target energy, since it was found to give somewhat better resolution.

In order to perform the momentum to range conversions, it is necessary to assume a particle mass. This will usually be taken to be the μ^+ mass, except in cases where we are explicitly analyzing π^+ events. For events where the charged track is assumed to be a pion, we also subtract an amount of energy equal to that deposited by the μ^+ in $\pi^+ \rightarrow \mu^+ \nu_\mu$, since that energy is usually within the ADC gate.

In later analysis, it will also be necessary to know the direction of the charged particle at the K^+ decay vertex. The direction of the drift chamber track at its closest approach to the K^+ stopping position is used to approximate this direction and is

Variable	Definition
ISKCODE	Return code of charged track reconstruction
PTOT_TR	Total momentum of charged track
ETOT_TR	Total energy of charged track
VM(3)	Direction cosines of charged track at K^+ decay vertex
TGZ	z coordinate of K^+ stopping position

Table 3.5: Definitions of variables saved in the n-tuple from analysis combining results from the three charged track measuring detector components.

saved in the n-tuple as an array of direction cosines, VM(3). This extrapolation is also used to find the z -position of the K^+ stopping position, TGZ.

3.4 Photon Reconstruction

The $K_{\mu\nu\gamma}$ trigger requires a single cluster of photon energy in the Barrel Veto and rejects events with energy in any of the other photon veto systems. The goal of the photon reconstruction is to use the information provided by the Barrel Veto to measure the energy, time and position of the required photon. Each counter is read out on both ends and so gives a time, measured with TDC's, and an energy, measured with ADC's, from each end. The time measurement for a counter is obtained by averaging the two end times. This takes out the effect of the finite light propagation speed. Similarly, the energy measurement is made by taking the geometric mean of the energies from the two ends, since this takes out the effect of light attenuation.

3.4.1 Barrel Veto Z Measurement

Conversely, the effects of finite light propagation speed and finite attenuation lengths can be used to measure the z position of a photon. The two measurements of z are defined:

$$z_{tdc} = \frac{c}{2}(T_1 - T_2) + d, \quad z_{adc} = \frac{\lambda}{2} \log \frac{A_2}{A_1} + f,$$

where T_1 and T_2 are the times in the two ends, A_1 and A_2 are the measured energies, c is a calibration constant which is equal to the speed of light in the counter, λ is the light attenuation length in the counter, d and f are offsets.

The primary calibration that is applied to the Barrel Veto data is aimed only at measuring the time and energy of energy depositions. It produces time offsets to align the mean time in each counter and energy scales to align the geometric mean of energy in each counter. However, it does not calculate the constants needed to convert the ADC and TDC measurements into z -positions. A three-step secondary calibration procedure was therefore performed to find these constants:

- Find the speed of light, c in the counters by selecting cosmic ray events that just clip the corner of the BV.
- Find the offset of the TDC-based z -measurement by extrapolating $K_{\mu 2}$ events into the BV. The speed of light and offset are assumed to be the same for all

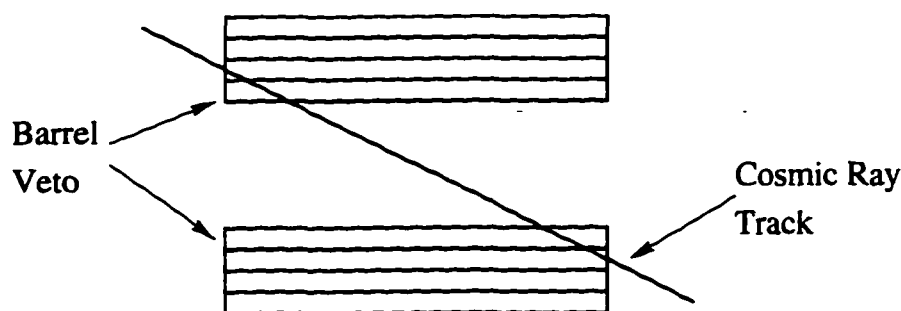


Figure 3.3: Illustration of the type of cosmic ray events used to measure the speed of light in the Barrel Veto.

counters in the system.

- Align the ADC-based z measurement to the TDC-based one in each counter using a χ^2 minimization procedure. This yields a λ and f constant for each counter.

While the second two steps are self-explanatory, the first step requires a little more description. This step employs cosmic ray events of a very particular geometry shown in Figure 3.3. These events have tracks that cross the end of the BV active region, leaving energy in one or more of the inner layers, but not in one or more of the outer layers. Events of this type are easily identified by this energy deposition pattern and are useful because they deposit energy very close to the end of the outermost counter which they crossed. Since the length of the counters is known, a measurement of the time difference (Δt) between the arrival of the light at the near and far ends of the outermost struck counter can be used to determine the speed of light in the counters.

Distributions of Δt for cosmics of this type is shown in Figure 3.4 where separate

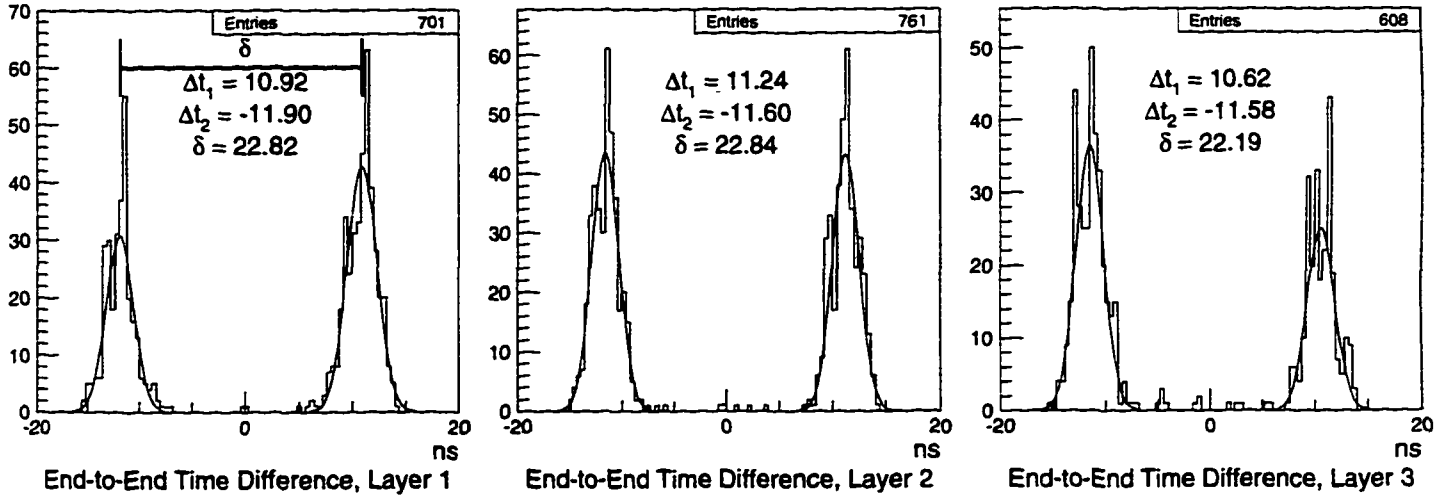


Figure 3.4: End-to-end time difference measured in the Barrel Veto for cosmics of the type shown in Figure 3.3.

plots have been made for each BV layer. Two peaks are observed in each layer, one coming from tracks crossing the upstream side of the detector and one coming from tracks crossing the downstream side. In principle, these peaks should be at symmetric positions about zero. However, a slight offset in the primary time calibration can cause these peaks to be offset. The time difference (δ) between the two peaks was therefore taken to remove this effect. The speed of light is thus calculated

$$c = \frac{2L}{\delta},$$

where c is the speed of light in the counter, L is the length of the counter and δ is the difference between the positions of the two peaks. Δt is taken as the average over all layers and is found to be 22.2 ns. This yields a c of 17.1 cm/ns which is significantly higher than the value used in previous analyses of 15.0 cm/ns [25].

The TDC-based offset found by extrapolating $K_{\mu 2}$ events into the BV is +2.91 cm.

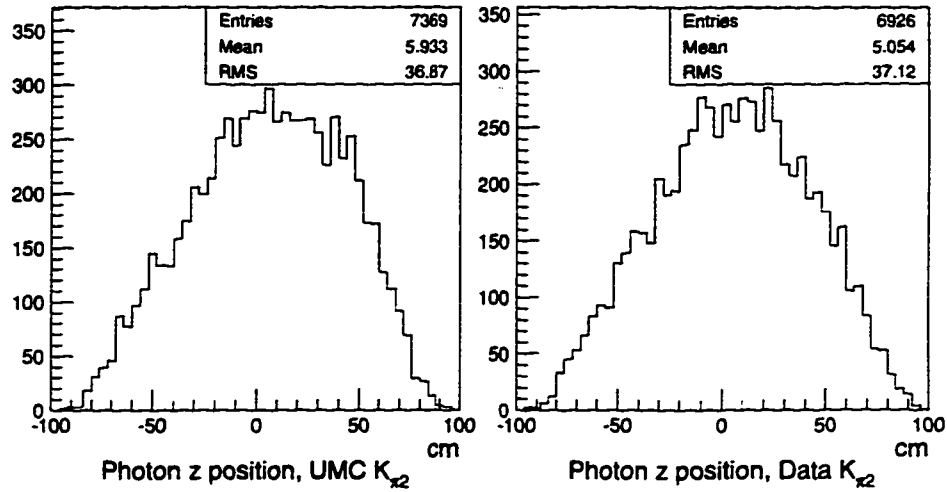


Figure 3.5: Measured z position of photons from $K_{\pi 2}$ in UMC and in data.

This is roughly consistent with the value of +4.0 cm that one obtains by centering the end-to-end time distributions in Figure 3.4. The source of the offset is that that primary BV time calibration is done assuming that the distribution of photons in the BV is centered at $z = 0$. In fact, for this data set, the mean K^+ stopping position was several centimeters downstream of $z = 0$ and this is reflected in the z -distribution of photons in the BV and thus in the calibration constants.

As a check of the entire z -calibration procedure, the measured z -position of photons from $K_{\pi 2}$ events was compared to that observed in Monte Carlo. These distributions are shown in Figure 3.5 and are found to agree quite well. When the old value for the speed of light was used the distributions did not agree well. The RMS of the distribution in data was 32.60 cm, compared to the 36.87 cm which is observed in UMC.

It has been found in previous analyses that the best single measurement of z in a counter is obtained by combining the two measurements as follows [25]:

$$z_{com} = \frac{z_{tdc} + z_{adc} \times \sqrt{E/10}}{1 + \sqrt{E/10}},$$

where E is the counter energy measured in MeV. It is this combined measurement that will be used in all further calculations.

3.4.2 Clustering

Once the time, energy and z -position of each struck counter have been determined, contiguous groups of such counters are grouped into clusters representing individual photons. This process is illustrated in Figure 3.6. For each cluster, a number of quantities are calculated. These include the total energy (EREG), the energy-weighted time (TREG), energy-weighted ϕ -position (PHIREG) and energy-weighted z -position (ZREG). The direction of the photon is determined by extrapolating from the K^+ stopping position in the Target to the measured photon position. The three direction cosines of the photon are saved in VG(3). The time and energy for each hit in the cluster are saved as TMOD and EMOD. The variables for the two highest energy clusters are saved in the n-tuple as shown in Table 3.6.

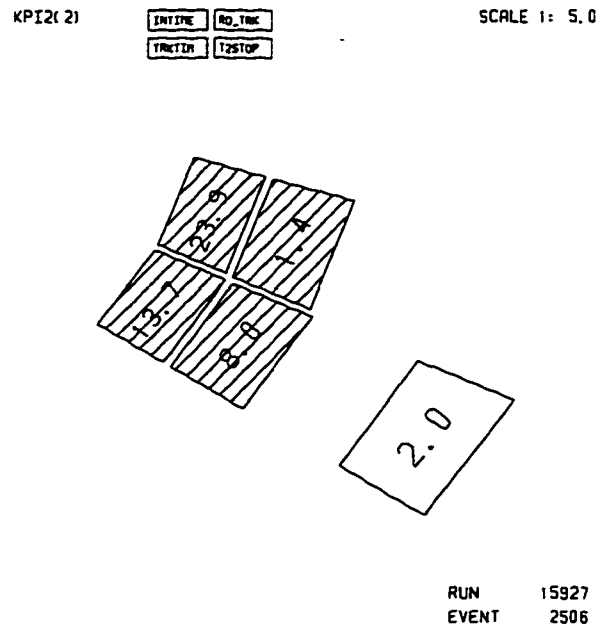


Figure 3.6: Event picture illustrating the BV cluster-finding procedure. The hatched counters have been grouped together into a cluster because they are contiguous. The unhatched counter has been left out of the cluster. The numbers indicate the visible energy in MeV in each counter.

Variable	Definition
NHIT	Number of counters in the highest energy cluster
EMOD(NHIT)	Energy of each module in the cluster
TMOD(NHIT)	Time of each module in the cluster
EREG	Total energy of the cluster
TREG	Energy weighted time of the cluster
PHIREG	Energy weighted ϕ position of the cluster
ZREG	Energy weighted z position of the cluster
VG(3)	Direction of photon
NHIT2, EREG2, ...	Variables for second highest energy cluster

Table 3.6: Definitions of variables saved for re-constructed Barrel Veto photons.

3.5 Final Kinematic Calibration

While calibrations are performed by system experts on each of the components of the detector, it is still necessary to do some fine-tuning of the kinematic variables. The $K^+ \rightarrow \mu^+ \nu_\mu$ and $K^+ \rightarrow \pi^+ \pi^0$ decays provide mono-energetic peaks in charged track energy and momentum against which the total momentum and energy measurements can be checked. Similarly, the sum of the energy of the two photons from the π^0 in $K^+ \rightarrow \pi^+ \pi^0$ decay provides a mono-energetic peak which can be used to check the energy calibration of the Barrel Veto. The measured peak positions of each kinematic variable are lined up with the known peak positions with a simple linear relationship. To line up the measured total momentum peaks with their known values the momentum measured in the drift chamber is adjusted:

$$PDC' = a \times PDC + b,$$

where a and b are calibration constants to be determined.

Likewise, the Range Stack energy ERST is adjusted to bring the measured total energy peaks into line with the known values. For the Barrel Veto photon energy measurement, the sum of the energies of the two highest energy photons found in the BV (EREG and EREG2) is simply scaled to line it up with the $K_{\pi 2}$ photon energy peak. ²

²Scaling the BV photon energy is equivalent to changing the “visible energy fraction,” f_{vis} . After calibration $f_{vis} = 0.312$.

		Data	UMC
Charged Track Momentum	a	1.031	1.015
	b	-4.928	-1.536
	c	-	0.008
Charged Track Energy	a	.9320	1.016
	b	7.973	-1.767
	c	-	0.020
Photon Energy	a	.9305	0.999
	c	-	0.000

Table 3.7: Kinematic correction factors for data and Monte Carlo. The smearing factor c is only applied to Monte Carlo data.

$$\text{EREG}' = a \times \text{EREG}$$

For Monte Carlo data, the kinematic variables are also smeared so that resolutions match those observed in data:

$$\text{PDC}' = a \times \text{PDC} \times (1 + c \times G) + b,$$

where G is a unit Gaussian random number and c is the additional calibration constant to be determined.

Table 3.7 gives the calibration constants that were used. Figure 3.7 shows the kinematic peaks after calibration. Table 3.8 gives peak positions and σ for each variable before and after calibration. The resolution for charged-track momentum is 1.5%, charged-track kinetic energy it is 2.4% and for photon energy it is 13% at the $K_{\pi 2}$ peak.

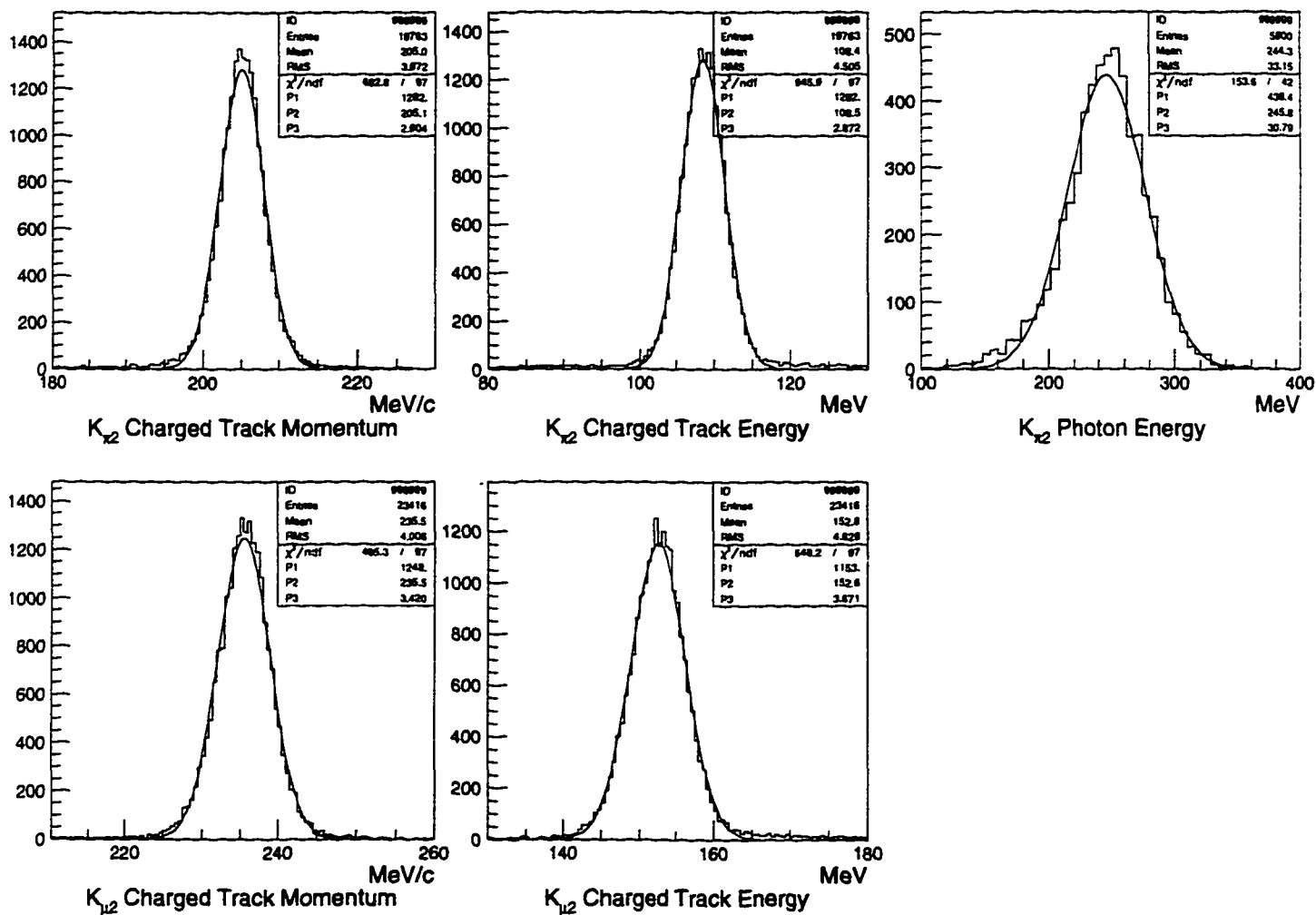


Figure 3.7: Line shapes of kinematic variables after final kinematic calibration. Note change in scale for $K_{\pi 2}$ photon energy.

		$K^+ \rightarrow \pi^+ \pi^0$		$K^+ \rightarrow \mu^+ \nu_\mu$	
		Peak	σ	Peak	σ
Charged Track Momentum - PTOT_TR (MeV/c)	Raw Data	204.3	2.76	233.8	3.29
	Corrected Data	205.1	2.90	235.5	3.42
	Raw UMC	203.9	2.50	233.9	2.88
	Corrected UMC	205.0	2.95	235.5	3.40
	True Value	205.1	-	235.5	-
Charged Track Kinetic Energy - ETOT_TR (MeV)	Raw Data	106.8	3.11	153.9	4.01
	Corrected Data	108.5	2.87	152.6	3.67
	Raw UMC	108.8	1.85	152.0	1.88
	Corrected UMC	108.5	2.80	152.4	3.49
	True Value	108.5	-	152.5	-
Photon Energy - EREG (MeV)	Raw Data	263.9	33.0	-	-
	Corrected Data	245.2	30.8	-	-
	Raw UMC	245.3	29.1	-	-
	Corrected UMC	245.8	29.0	-	-
	True Value	245.6	-	-	-

Table 3.8: Table of peak positions and resolutions for data and UMC.

3.6 Charged Track Consistency

The Drift Chamber momentum measurement and the Range Stack energy measurement are checked for consistency with a μ^+ mass hypothesis by first forming a χ^2 :

$$\chi_{fit}^2 = \left(\frac{PDC - P_{fit}}{\sigma_p} \right)^2 + \left(\frac{ERST - E_{fit}}{\sigma_E} \right)^2,$$

where E_{fit} and P_{fit} are related by

$$E_{fit} = \sqrt{P_{fit}^2 + m_\mu^2} - m_\mu$$

The errors on energy and momentum measurement are assumed to depend linearly on the measured quantities and are fixed to the values measured at the $K_{\pi 2}$ and $K_{\mu 2}$ peaks. We can substitute the above expression for E_{fit} into the the χ_{fit}^2 expression and take the derivative with respect to P_{fit} . We then minimize χ_{fit}^2 with respect to P_{fit} by numerically solving the equation:

$$\frac{d\chi_{fit}^2}{dP_{fit}} = 0$$

χ_{fit}^2 was then calculated at the minimum and converted to a confidence level called PRB_COM. Additionally, P_{fit} , which should be an improved momentum measurement was saved as PCOM. A total momentum measurement was also produced as in section 3.3.4 and saved as PCOM_TR.

Variable	Definition
COSOP	Opening angle between μ^+ and photon
EREG_CALC	Expected energy of BV photon based on COSOP

Table 3.9: Definitions of variables saved for the kinematics of the μ^+ and photon.

3.7 Muon/Photon Kinematics

Once the muon and the photon have been fully reconstructed, a number of variables describing their relation to each other can be calculated. The first is the cosine of the opening angle between them defined simply as the dot product of the muon direction vector, VM , and the photon direction vector, VG :

$$\text{COSOP} = VG(1) \cdot VM(1) + VG(2) \cdot VM(2) + VG(3) \cdot VM(3)$$

Under the assumption that a given decay was $K_{\mu\nu\gamma}$ from a K^+ at rest, the μ^+ momentum and the angle between the μ^+ and the photon are enough to completely constrain the event. We can calculate the expected energy, called EREG_CALC of the photon in terms of these variables.

$$\text{EREG_CALC} = \frac{M_K^2 + M_\mu^2 - 2M_K \sqrt{PTOT_TR^2 + M_\mu^2}}{2PTOT_TR \cdot \text{COSOP} + 2M_K - 2\sqrt{PTOT_TR^2 + M_\mu^2}}$$

Table 3.9 gives the definitions of n-tuple variables saved from this part of the analysis.

EREG_CALC could then be compared to the measured EREG to determine if the

event was a good fit to a $K_{\mu\nu\gamma}$ hypothesis. A more sophisticated method, however, which properly accounts for the measurement error of each kinematic variable is called Kinematic Fitting.³

3.8 Kinematic Fitting

In the four equations that describe conservation of 4-momentum, there are three unmeasured quantities which represent the three components of neutrino momentum. Since there is one more constraint than unknown, the problem is over-constrained (it is a “1C” problem) and one can fit for the unknown variables and determine a goodness of fit.

Ideally, we would like to solve for the unknowns and then form a χ^2 between the measured variables and a set fit variables which are consistent with conservation of 4-momentum, in analogy with section 3.6. We could then find the minimum of this χ^2 with respect to the fit variables and use this value to measure the goodness of fit of the $K_{\mu\nu\gamma}$ hypothesis.

A difficulty arises, however, in that the constraint equations are non-linear and so cannot be solved for the unknowns. Instead, a technique called “Non-Linear Least Squares Fitting with Constraints” is employed [26, 27]. This method employs Lagrange multipliers to get around the non-linearity of the constraint equations and to

³A third alternative is to calculate the “missing mass,” which should be zero since the missing particle is a neutrino. This is equivalent to the EREG_CALC comparison.

Variable	Definition	σ
P_μ	Muon momentum (PCOM_TR)	$0.0164 \times P_\mu - 0.37$
ϕ_μ	Muon azimuthal angle (derived from VM)	0.025
θ_μ	Muon polar angle (derived from VM)	0.034
P_γ	Photon Energy (EREG)	$1.676 \times \sqrt{P_\gamma}$
ϕ_γ	Photon azimuthal angle (derived from VG)	0.027
θ_γ	Photon polar angle (derived from VG)	0.030

Table 3.10: Definitions of measured variables and their errors used in kinematic fitting.

minimize the χ^2 subject to these constraints.

The χ^2 that is formed is of the following form:

$$\chi^2 = \left(\frac{P_\mu^{meas} - P_\mu^{fit}}{\sigma_{P_\mu^{meas}}} \right)^2 + \left(\frac{\phi_\mu^{meas} - \phi_\mu^{fit}}{\sigma_{\phi_\mu^{meas}}} \right)^2 + \left(\frac{\theta_\mu^{meas} - \theta_\mu^{fit}}{\sigma_{\theta_\mu^{meas}}} \right)^2 + \left(\frac{P_\gamma^{meas} - P_\gamma^{fit}}{\sigma_{P_\gamma^{meas}}} \right)^2 + \left(\frac{\phi_\gamma^{meas} - \phi_\gamma^{fit}}{\sigma_{\phi_\gamma^{meas}}} \right)^2 + \left(\frac{\theta_\gamma^{meas} - \theta_\gamma^{fit}}{\sigma_{\theta_\gamma^{meas}}} \right)^2$$

The definitions of the measured variables and the errors that were used for each are shown in Table 3.10

After the minimization is done, the minimum χ^2 is converted to a confidence level called PRB_MGN. The fit also returns fitted values of all of the kinematic variables of the fit. These values should have better resolution than the directly measured variables. This is particularly true for the photon energy, where the fitted value EREG_FIT has a σ about half as large as the directly measured value EREG. The variables that are saved in the n-tuple from the kinematic fitting are shown in Table 3.11

Variable	Definition
PRB_MGN	Confidence Level of fit to $K_{\mu\nu\gamma}$ hypothesis
EREG_FIT	Fitted photon energy

Table 3.11: Definitions of variables saved from kinematic fitting.

3.8.1 Setting the Errors

Setting the errors of the measured variables is an important part of the kinematic fitting analysis. For the μ^+ momentum, the error is assumed to scale linearly between the σ_p found at the K_{π^2} peak and that found at the K_{μ^2} peak. For the photon energy the error is assumed to scale as the square root of the energy and is pegged to the value observed at the K_{π^2} photon energy peak. The errors of the direction measurements are taken from UMC K_{π^2} data, where the measured variable is compared to its true value and the error taken from the width of the distribution.

3.8.2 Checking with K_{π^2}

For a fit with many more constraints than unknown variables, one can look at the “stretch” functions to determine whether the errors have been properly chosen. For a 1C fit, looking at the stretch functions does not give any information. To check the procedure, then, a different technique is needed. K_{π^2} events were fit with the 1C fit technique using only one of the two photons in the event and a π^+ mass rather than a μ^+ mass. The second photon then takes on the role of the neutrino in a $K_{\mu\nu\gamma}$ fit.

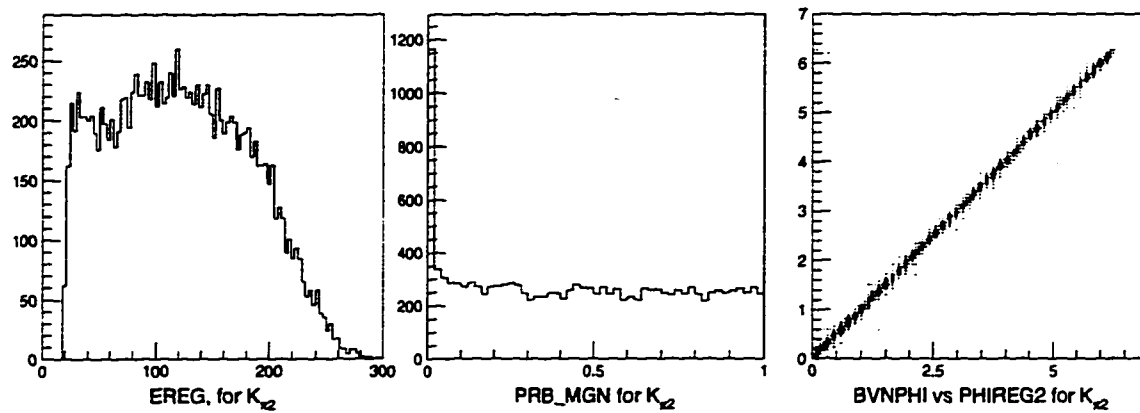


Figure 3.8: Kinematic fitting histograms for fits of $K_{\pi 2}$ events. The first histogram shows the measured photon energy spectrum of the events that were used. The middle histogram shows the confidence level of the fit. The last histogram is a scatter-plot of the expected vs. measured ϕ -position of the second photon.

Unlike the neutrino, however, we can measure the energy and direction of the photon in the BV. Therefore, we can compare the fitted values with those that are measured. Since the measured values of the second photon were not used in the fit, this gives a bias-free way of checking the kinematic fitting. To get a full range of photon energies, it is necessary to analyze both events twice - once using the lower energy photon as the “neutrino” and once using the higher energy photon.

Figure 3.8 shows the results of these checks. The confidence level of the fit is flat outside of a small region near zero, as is expected and the ϕ position of the second photon is quite well predicted.

3.9 Photon Vetoing

Once a photon in the Barrel Veto, and a charged track in the Range Stack have been reconstructed, we wish to veto on photon energy anywhere else in the detector. This will give rejection against π^0 containing events, since they will generally have two photons in the final state.

The photon veto analysis looks for photon energy in five sub-systems capable of detecting photons — the BV, the RS, the EC, the I-counters and the V-counters. The regions associated with the the charged track and the highest energy photon in the BV are excluded from the search. A prompt window around the time of the charged track (TRS) is defined for each subsystem. Energy within this time window is summed for each sub-system and saved in the n-tuple. For the RS, BV and EC, two separate prompt windows are used. This will allow the use of different energy thresholds for the different time windows.

An additional special excluded region is defined in the area of the Range Stack in front of the BV photon. This area was often found to have some photon energy that “splashed back” from the BV photon. The RS excluded area for an event is shown in Figure 3.9. Energy in that region was summed separately and called RDPE_EXCL. This will allow a higher energy threshold to be used for this special region.

Table 3.12 gives the definitions of the different regions and time windows for the energy sums. Note that the Target is also used as a photon veto system through the

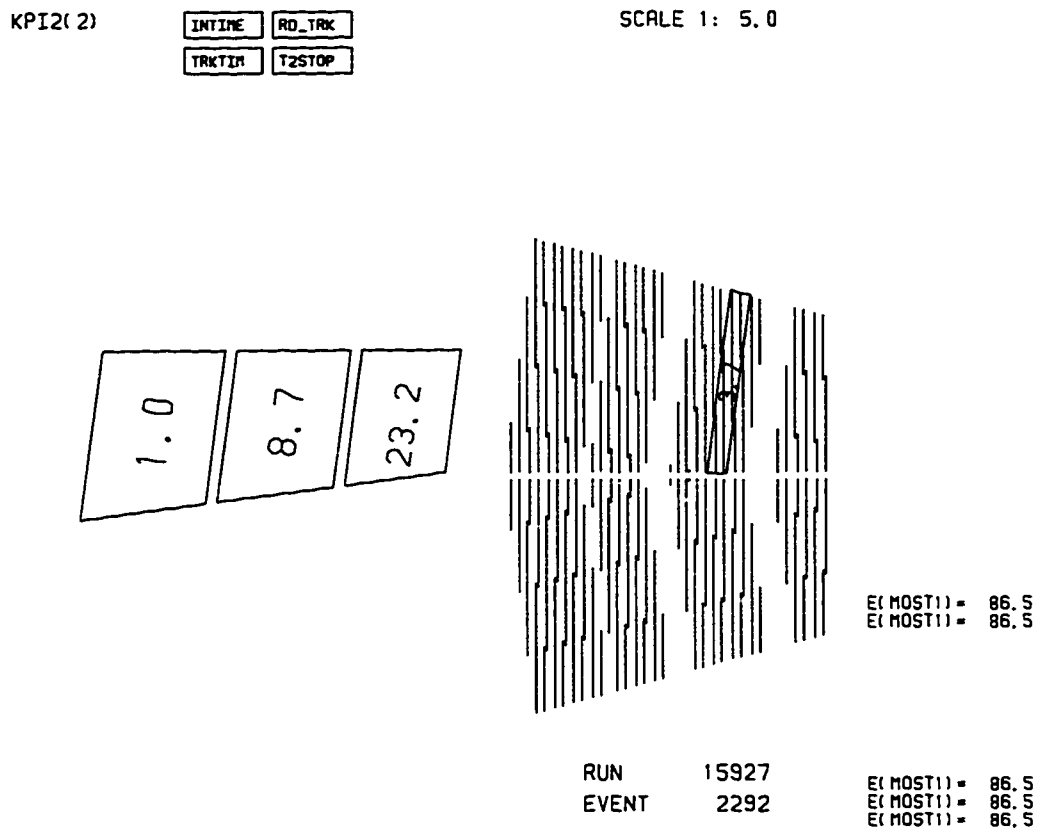


Figure 3.9: Event picture showing special excluded region in the Range Stack. Photon energy in the hatched region is added separately so that small amounts of splash back energy from the BV photon do not cause the event to be vetoed.

Subsystem	Window Half-Width	Variable Name
Barrel Veto	2.0 ns	BVPE
Barrel Veto	5.0 ns	BVPE2
Endcap	2.0 ns	E2PE
Endcap	5.0 ns	E2PE2
Range Stack	2.0 ns	RDPE
Range Stack	5.0 ns	RDPE2
RS behind photon	2.0 ns	RDPE_EXCL
I-Counters	5.0 ns	ICPE
V-Counter	5.0 ns	VCPE

Table 3.12: Definitions of second photon energy sums.

variable ETGPHO.

Background Rejection

Once the events have been reconstructed and the n-tuple formed, a series of cuts are applied to the n-tuple variables to remove background events. This produces a final sample, which will consist of $K_{\mu\nu\gamma}$ events and a small amount of background. To estimate the number of background events that will remain in this final sample, and to aid in the setting of the cuts, we perform a series of “background studies.” Each of these studies employs two separate methods of distinguishing background from signal. The two methods are applied to the data separately and the results used to estimate the number of background events that will remain when the two methods are applied together. In this way we are able to estimate the amount of background in the final sample *before* actually producing it.

In this chapter, I will first present a complete table of the cuts that were used in the analysis. I will then describe each of the individual background studies. The structure of each study will be presented and the results summarized. Detailed lists

of the precise cuts used in studies and their rejections are collected in the last section of the chapter.

4.1 Cut Definitions

For reference, I list in Table 4.1 all of the cuts that were used to cut background events. In many cases, the cut is simply a requirement that one of the n -tuple variables from the event reconstruction be within a certain range. For these cuts, the name of the cut is usually the same as the name of the variable and I will simply give the range that corresponds to the cut. Other cuts involve some further analysis that will be discussed in this chapter. For both types of cuts, I include a reference to the Section in which the variables involved in the cut are discussed.

Table 4.2 lists cuts which are used as tags of the different background sources and in other analyses.

4.2 Background Study Organization

Before going into the specific background studies of the $K_{\mu\nu\gamma}$ analysis, I will discuss the organization of background studies in general. In the simplest type of background study, one has two independent sets of cuts for rejecting a particular background source. For example, the sets of cuts for rejecting a K_{π^2} event might consist of the set

Cut Name	Definition	Description	Ref
ISKCODE	ISKCODE = 0	Charged track reconstructed OK	3.3.4
EREG	EREG > 10MeV	BV photon reconstructed OK	3.4
TRS	4 < TRS < 50	K^+ decay occurred within window	3.3.2
COS3D	COS3D < 0.5	DC dip-angle in fiducial region	3.3.1
TGZ	TGZ - 3. < 10.	K^+ stop z within fiducial region	3.3.4
ETGT	ETGT > 0	At least one CT Target fiber	3.3.3
EIC	EIC < 4	IC energy consistent with CT	3.3.3
STLAY	16 ≤ LAY ≤ 20	Stopping layer agrees with trigger	3.3.2
PROMPT	TREG - .15 < 2.	Photon in time with charged track	3.4
BW1TRS	BW1TRS + 5. > 20	No BWPC #1 hit in time with CT	3.2
BW2TRS	BW2TRS + 5. > 20	No BWPC #2 hit in time with CT	3.2
ZREG	ZREG < 70	Barrel Veto photon z -coordinate	3.4
RSIN	RDPE < 1.	Range Stack INTIME	3.9
ECIN	E2PE < 2.	Endcap INTIME	3.9
BVIN	E2PE < 2.	Barrel Veto INTIME	3.9
VCIN	VCPE < 2.	V-Counter INTIME	3.9
ICIN	ICPE < 2.	I-Counter INTIME	3.9
INTIME	RSIN · ECIN · BVIN · VCIN · ICIN	Shorthand for INTIME cuts	3.9
INTIME2	RSIN2 · ECIN2 · BVIN2	INTIME, second prompt window	3.9
RDPE_EXCL	RDPE_EXCL < 5.	INTIME in RS excluded region	3.9
ETGPHO	ETGPHO < 5.	Target photon energy	3.3.3
PRB_COM	PRB_COM > 0.01	CT Momentum/Energy Consistency	3.6
PRB_MGN	PRB_MGN > 0.05	Kinematic Fit confidence level	3.8
PHO_CHISQ	PHO_CHISQ < 2	RS energy distribution	4.7.3
FRACL	FRACL < .9	BV photon shape	4.4.2
PRB_TU5	PRB_TU5 > .05	BV photon time consistency	4.4.2
EREG_FIN	EREG > 90	Photon final spectrum cut	3.4
SPEC14	ETOT_TR > 137	Muon final spectrum cut	3.3.4

Table 4.1: List of all cuts used in background rejection. The section in which the n -tuple variables involved in each cut are discussed is listed under "Ref."

Cut Name	Definition	Description	Ref
NOTPROMPT	$ TREG - .15 > 3$	Accidental Tag	4.4.1
ECIN_REQT	$(NE2CO > 1) \cdot$ $(TE2CO < 2)$	Second photon tag in EC	4.6.2
BV_REQT	$(EREG2 > 10) \cdot$ $(PHIREG - PHIREG2 > .5) \cdot$ $(TREG2 < 3)$	Second photon tag in BV	4.6.3
CTEX_REQT	$(2 < CTEX_ENER < 10) \cdot$ $(CTEX_TIME < 4)$	Overlap photon tag	4.7.1
RSIN_CTEX	$RDPE - RDPE_CTEX < 1$	γ -veto outside of CTEX	4.7.1
EPHOLAP	$EPHOLAP > 2\text{MeV}$	Overlap tag for UMC events	4.7.1
CTEX_CUT	$RDPE_CTEX < 1$	γ -veto in CTEX region	4.7.1
PTOT_KPI2	$197 < PTOT_TR < 212$	$K_{\pi 2}$ Momentum	3.3.4
STLAY_KM2	$19 \leq STLAY \leq 20$	$K_{\mu 2}(1)$ stopping layers	3.3.2
GAM_TRIG	$\overline{EC} \cdot HX \cdot \overline{NG2}$	γ -veto trigger bits	2.7.1
BVTRIG	\overline{BV}	BV γ -veto trigger bit	2.7.1

Table 4.2: List of tags used in background studies and cuts used in other parts of the analysis. The section in which the n-tuple variables involved in each cut are discussed is listed under “Ref.”

of all kinematic cuts and the set of all photon veto cuts. The first step is to isolate the background with a series of “setup” cuts designed to remove all but the background under study. One then applies the two independent sets of cuts for rejecting the background under study, separately, to this “setup” sample. To determine the total rejection that the two sets of cuts would have if applied sequentially, one simply multiplies together the rejections that the two sets had when applied separately. The expected number of background events can then be calculated by dividing the number of setup events by this combined rejection. This is shown graphically in Figure 4.1. This type of study has the desirable feature that only cuts that will actually be used in the final analysis are needed. No new cuts need to be devised, or efficiencies

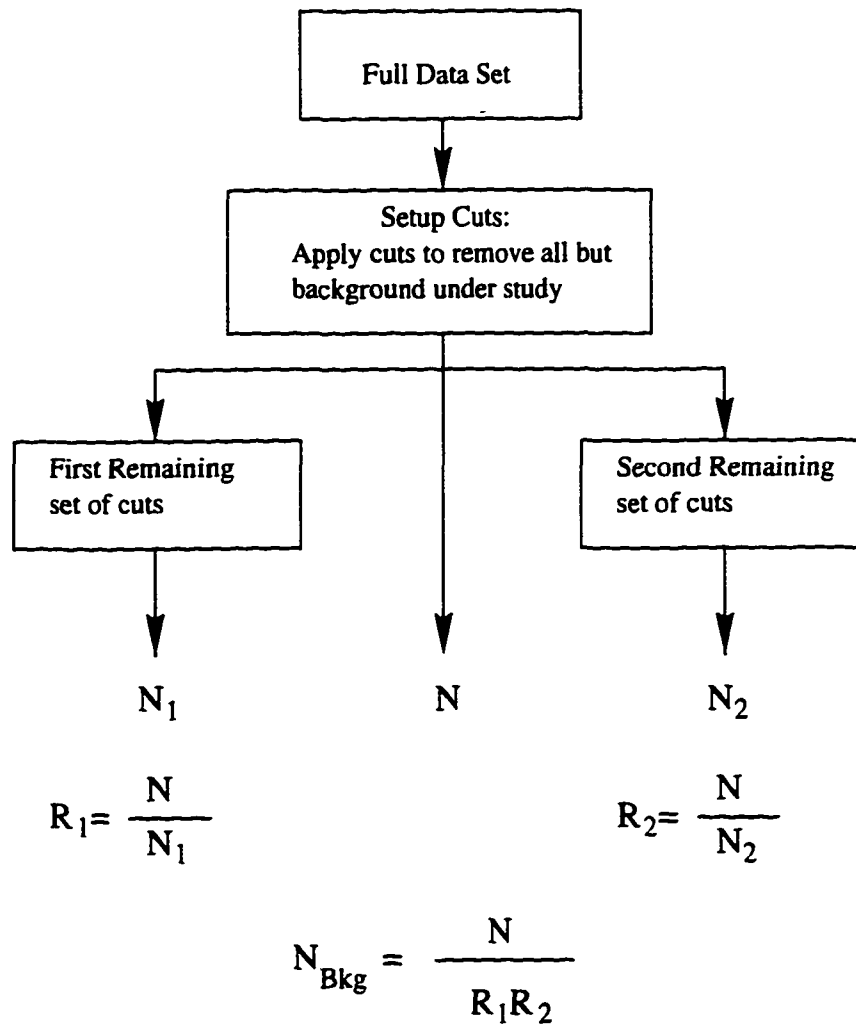


Figure 4.1: The simplest form of background study where one has two independent sets of cuts for rejecting the background.

calculated.

Despite its advantages, there are a number of ways in which this type of study can fail. If the rejections of the two sets of cuts are correlated, then the rejection of the two sets together will be mis-estimated. We study possible correlations and group the cuts to minimize such correlations. Another potential problem, which is more relevant for the $K_{\mu\nu\gamma}$ analysis, is the case where there is a large number of “signal”

events in the sample which will in principle not be rejected by either set of cuts. These signal events will then “contaminate” the background sample, thus causing an over-estimation of the background.

We can eliminate this second problem by using a second type of study as shown in Figure 4.2. Here a “tag” is used to distinguish the background from the signal. This tag will consist of cuts which will not be used in the final analysis. In fact, the tag cuts are often inverted versions of cuts that will be used in the final analysis.

In the first branch of this type background study (referred to as the “rejection” branch) the full data set is run through setup cuts to remove all other sources of background. The tag is then applied to produce a sample of N_{tag} tagged events. All remaining cuts are then applied except for those related to the tagging method. For example, if the presence of a photon in the Endcap were being used as a tag, one could not then apply the Endcap photon veto to the tagged events. This cut would therefore be removed from the set of cuts applied to the tagged events. The number of events which pass all the remaining cuts is called N_{surv} and the rejection of these cuts is calculated:

$$R_{rej} = \frac{N_{tag}}{N_{surv}}$$

In the other branch the efficiency of the tag and the rejection of the cuts related to the tag is calculated. This branch is usually run on a separate data set which

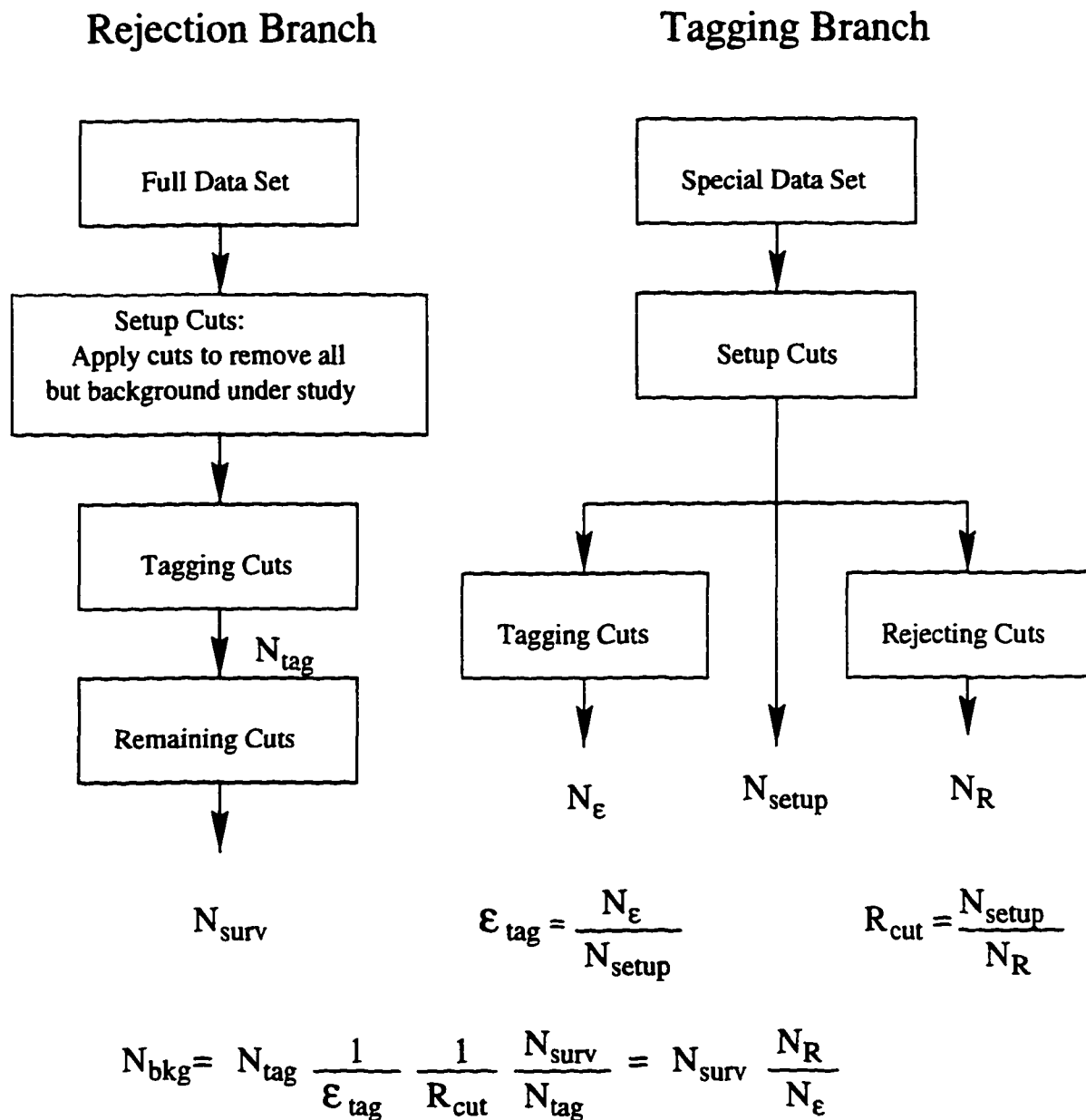


Figure 4.2: Block diagram of “tagging” type background study. Study is composed of two branches — one finds the rejection for tagged events and the other finds the efficiency and rejection associated with the tagging method.

does not have the problem of signal “contamination.” For example, to study the efficiency of an Endcap tag, we could use K_{π^2} events. A number of setup cuts are applied to produce a sample of N_{setup} events. The number of these events that pass the tagging cuts is called N_ϵ and the number that pass the rejecting cuts is called N_R . The efficiency of the tag and the rejection of these cuts are then calculated:

$$\epsilon_{tag} = \frac{N_\epsilon}{N_{setup}}; \quad R_{cut} = \frac{N_{setup}}{N_R}$$

The results of the two branches are then combined to produce an estimate of the number of background events:

$$\begin{aligned} N_{bkg} &= N_{tag} \frac{1}{\epsilon_{tag}} \frac{1}{R_{cut}} \frac{1}{R_{rej}} \\ &= N_{surv} \frac{N_R}{N_\epsilon} \end{aligned}$$

This type of study is somewhat more complicated than the first due to the need to invent new tagging cuts and the need to calculate tagging efficiencies. Nonetheless, all of the background studies which were done in the $K_{\mu\nu\gamma}$ analysis were of this second type.

Note that for the purposes of estimating the background it does not matter whether we put a particular cut into the “Setup” category or into the “Remaining cuts” for the “Rejection” branch of the study. The only number that comes out of this branch is N_{surv} — the number of tagged events that pass *all* the cuts except those

related to the tag. It is useful, however, to apply cuts not related to the background under study before the tag. That way, the tagged events will be a clean sample of the desired background and cuts can be developed to get rid of these events. In contrast, it is important that we carefully choose which setup cuts go into the tagging branch of the study since that can effect the numbers that come out of the study.

It is also not necessary to know the number of “setup” events, N_{tag} and N_{setup} , since the only numbers that appear in the expression for N_{bkg} are N_{surv} , N_R and N_c . Nonetheless, it is sometimes useful to know those numbers so that tagging efficiencies and rejections can be calculated. In cases where it is convenient to do so, I will present those numbers as well as the ones involved in the calculation of N_{bkg} .

4.3 Background Sources in the $K_{\mu\nu\gamma}$ Data Set

In identifying the sources of background for $K_{\mu\nu\gamma}$ analysis, it is useful to consider the source of the “photon” that satisfied the trigger photon requirement. There are really only three possible sources of high energy photons in the E787 detector:

- A second event, unrelated to the one that produced the charged track is responsible for the Barrel Veto energy deposition. These are called “accidentals.”
- A π^0 decay where the π^0 originated from any of several K^+ decay modes (K_{π^2} , $K_{\mu^3\dots}$) and came from the same event that produced the charged track.

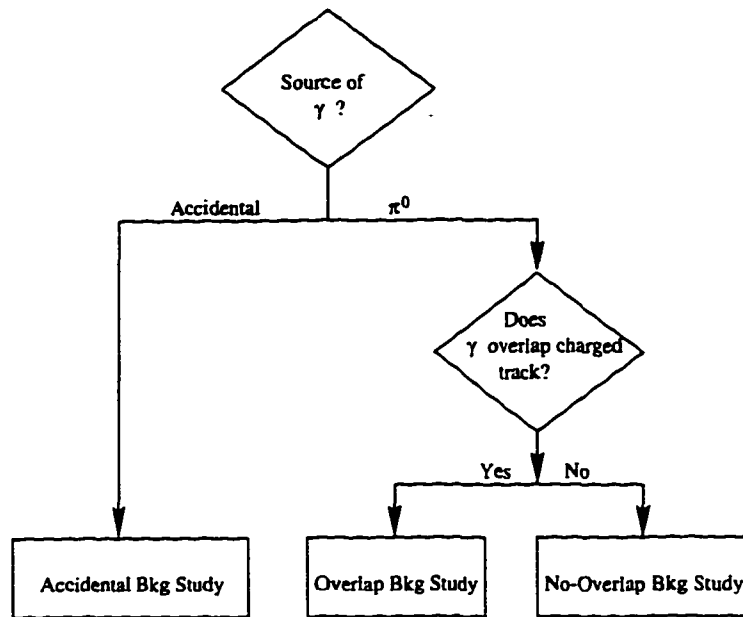


Figure 4.3: Flow chart defining background studies for $K_{\mu\nu\gamma}$ analysis.

- A “radiative” K^+ decay such as $K_{\pi 2\gamma}$, $K_{\mu 3\gamma}$ or $K_{\mu\nu\gamma}$.

For decays such as $K_{\pi 2\gamma}$ or $K_{\mu 3\gamma}$ the event will also contain a π^0 and so it can be treated together with the other types of decays with a π^0 . So, if we are able to reject events where the photon came from a π^0 and those events where the photon came from an accidental, then we really have left only one source of events — $K_{\mu\nu\gamma}$. For reasons that will be explained later, it is necessary to treat π^0 events where the photon overlapped the charged track differently from those where it did not. The overall organization of the background studies is shown in flow-chart form in Figure 4.3.

While each of the background studies produces the number of expected background events, it also produces a sample — tagged events that pass all the cuts on

Region	Definition	Source of Events
1	$ETOT_TR > 137\text{MeV}, EREG > 150\text{MeV}$	$K_{\mu\nu\gamma}(\text{SD+})$
2	$ETOT_TR < 137\text{MeV}, EREG > 150\text{MeV}$	$K_{\pi 2}, K_{\mu 3}$
3	$ETOT_TR < 137\text{MeV}, 90 < EREG < 150\text{MeV}$	$K_{\mu\nu\gamma}(\text{IB})$
4	$ETOT_TR > 137\text{MeV}, 90 < EREG < 150\text{MeV}$	$K_{\mu\nu\gamma}(\text{IB})$ and $K_{\mu\nu\gamma}(\text{SD+})$

Table 4.3: Definitions of the four spectral regions and some of the sources of events in those regions.

the “Rejection” side of the study — that can be taken as representative of the shape of the spectrum of the background under study. After applying the N_R/N_ϵ normalization, this spectrum will represent the expected background both in shape and in magnitude. As we will see in the next chapter this spectrum can be subtracted from final spectrum to account for the remaining background in a statistical way.

The sample of events which remain after all cuts, *except* the spectrum cuts will be called the the “pre-spectrum” sample. To help understand the shape of the background the phase space is split into four regions as defined in Table 4.3. The SD+ signal should be most prevalent in Region 1, so that is where we will be most concerned about the background. Region 4 will be used to help normalize the amount of $K_{\mu\nu\gamma}(\text{IB})$ in the sample and so it is also important to keep the background low there. Regions 2 and 3 are less important as they have large irreducible backgrounds from $K_{\pi 2}$ and $K_{\mu 3}$.

In the following sections I will describe the structure of each background study and the cuts that were developed in conjunction with them. I will also present the final

numerical results and spectra that each study produced. For the detailed numbers of individual cut rejection, however, I will wait until the last section of this chapter and compile them all there. This last section could be skipped or read quickly by the casual reader.

4.4 Accidental Background Study

This study is aimed at rejecting events where the “charged track” and “photon” parts of the trigger were satisfied by two separate events. The source of the charged track is usually a $K_{\mu 2}$, but there are a number of potential sources for the energy deposition in the BV:

- A π^0 decay to two photons originating from a second K^+ decay.
- A particle coming from outside the detector and depositing energy in the Barrel Veto. This includes cosmics.
- A μ^+ from a previous event which has stopped in the Barrel Veto and decayed.

This is called a “stale” muon.

There are doubtless a number of other sources of random energy deposition in the BV. Nonetheless, they all share the property that their measured time is uncorrelated with the time of the charged track.

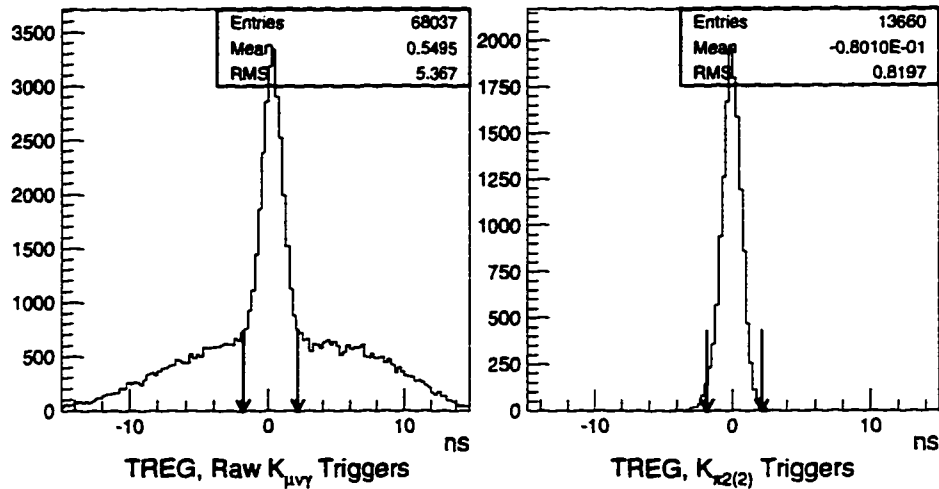


Figure 4.4: Comparison of photon time distribution measured relative to the charged track time for $K_{\mu\nu\gamma}$ triggers and for lightly selected $K_{\pi 2(2)}$. A large accidental component is visible in the $K_{\mu\nu\gamma}$ triggers. The cuts defining the prompt window are shown.

4.4.1 Accidental Tagging

For accidental events, the relative time between the muon and the photon (TREG) is random. The observed distribution of this time is determined by the trigger requirement that they come roughly within 10 ns of each other. Offline, it is possible to time much more precisely than this because of the calibrations and the correction for z -position that can be applied. Real prompt photons appear as a sharp peak in TREG whereas accidentals appear as a broad roughly flat distribution. This can be seen by comparing the TREG distribution of raw $K_{\mu\nu\gamma}$ triggers with that of $K_{\pi 2}$ events as shown in Figure 4.4. The $K_{\mu\nu\gamma}$ triggers have one component due to the broad accidental distribution and one due to the narrow prompt photon distribution. The $K_{\pi 2}$ events on the other hand have only the narrow prompt photon component.

We can therefore cleanly tag accidentals by requiring that TREG lie outside of the prompt region. This is the basis of the NOTPROMPT tag, defined as $|\text{TREG} - .15| > 3$ ns, where the .15 ns offset was necessary to line up the charged track and photon timing. NOTPROMPT will be used as the “tagging” cut in Figure 4.2. The PROMPT cut, defined as $|\text{TREG} - .15| < 2$ ns, takes on the role of the “rejecting” cuts in the Tagging branch of the study. Note that the PROMPT cut is somewhat tighter than a simple inversion of NOTPROMPT.

We now wish to calculate the efficiency of the NOTPROMPT tag and rejection of the PROMPT cut as discussed in section 4.2. To do this, we need to know the shape of the TREG distribution produced by *accidental* events. Ordinarily, this type of thing is done using other cuts to isolate a clean sample of the background under study. Accidentals, however, are difficult to isolate except with the use of the NOTPROMPT cut. So, we use the “sidebands” of the TREG distribution of distribution of raw $K_{\mu\nu\gamma}$ triggers, which we know are composed solely of accidentals, to estimate the number of accidentals in the prompt region. We assume a flat interpolation of the sidebands into the prompt region as shown in Figure 4.5 (b). We can then calculate the number of accidentals that would pass the PROMPT cut, $N_{R,acc}$, and the number of accidentals that are tagged by the NOTPROMPT tag, $N_{\epsilon,acc}$. Table 4.4 shows the numerical values of these parameters.

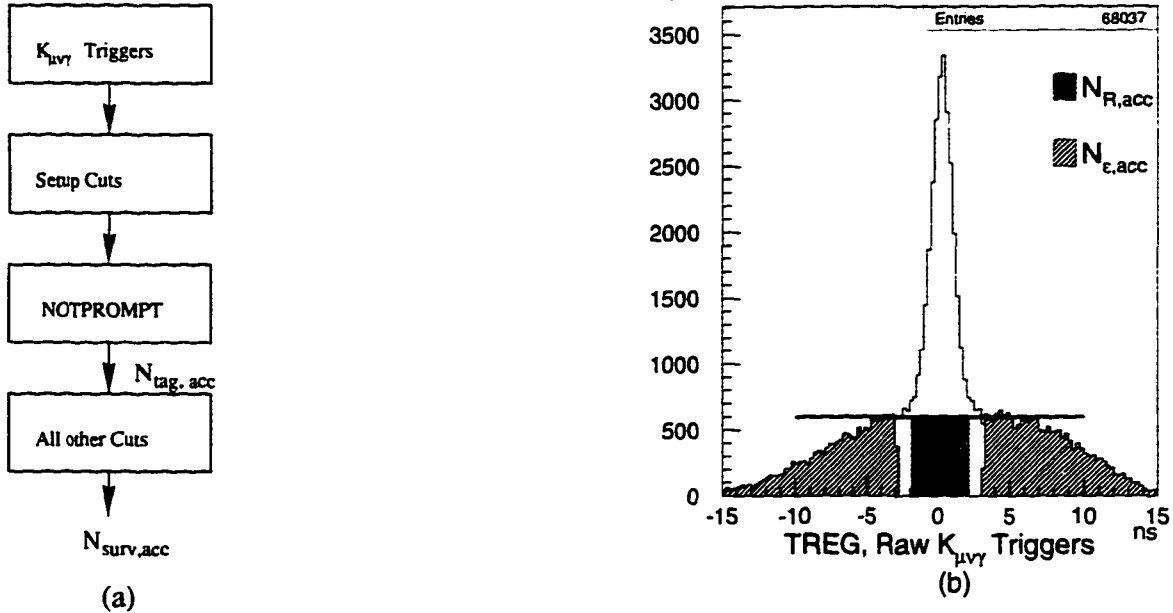


Figure 4.5: The structure of the Accidental Background Study. Plot (a) shows the “rejection” branch of the study in which events tagged by NOTPROMPT are used to measure the rejection of the rest of the cuts. Plot (b) shows the calculation of the efficiency of NOTPROMPT and the rejection of PROMPT. Single-hatched region indicates events that would be tagged by NOTPROMPT, and double-hatched indicates those that would not be cut by the PROMPT cut.

Parameter	Value
$N_{R,acc}$	9600
$N_{\epsilon,acc}$	33243
$N_{R,acc}/N_{\epsilon,acc}$	0.2888

Table 4.4: Numbers inferred from Figure 4.5

4.4.2 Accidental Rejection

The cleanness of the NOTPROMPT tag allows us to use very simple setup cuts on the rejection side of the study. These consist only of the fiducial-type cuts shown in Table 4.13. We then apply the NOTPROMPT tag and calculate the rejection of the other cuts for these tagged accidental events. The other cuts will take advantage of differences between accidental and signal events, other than the time distribution. In this section, I will describe the development of these cuts and calculate their rejection.

Beam System Cuts

One clear source of accidentals can be found by looking in the beam system. Events where a second K^+ entered the beam system can be identified by looking at the Beam Wire Chambers. Figure 4.6 shows the time of a second particle in the Beam Wire Chambers relative to the time of the charged track. The prompt peak shows that many tagged accidental events have second beam particles. The narrowing of the time distribution when the time is taken relative to the photon time shows that the photon came from this second beam particle. Events with a hit between the two cut positions are removed. Cuts are made both on the first Beam Wire Chamber (BW1TRS) and on the second (BW2TRS).

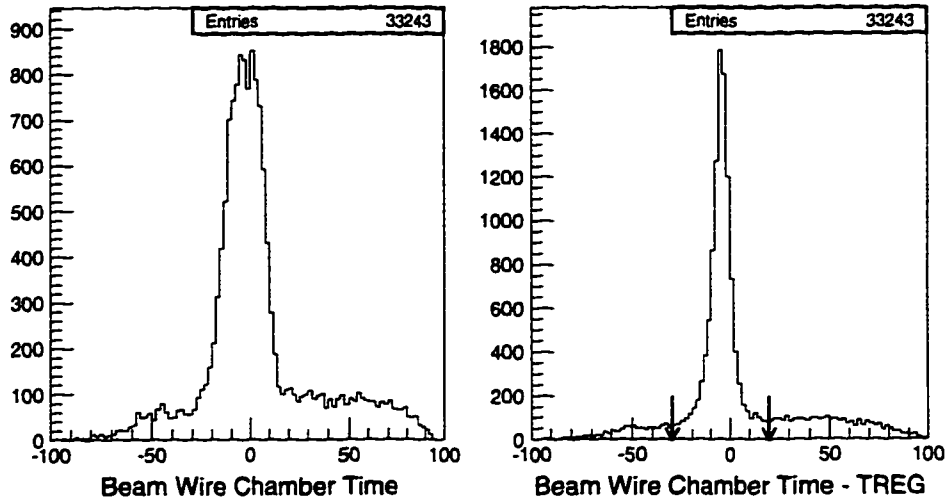


Figure 4.6: The time of a second beam particle measured in the Beam Wire Chamber shown relative to the charged track time and relative to the photon time. Cut positions are shown on the second plot.

Photon Shape Cuts

Once two beam particle events have been removed, a second source of accidentals becomes apparent in Figure 4.7. The band of events at negative z and reaching to high energy are evidently muons coming from the outside of the detector, travelling along the z direction and ranging out in the Barrel Veto. The approximately linear relationship between their energy and measured z -position is what one would expect for such muons.

The arch shaped band at lower energy is most likely due to “stale” muons or other delayed energy release processes. The arch is due to the fact that the online trigger was based on an analog *linear* sum of energy whereas the offline energy measurement is based on a geometric mean. Therefore, photons which are located at high $|z|$ require

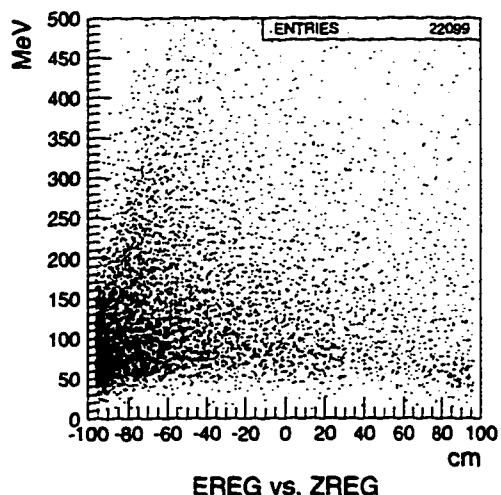


Figure 4.7: Scatter plot of photon energy vs. photon z-position for events tagged as accidentals and passing Beam Wire Chamber cuts.

less real (offline) energy to cause a trigger. Most of these are at low photon energies and so do not present a serious background problem.

Knowing that the photon part of the $K_{\mu\nu\gamma}$ trigger is often caused by particles other than photons traveling from the inside of the detector makes it possible to design cuts based solely on photon variables. A particle traveling along the z-direction will tend to deposit most of its energy in one BV layer, whereas a photon traveling essentially in the radial direction will tend to shower outward into several layers. This is the basis of the FRACL variable which is defined as follows:

$$\text{FRACL} = \frac{\text{MAX}(E_{\text{lay}})}{\text{EREG}},$$

where E_{lay} is the photon energy summed by layer. Figure 4.8 shows a histogram of this variable for tagged accidentals. For comparison, a plot of the same variable for

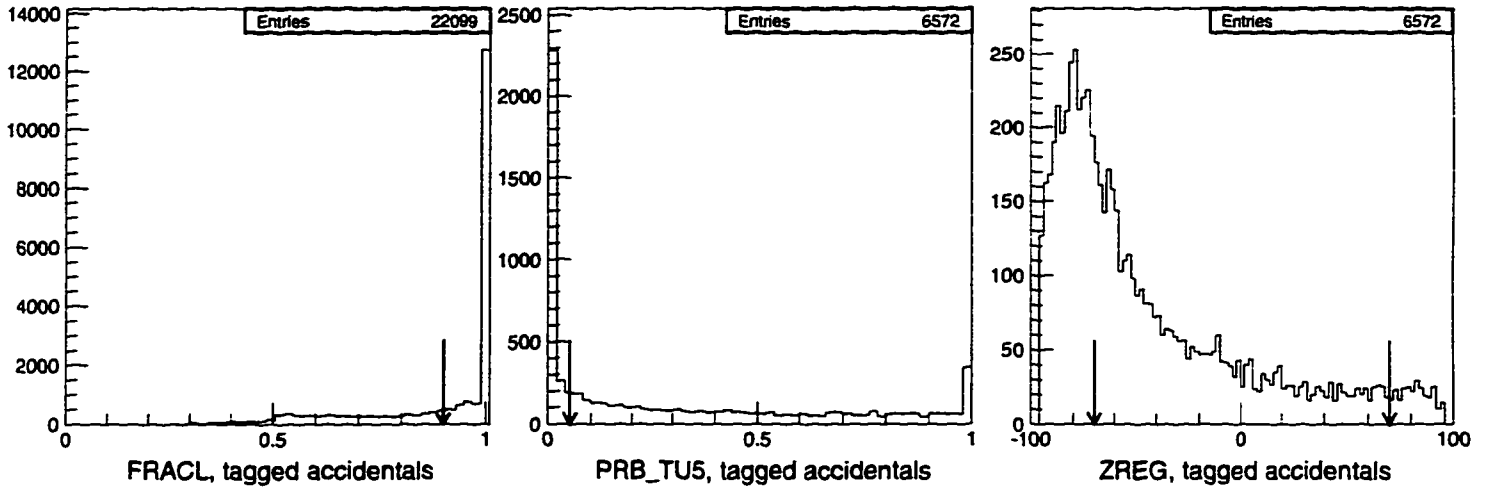


Figure 4.8: Histograms of photon shape variables used to distinguish accidentals from real photons. To be compared to Figure 4.9. The arrows show the cut positions.

$K_{\pi^2}(2)$ is shown in Figure 4.9.

Another way in which a particle traveling in the z -direction will look different from a photon traveling in the radial direction is in the relative timing of the different BV modules that make up the BV cluster. For a photon showering in the radial direction, the times in the different counters should agree. For a minimum-ionizing particle traveling along the counters, the measured times will be different as the particle passes from counter to counter.

A χ^2 variable which compares the times of counters with more than 2.5 MeV energy deposited (EMOD) is defined as:

$$\chi^2_{TU5} = \frac{1}{\sigma^2} \sum_{i=1}^N \left[\text{TMOD}(i) - \frac{1}{N} \sum_{j=1}^N \text{TMOD}(j) \right]^2,$$

where the TMOD array contains the times of individual counters making up the BV

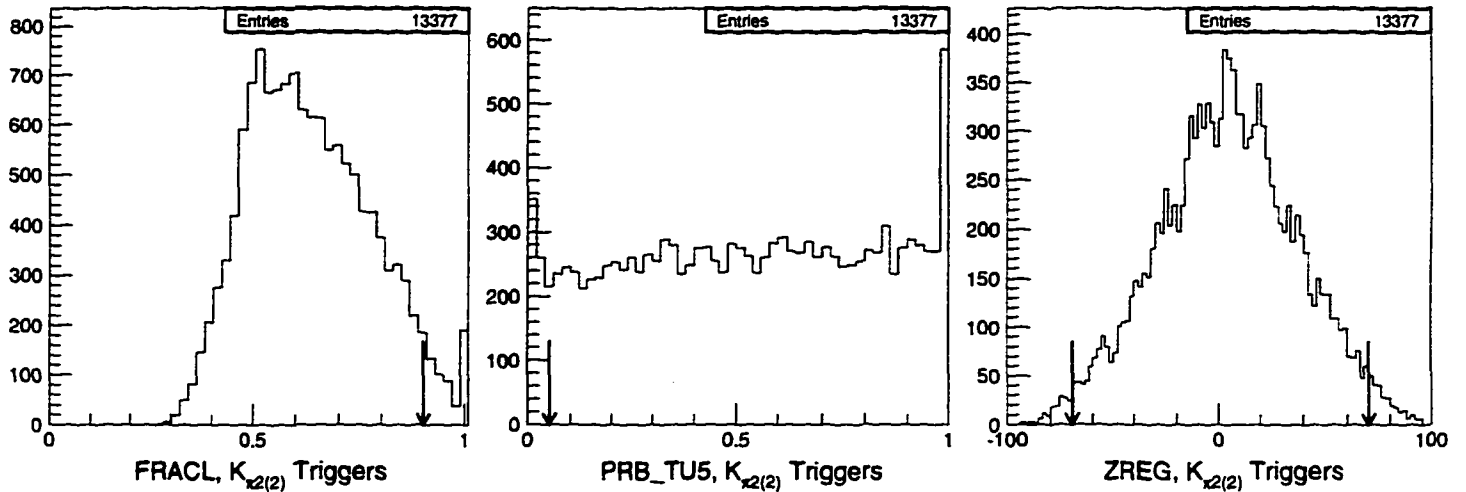


Figure 4.9: Histograms of photon shape variables for real photons from $K_{\pi 2}(2)$ triggers. The arrows show the cut positions. While we do not know that the ZREG distribution will be the same for $K_{\mu\nu\gamma}$ as for $K_{\pi 2}$, we can at least see that there is a difference between real photons and the fake ones in Figure 4.8

cluster, and N is the number of counters with $\text{EMOD}(i) > 2.5$ MeV.

The CERNLIB routine PROB is used to convert this χ^2 with $N - 1$ degrees of freedom into a confidence level — PRB_TU5, which can be cut on. Figure 4.8 shows a histogram of this variable for non-beam accidentals— i.e. tagged accidentals after the BW1TRS and BW2TRS cuts have been applied.

A third way to distinguish non-beam accidentals from photons is by their measured z -position. A histogram of this variable is shown in Figure 4.8.

Kinematic Fitting

A generic property of all accidentals that can be used to reject them is that the angle between the muon and photon is random. Thus, they will not fit to a $K_{\mu\nu\gamma}$

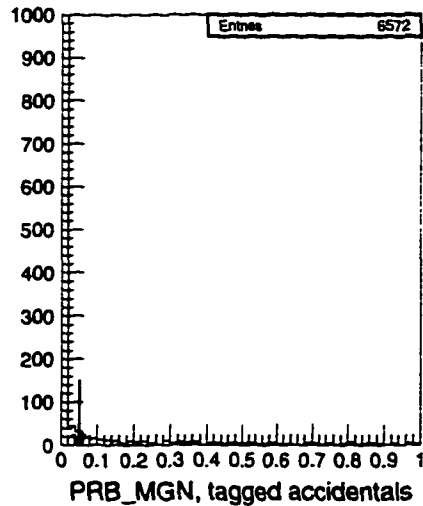


Figure 4.10: Histogram of kinematic fit probability for tagged accidentals. Zero bin has been reduced to show other bins. Actual zero bin content is much higher.

hypothesis very well. As was described in Section 3.8, the kinematic fitting produces a fit probability (PRB_MGN) that can be cut on. Figure 4.10 shows the distribution of this variable for tagged accidentals.

4.4.3 Accidental Spectrum

In this study, as in the others, it will be useful to apply all the cuts except for the final “spectrum” cuts on total muon energy and photon energy and then examine this final spectrum. The spectrum produced by applying all cuts except for the PROMPT cut is shown in Figure 4.11. The spectrum shows that the muon energy for the accidental background is peaked at the $K_{\mu 2}$ energy as expected.

The normalization calculated in the tagging branch of the study ($N_{R,acc}/N_{\epsilon,acc}$) can now be applied to the spectrum and the expected number of events in each of

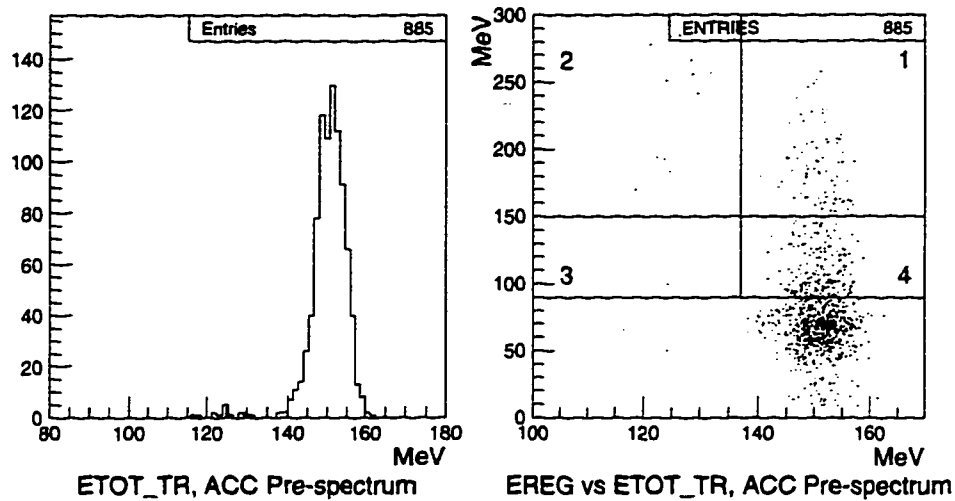


Figure 4.11: Final spectra of surviving tagged events in the accidental background study. The first plot shows the charged-track kinetic energy and the second plot shows the photon energy versus the charged-track kinetic energy.

the spectral regions calculated. The result of this is presented in Table 4.5.

4.5 π^0 Background Studies

To study the rejection of events where the BV photon came from a prompt π^0 , we again need a tag to distinguish them from signal events. Since π^0 's decay to two photons 98.8% of the time, and the trigger only requires one photon, there will usually be a second photon available to tag. The $K_{\mu\nu\gamma}$ trigger was designed to veto on this second photon, but many still pass and are visible in the various photon detectors.

Ideally, we would like to make a bifurcated background study where one branch is based on photon vetoing and the other on kinematic-type cuts. A problem arises in this proposed bifurcation, however, due to the possibility that the second photon

NOTPROMPT Tagging			Reference
N_{tag}	518431		4.14
$N_{R,acc}/N_{\epsilon,acc}$	0.2888		4.4
Events	Raw (N_{surv})	Expected (N_{bkg})	
Pre-spectrum	885	255.6 ± 8.6	4.15
Region 1	79	22.8 ± 2.6	-
Region 2	12	3.5 ± 1.0	-
Region 3	1	0.3 ± 0.3	-
Region 4	196	56.6 ± 4.0	-
Region 1 + 4	275	79.4 ± 4.8	-

Table 4.5: Results from rejection branch of accidental background study. The number of events measured in each spectral region is shown. The expected number in each region after all cuts have been applied is obtained by multiplying by the N_R/N_ϵ normalization. Regions do not sum to “Pre-spectrum” total, because events with $ERE\bar{G} < 90\text{MeV}$ are not included in any of the regions. The “Reference” gives the table number in which the number was calculated.

overlaps the charged track. Energy from the photon can then contribute to the measured charged track energy, thereby producing a large correlation between photon vetoing and kinematic rejection.

We therefore need two separate π^0 background studies. The first, called the “No-Overlap” study, is based on the bifurcation between photon vetoing and kinematics. It tags events by seeing the second photon in either the Endcaps or in the Barrel Veto. Such a tag establishes not only that the event had a π^0 , but also that the second photon did not overlap the charged track. We can therefore apply the kinematic cuts to the tagged events without fear that photon energy is contributing to the measured charged track energy. The second study is called the “Overlap” study and is aimed at

events where the photon *did* overlap the charged track. It requires a separate tagging method and is described in Section 4.7.

4.6 No-Overlap Background Study

In the No-Overlap study we tag events with a π^0 by identifying the second photon in one of the photon veto subsystems. The rejection of the kinematic cuts for tagged events is then measured. $K_{\pi^2}(2)$ monitor events are used as a source of π^0 's to measure the efficiency of the tag and the rejection of the photon veto cuts. While we have removed the possibility of a correlation between the two branches due to photon energy overlapping the charged track, it is still possible that correlations due to other sources exist. To check for this possibility, two separate subsystems are used to tag the second photon: the BV and the EC. These two subsystems tag photons in quite different areas of the available phase space. A comparison of the results from the two subsystems will therefore be sensitive to any possible correlation. Figure 4.12 describes the structure of the two studies.

4.6.1 Photon Vetoing

In the $K^+ \rightarrow \pi^+ \nu \bar{\nu}$ analysis, we are used to getting π^0 rejections of order 10^6 from photon vetoing. The rejection in this analysis, however, will be much more modest. Whereas the $K^+ \rightarrow \pi^+ \nu \bar{\nu}$ analysis can veto on *any* photon energy, in the $K_{\mu\nu\gamma}$ analysis

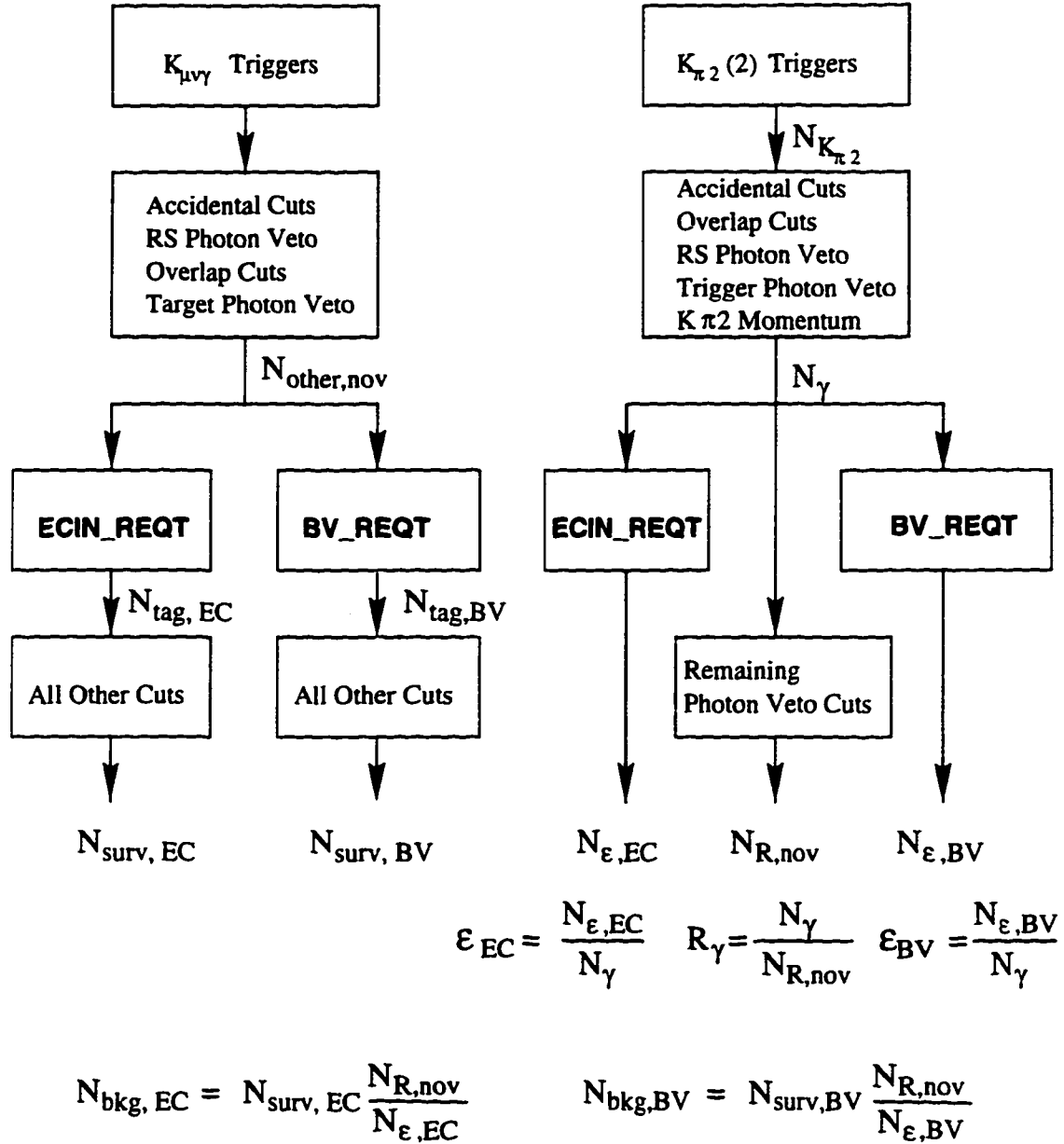


Figure 4.12: Chart describing No-Overlap background study. There are actually two independent studies being performed simultaneously — one employing an Endcap tag and the other a Barrel Veto tag.

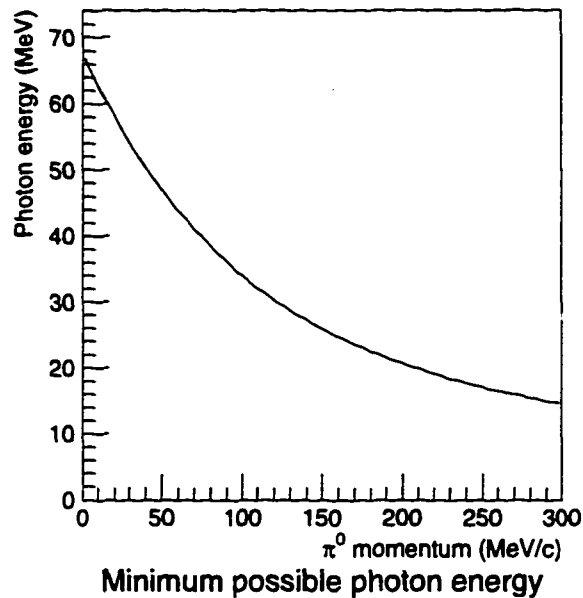


Figure 4.13: Minimum possible photon energy is plotted as a function of momentum of the π^0 that produced the photon.

we can only veto on a *second* photon. Indeed, this photon will tend to be quite low in energy since the photon in the barrel is often nearly back-to-back with the charged track and so has quite a high energy. Nonetheless, we are aided in photon vetoing by the fact that a π^0 in the momentum range of interest cannot produce photons of arbitrarily low energy. The minimum photon energy for a π^0 of given momentum is shown in Figure 4.13. The maximum π^0 momentum from $K_{\mu 3}$ is 215 MeV/c, so the minimum possible photon energy is approximately 20 MeV.

Photon vetoing is done by placing cuts on the energy sums defined in Section 3.9. Figure 4.14 shows the distribution of energy vs. time of photon energy in each of the subsystems for raw $K_{\mu\nu\gamma}$ triggers. Superimposed on the plots are the time windows and energy thresholds that were used.

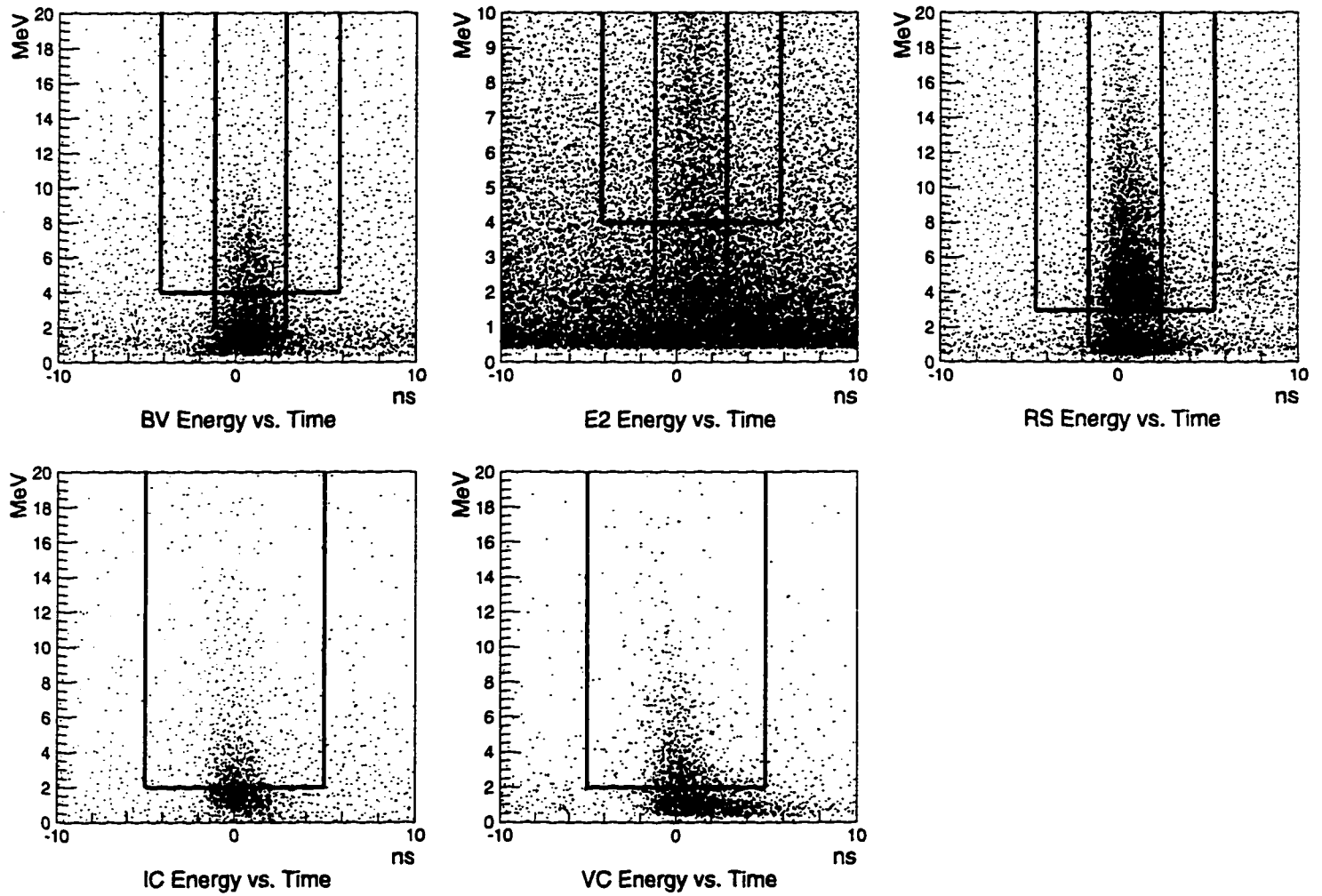


Figure 4.14: Energy and time of hits recorded in photon veto sub-systems for raw $K_{\mu\nu\gamma}$ triggers. Positions of time and energy windows are indicated.

To calculate the post-trigger rejection of the photon veto we use a sample of $K_{\pi 2}(2)$ events as a source of π^0 's. To ensure that the events used are really $K_{\pi 2}$, a number of setup cuts are applied including a momentum cut bracketing the $K_{\pi 2}$ momentum peak. We then exclude the highest energy photon found in the BV from the energy sums, just as is done $K_{\mu\nu\gamma}$ triggers. The trigger photon vetoes are then applied to produce a sample of N_γ events, all of which should have a second photon in them. The cuts that produced this sample are shown in Table 4.16. The number of these events that pass all the remaining photon vetoes is called $N_{R, \pi 0}$. The numerical values of these parameters are given in Table 4.6.

4.6.2 Endcap Tagging — ECIN_REQT

To tag photons in the EC, one could, in principle, just invert the EC INTIME cut. However, due to a large accidental rate in the Endcaps, there would be a large number “fake” tags, which would allow $K_{\mu\nu\gamma}$ events into the background study, thereby polluting it. What is done instead is to form “clusters” of crystals with more than 2 MeV measured in each and with times within 2 ns of each other. The number of crystals in the largest cluster is called NE2CO and the the energy weighted time of the cluster is called TE2CO. The tag ECIN_REQT is then defined as:

$$(NE2CO > 1) \cdot (|TE2CO| < 2)$$

The tag therefore requires a coincidence between two or more crystals, which greatly reduces the fake tags due to accidentals.

To measure the efficiency of ECIN_REQT, we use the same sample of N_γ events as was used for the photon veto rejection. The number of these events that are tagged by ECIN_REQT is called $N_{\epsilon,EC}$. The numerical values of these parameters are shown in Table 4.6.

4.6.3 Barrel Veto Tagging — BV_REQT

Compared to the EC, the BV has the advantage that its accidental rates are lower. It also has the disadvantage that the trigger has already required one photon in the BV, thus complicating the detection of a second. Nonetheless, clean second photons are detectable and can be used in a tag called BV_REQT.

BV_REQT uses the photon cluster variables of the second highest found in the BV as described in section 3.4. In terms of those variables, the BV_REQT tag is defined as:

$$(|\text{PHIREG2} - \text{PHIREG}| > .5) \cdot (\text{EREG2} > 10 \text{ MeV}) \cdot (|\text{TREG2}| < 3 \text{ ns}).$$

The second photon is required to be separated from the first in ϕ to avoid a potential source of mis-tagging due to fragmentation of the shower of the first photon into two separate geometrical regions. While this is potentially dangerous because

Parameter	Value		Reference
$N_{K_{\pi 2}(2)}$	32948		-
N_{γ}	1677		4.16
N_R	319		4.17
$R_{\gamma} \equiv N_{\gamma}/N_R$	5.2571		-
	EC Tagging	BV Tagging	
N_{ϵ}	295	545	-
$\epsilon \equiv N_{\epsilon}/N_{\gamma}$	0.1759	0.3250	-
N_R/N_{ϵ}	1.0814	0.5853	-

Table 4.6: Results from tagging branch of No-Overlap background study.

it rules out events where the second photon was close the first, the results from the Barrel Veto tag can be compared with those of the Endcap tag, so any significant bias should be apparent.

The sample of N_{γ} events is again used to measure the efficiency of the tag in the identical way as ECIN_REQT. The numbers extracted from this branch are shown in Table 4.6.

4.6.4 Mis-Tagging

Before going on to the “Kinematic” branch of the study, it is useful to estimate the probability that an event will cause a second photon tag, when in fact none exists. A mis-tag of $K_{\mu\nu\gamma}$ events can lead to an over-estimation of background. This mis-tag probability is calculated by kinematically selecting clean $K_{\mu 2}$ events, then applying the trigger photon vetoes and then separately applying the the BV_REQT

and ECIN_REQT tags. Since $K_{\mu 2}$ events should not have any photons associated with them, this will give an estimate of the mis-tagging probability. There is a complication in finding the Barrel Veto mis-tagging probability because that tag normally looks at the *second* photon measured in the BV, whereas $K_{\mu 2}$ events will not normally have any. To measure the mis-tagging, the tagging requirements are applied to the first photon instead.

For a given mis-tagging rate, one can make an estimate of the number of events in regions 1 and 4 of the final background spectrum that are really mis-tagged $K_{\mu\nu\gamma}$ events. This is done by skipping ahead in the analysis and taking the number of events in regions 1 and 4 in the final spectrum, i.e. after *all* cuts have been applied. Since the final sample is essentially all $K_{\mu\nu\gamma}$, this represents the number of $K_{\mu\nu\gamma}$ events that pass all the cuts. We then multiply this number by the measured mis-tagging rate to estimate the number of “background” events that are really mis-tagged $K_{\mu\nu\gamma}$ events. We can then compare this number of events in the regions 1 and 4 of the background spectrum, which will be found in the following sections.

The results of the mis-tagging check are given in Table 4.7.

4.6.5 No-Overlap Rejection

Kinematic rejection of $K_{\mu 3}$ events comes largely from requiring that the charged track kinetic energy lie above the $K_{\mu 3}$ endpoint of 134.0 MeV. This endpoint is also the

Parameter	Value		Reference
$N_{K_{\mu 2}, setup}$	16287		4.18
	EC Tagging	BV Tagging	
N_{tag}	91	29	-
$\epsilon_{mis} \equiv N_{tag}/N_{K_{\mu 2}}$	0.559×10^{-2}	0.178×10^{-2}	-
Mis-tagged $K_{\mu\nu\gamma}$	15.0	4.8	-

Table 4.7: Results from mis-tagging study performed with $K_{\mu 2}(1)$ events including an estimate of the number of $K_{\mu\nu\gamma}$ events that will be mis-tagged and will end up in the regions 1 and 4.

highest possible energy of a μ^+ coming from a $K_{\pi 2}$ where the π^+ decayed in flight, and so is very effective against $K_{\pi 2}$ events as well. Other kinematic-type cuts consist mostly of clean-up of various reconstruction problems to try to make the kinetic energy cutoff as clean as possible.

Momentum/Energy Consistency Cut —PRB.COM

Under the assumption that the charged particle was a μ^+ , the Range Stack energy measurement and the Drift Chamber momentum measurement are redundant, and so can be checked for consistency with a μ^+ mass hypothesis. While $K_{\mu 3}$ events will mostly be consistent with this hypothesis, $K_{\pi 2}$ events will usually not be. In UMC studies, it was found that most $K_{\pi 2}$ events that passed the trigger did not come to a stop in the Range Stack normally. Either the π^+ decayed in flight, or it had a nuclear interaction, or another non-standard process occurred. The decays-in-flight quite often happen in the Drift Chamber volume thereby compromising the

momentum measurement, due to the “kink” that the in-flight decay causes. However, the kinetic energy measurement is still quite reliable. On the other hand, there are a number of background sources, such as π^+ nuclear interactions in the Range Stack, which cause an increase in the kinetic energy measurement, yet do not affect the momentum measurement.

The effect of the decays in flight can be seen in Figure 4.15 where the spectra of total momentum and total kinetic energy are plotted. The tails of the momentum distribution are much more pronounced and go far beyond kinematic limit of 235.5 MeV/c due to π^+ decay in flight disturbing the circle fit. For this reason, the muon total energy ETOT_TR is used for all spectrum cuts. As described in section 3.6, the variable PRB_COM can be used as a check of consistency between the momentum measured in the DC and the energy measured in the RS. A histogram of this variable for EC-tagged events is shown in Figure 4.16.

Kinematic Fitting — PRB_MGN

The PRB_MGN cut removes some π^0 events, although it is not nearly as effective against them as it is against accidentals. The angle between the muon and photon for $K_{\mu 3}$ events is almost what it would be for a $K_{\mu\nu\gamma}$ event. The only kinematic difference between these types of event is the extra low energy photon coming from the π^0 . In a $K_{\mu 3}$, the amount of energy this represents can be quite small compared

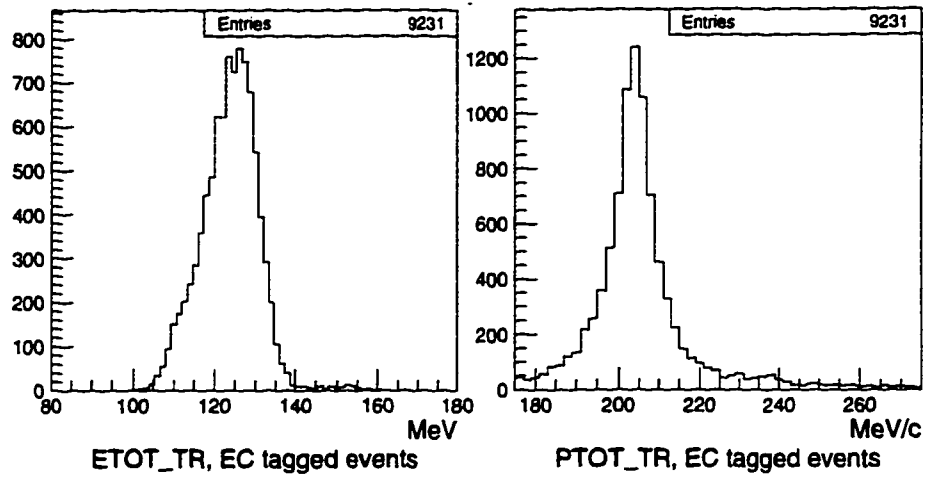


Figure 4.15: Histograms of kinetic energy and momentum for EC tagged events. Note the cutoff at $ETOT_TR=134$ MeV and large momentum tails.

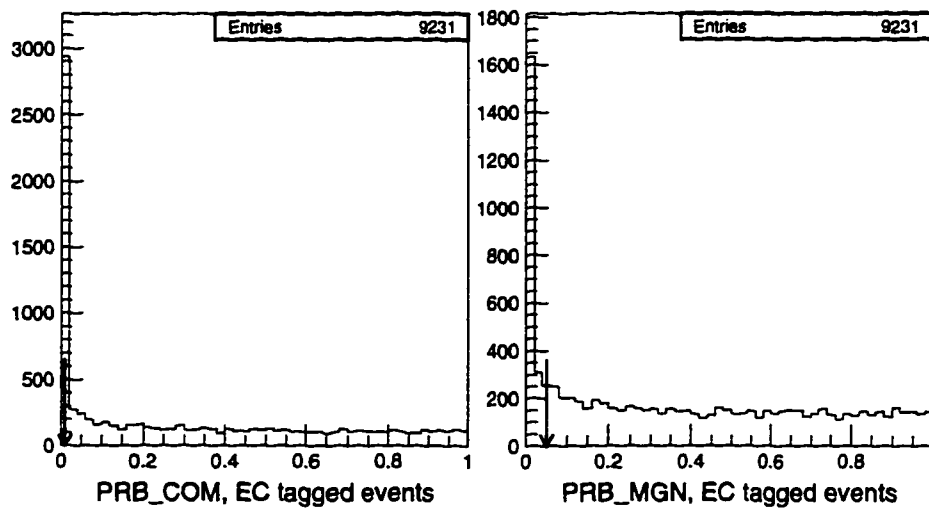


Figure 4.16: Histograms of confidence level for momentum energy comparison and for kinematic fitting for EC tagged events.

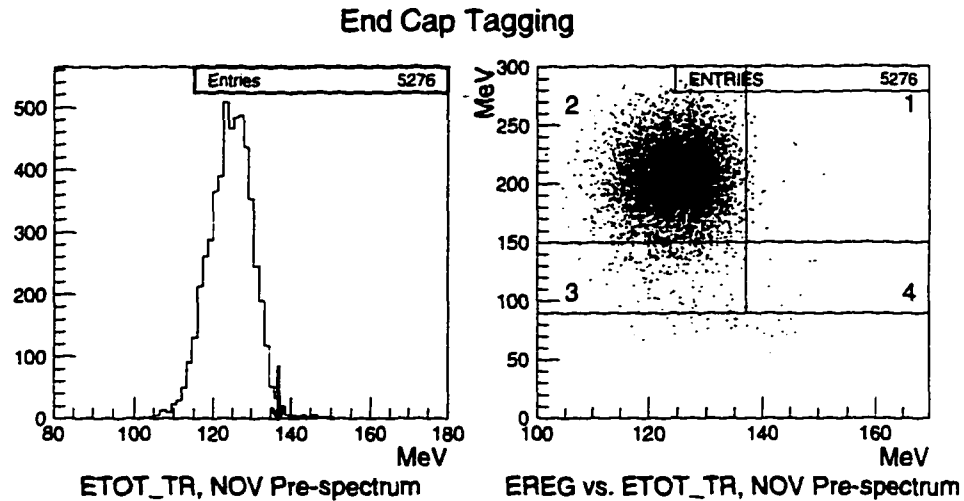


Figure 4.17: Final Spectra of surviving tagged events for the No-Overlap background using Endcap tagging.

to the energy resolution of the Barrel Veto, which explains the rather low rejection of this cut for this type of event. Figure 4.16 shows a histogram of PRB_MGN for EC tagged events.

4.6.6 No-Overlap Spectrum

The final spectrum for No-Overlap background for Endcap tagging is shown in Figure 4.17 and for Barrel Veto tagging in Figure 4.18. The number of events observed in each spectral region for each type of tagging is shown in Table 4.8. The expected number of events in each spectral region is obtained by multiplying the number of survivors of the Kinematic branch by the N_R/N_ϵ normalization obtained in the Photon Veto branch.

In the EC-tagging study the number of background events observed in regions 1

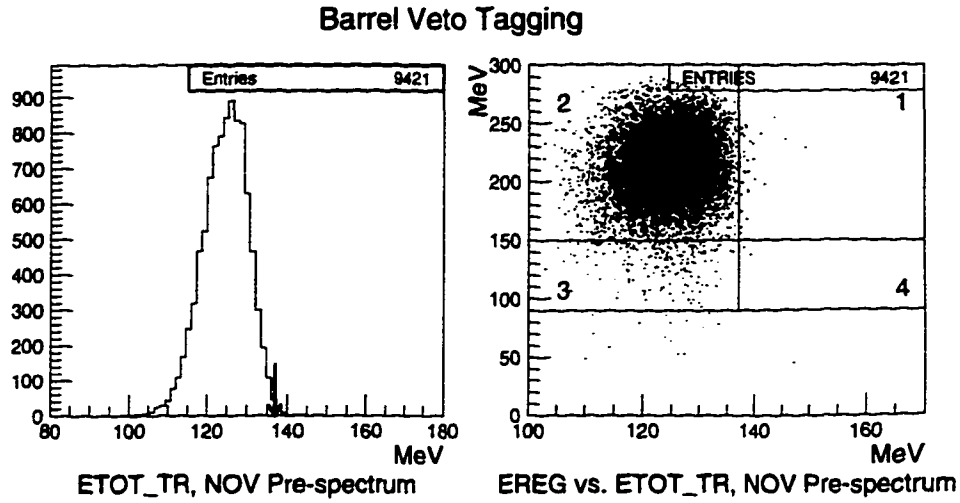


Figure 4.18: Final Spectra of surviving tagged events for the No-Overlap background using Barrel Veto tagging.

	EC Tagging		BV Tagging		Reference
$N_{other,nov}$	74373				4.20
N_{tag}	9289		16577		-
N_R/N_ϵ	1.0814		0.5853		4.6
Events	Raw (N_{surv})	Expected (N_{bkg})	Raw	Expected	
Pre-spectrum	5225	5650.3 ± 78.2	9326	5458.5 ± 56.5	4.22
Region 1	30	32.4 ± 5.9	40	23.4 ± 3.7	-
Region 2	4946	5348.6 ± 76.1	9052	5298.1 ± 55.7	-
Region 3	209	226.0 ± 15.6	213	124.7 ± 8.5	-
Region 4	6	6.5 ± 2.6	3	1.8 ± 1.0	-
Region 1 + 4	36	38.9 ± 6.5	43	25.2 ± 3.8	-

Table 4.8: Results from kinematic branch of No-Overlap background study. For each type of tagging the number of tagged events in each spectral region is shown. The expected number in each region after all cuts have been applied is obtained by multiplying by the N_R/N_ϵ normalization.

and 4 is 36 . In Table 4.7 we saw that the expected number of mis-tagged $K_{\mu\nu\gamma}$ events in regions 1 and 4 was 15.0 . Apparently, mis-tagging is causing a non-negligible fraction of the background events and so we are somewhat overestimating the background.

As can be seen in the “Expected” columns of the table, the results for the two tagging methods are quite consistent in the critical region 1. The results in regions 3 and 4 are somewhat less consistent. This is due to a combination of different mis-tagging rates for the different methods and somewhat different photon energy distributions for the different tagging methods.

4.7 Overlap Background Study

As mentioned in the Section 4.5, π^0 -containing events where one of the photons from the π^0 overlaps the charged track will not be properly tagged in previous background study. They therefore require an entire background study of their own. Some of these events can be tagged as an overlap by noting extra energy next to the track in the Range Stack. Such an event is shown in Figure 4.19. There may also be some energy *on* the track which will be included in the measured energy and can therefore push the event above the kinematic limit for π^0 containing events and into the signal region. While the event shown in Figure 4.19 could be rejected by the presence of the extra energy, there are presumably many other events with an overlapping photon where all the extra energy is confined to the track counters and so cannot be rejected by

this method. We will therefore have to develop other cuts to get rid of these events. We will use the extra energy next to the charged track to tag overlap events and make the assumption that these events are representative of all overlap events. We will then use Monte Carlo data to estimate the efficiency of this tag and the rejection that is obtained by vetoing events with extra energy RS energy. The structure of this study is shown in Figure 4.20.

4.7.1 **Overlap Tagging**

The pattern of struck counters of charged tracks in the Range Stack is usually very simple, consisting of a “straight line” of counters. The RD_TRK algorithm, described in Section 3.3.2, usually includes all counters due to a single charged track. To tag photon energy near the charged track, we can define a region surrounding the RD_TRK charged track, comprising counters directly adjacent to those used by RD_TRK. This is called the “CTEX” region and is shown in Figure 4.19 for a typical overlap event. For the purposes of the Overlap background study, this region is excluded from the RS photon veto. The total energy in the region within wide time window of ± 50 ns is then summed (CTEX_ENER) and an energy weighted average time for this energy is calculated (CTEX_TIME). The CTEX_REQT cut, which will be used to tag overlap events is then defined as follows:

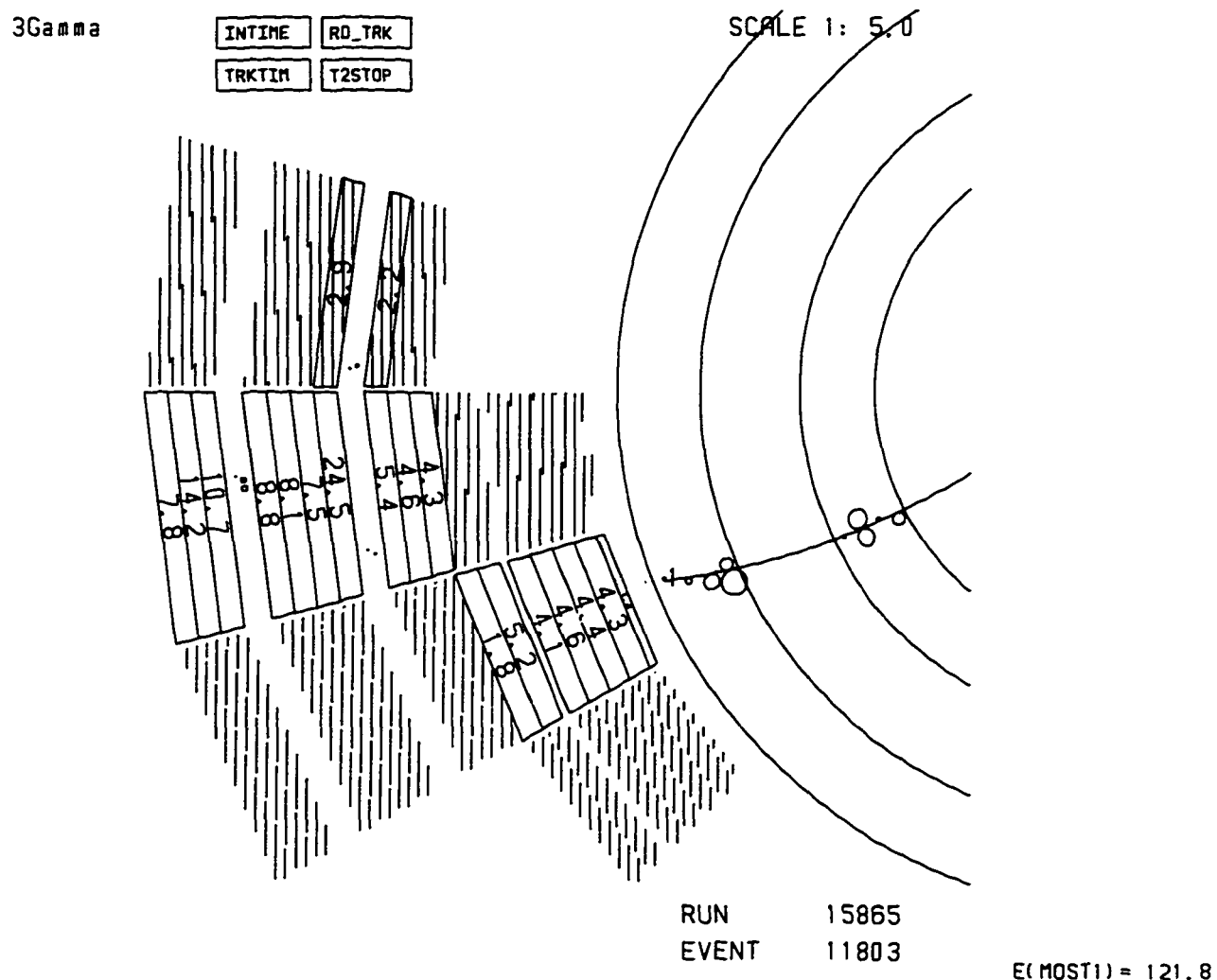


Figure 4.19: Event picture showing charged track excluded (CTEX) region. The unhatched counters show the charged track region, as determined by the RD_TRK algorithm and the hatched region indicates the CTEX region associated with it. In this event there was some energy in the CTEX region and so the event would be tagged by the CTEX_REQT cut.

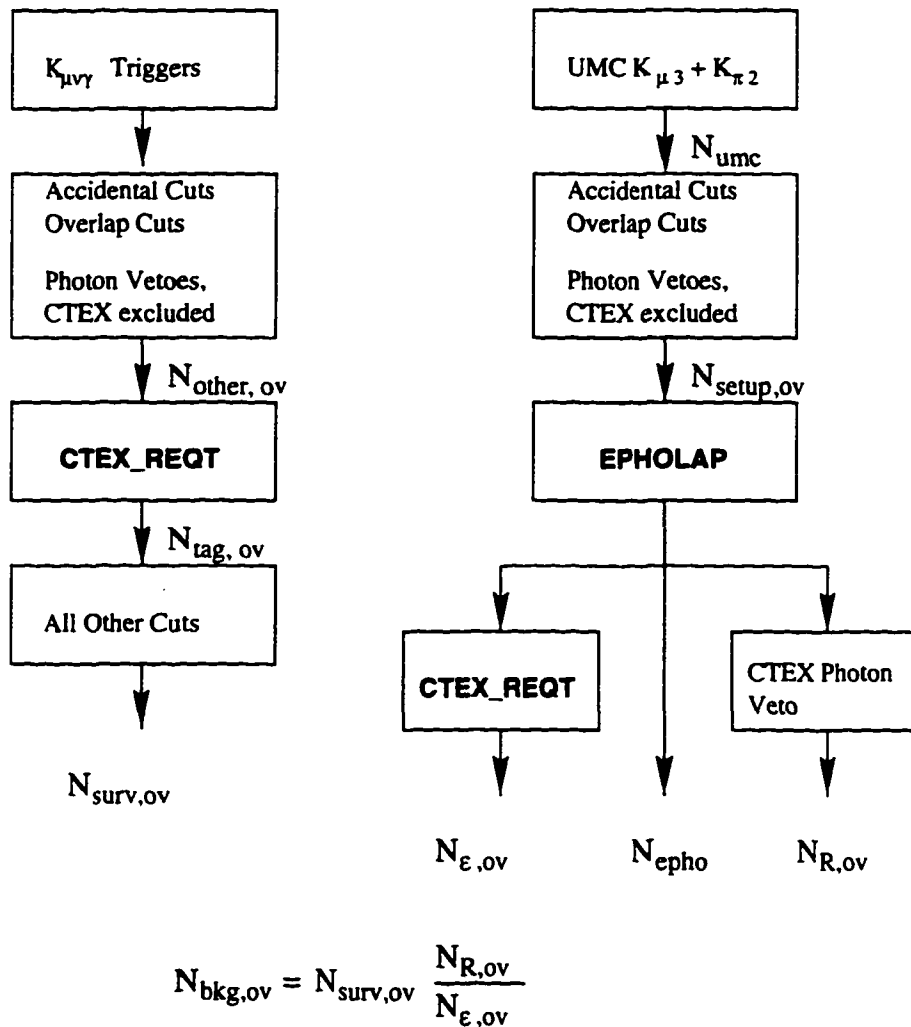


Figure 4.20: Chart describing Overlap background study. Overlap events are tagged by requiring energy in the CTEX region. The efficiency of this tag and the rejection obtained by vetoing on energy in the CTEX region is measured with Monte Carlo.

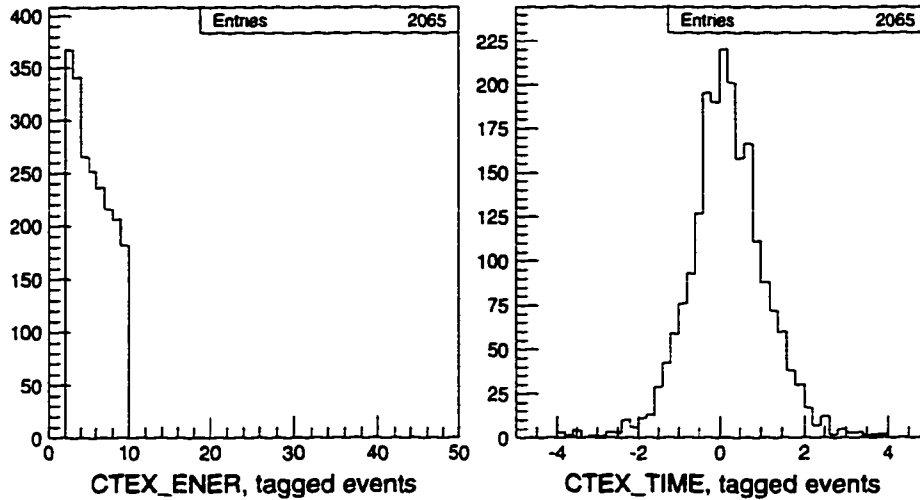


Figure 4.21: Histograms of the two variables used in overlap tagging. CTEX_ENER is the energy in the CTEX region and CTEX_TIME is the average time of this energy.

$$(2 \text{ MeV} < \text{CTEX_ENER} < 10 \text{ MeV}) \cdot (|\text{CTEX_TIME}| < 4 \text{ ns})$$

Histograms for these two variables for tagged events are shown in Figure 4.21. The potentially serious nature of this background can be seen in spectrum of the tagged events shown Figure 4.22. There are a large number of events in the signal region.

There is no easily identifiable data set that can be used to calculate the efficiency of this tag, so we are forced to use Monte Carlo. In Monte Carlo, we can definitely establish whether energy deposited on the track found by RD_TRK was due to a photon or to a charged track since we know the source of all energy deposition. We define the amount of photon energy on the charged track as EPHOLAP. We then apply the $K_{\mu\nu\gamma}$ trigger and a number of setup cuts to a Monte Carlo sample of $K_{\pi 2}$ and $K_{\mu 3}$ events, both generated in amounts equivalent to 2.16×10^8 stopped K^+ . Instead of

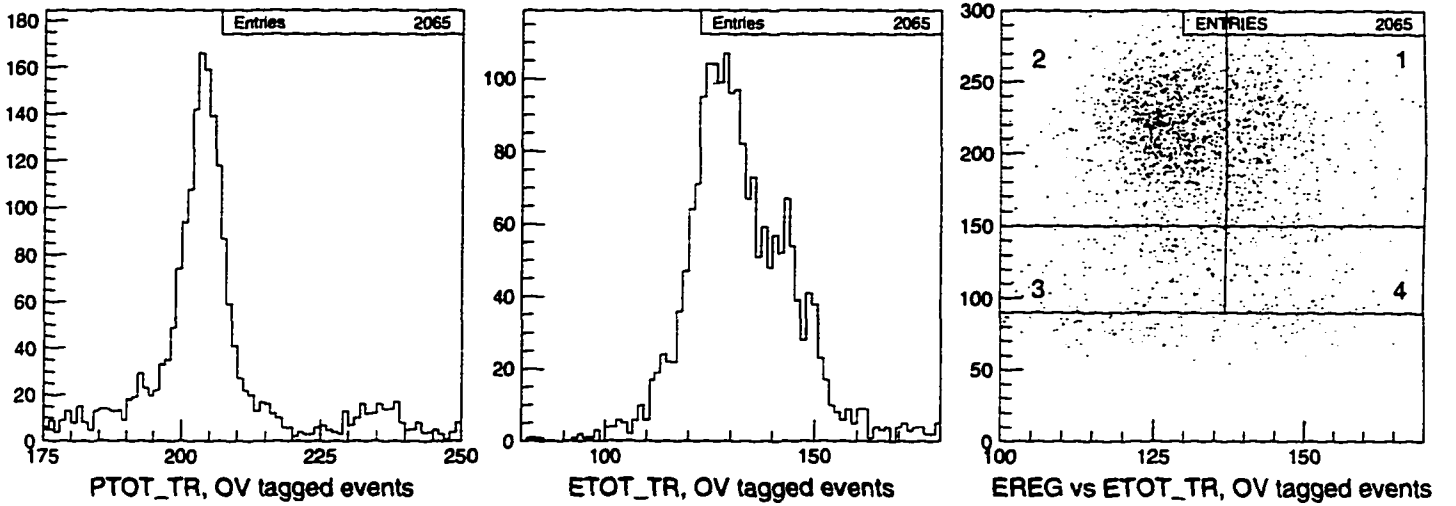


Figure 4.22: Spectra of tagged events in overlap background study.

the normal photon veto in the RS (RSIN), a special version which excludes the CTEX region is applied (RSIN_CTEX). RSIN_CTEX is defined as follows

$$RDPE - RDPE_CTEX < 1 \text{ MeV},$$

where RDPE is the total RS INTIME energy and RDPE_CTEX is INTIME energy in the CTEX region. We then select events that definitely have overlap energy with the following cut called EPHOLAP:

$$EPHOLAP > 2 \text{ MeV}.$$

This gives the number N_{epho} .

We can then check the efficiency of the CTEX_REQT on these selected events, which yields $N_{\epsilon,OV}$. We also measure the rejection of the photon veto in the CTEX region (CTEX_CUT, defined as $RDPE_CTEX < 1 \text{ MeV}$) for these events, yielding $N_{R,OV}$. The results are shown in Table 4.9

Parameter	Value	Reference
N_{UMC}	5711	-
$N_{\text{setup,ov}}$	974	4.23
N_{epho}	600	-
$N_{\epsilon,\text{ov}}$	124	-
$\epsilon_{\text{ov}} \equiv N_{\epsilon}/N_{\text{epho}}$	0.2067	-
$N_{R,\text{ov}}$	382	-
$R_{\text{ov}} \equiv N_{\text{epho}}/N_{R,\text{ov}}$	1.5707	-
$N_{R,\text{ov}}/N_{\epsilon,\text{ov}}$	3.0806	-

Table 4.9: Results of CTEX tagging efficiency study

Note that the role of the Monte Carlo here is quite limited. We are not trying to calculate the absolute rate at which overlaps occur, or the rejection of any complicated cuts. Rather, we are simply trying to measure the efficiency of the tagging method and the rejection of the photon veto for events that *do* have overlaps.

4.7.2 Mis-tagging

To check the mis-tagging probability we again use $K_{\mu 2}(1)$ triggers as in the the No-Overlap study. $K_{\mu 2}$ events are selected with a momentum cut and photon vetoing. The CTEX tag is then applied. Since $K_{\mu 2}$ events have no photons accompanying them, this gives a measure of the frequency with which events will be mis-tagged as having overlap energy when in fact none exists. The results of this study are shown in Table 4.10.

Parameter	Value	Reference
$N_{K_{\mu 2}}$	13949	4.24
$N_{tag,ov}$	59	-
ϵ_{mis}	0.423×10^{-2}	-
Mis-tagged $K_{\mu\nu\gamma}$	11.4	-

Table 4.10: Results from mis-tagging study performed with $K_{\mu 2}(1)$ events including an estimate of the number of $K_{\mu\nu\gamma}$ events that will be mis-tagged.

4.7.3 Overlap Rejection

The main new weapon against overlap events is the PHO_CHISQ cut described in section 3.3.2. A histogram of PHO_CHISQ for CTEX tagged events is shown in Figure 4.23 and for $K_{\mu 2}(1)$ events in Figure 4.24.

The cuts PRB_COM and PRB_MGN are also effective against overlap events as shown in Figures 4.23 and 4.24.

4.7.4 Overlap Spectrum

The final spectrum obtained from the Overlap background study is shown in Figure 4.25, and in Table 4.11. Here, we see that the number of events observed in Regions 1 and 4 (13) is similar to the number expected from mis-tagged $K_{\mu\nu\gamma}$ (11.4). This indicates that many of the events which are being counted as background may actually be $K_{\mu\nu\gamma}$ events that were mis-tagged. We are therefore somewhat overestimating the background due to this source. We will see in the next chapter that this is quite

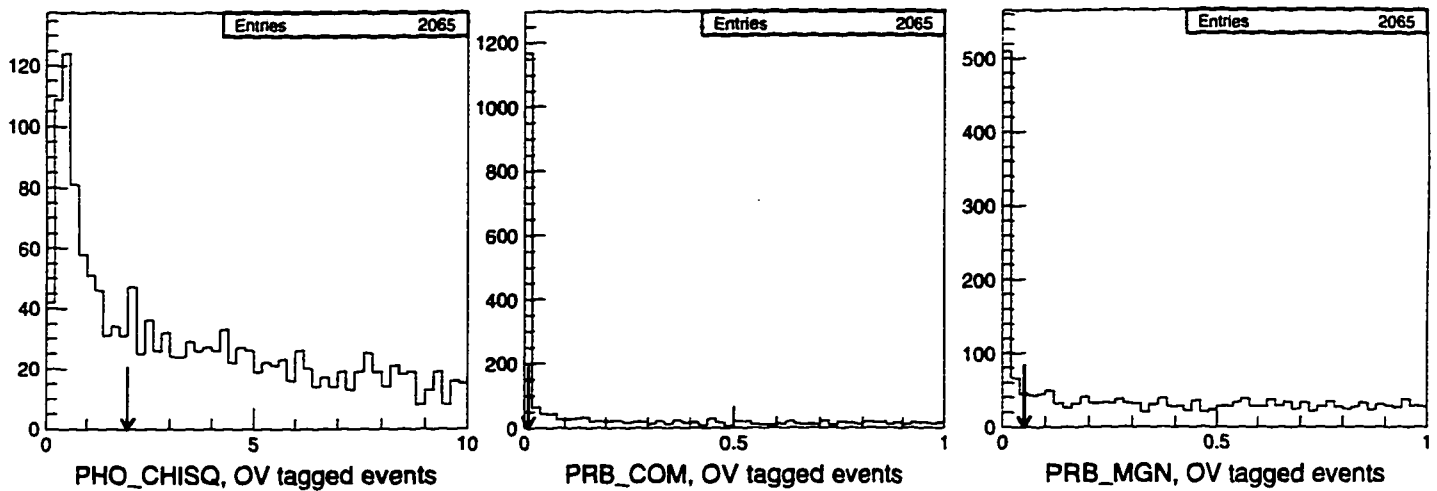


Figure 4.23: Histograms of variables with high rejection for CTEX tagged events. PHO_CHISQ measures deviations from the expected $\frac{dE}{dx}$ pattern within a charged track. PRB_COM compares the momentum and kinetic energy measurements. PRB_MGN is the confidence level of a fit to a $K_{\mu\nu\gamma}$ hypothesis. Cut positions are indicated.

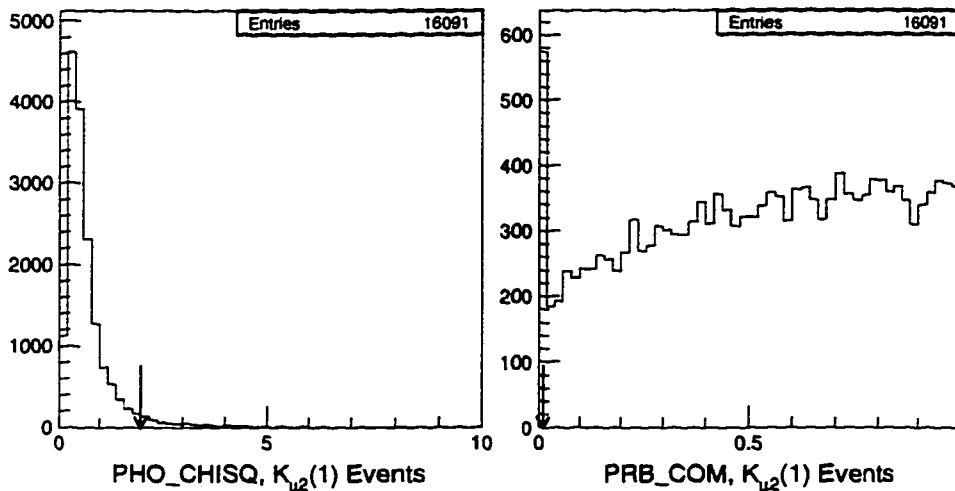


Figure 4.24: Histograms of PHO_CHISQ, PRB_COM, for $K_{\mu 2}(1)$ events. To be compared to Figure 4.23.

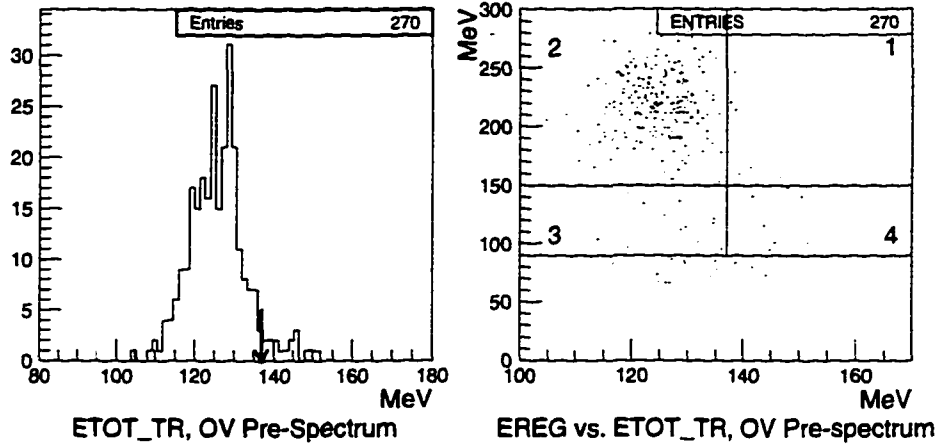


Figure 4.25: Final spectrum from overlap background study.

benign.

4.7.5 An Amusing Aside — K_{e2}

While looking at sources of mis-tagging for the CTEX tag, it was noticed that some of the events appeared consistent with events of the type $K^+ \rightarrow e^+ \nu_e$, called K_{e2} . The branching ratio of K_{e2} is quite small compared to $K_{\mu 2}$ due to helicity suppression. The momentum of the electron in K_{e2} is 246.8 MeV/c, compared to 235.5 MeV/c for $K_{\mu 2}$. The branching ratio has been measured to be [8]:

$$\text{BR}(K^+ \rightarrow e^+ \nu_e) = 1.55 \pm 0.07 \times 10^{-5}$$

A very simple analysis was done to see if a K_{e2} signal could be isolated in the $K_{\mu\nu\gamma}$ data set. K_{e2} events are able to pass the $K_{\mu\nu\gamma}$ trigger by showering in the RS and

	CTEX Tagging		Reference
N_R/N_ϵ	3.0806		4.9
N_{tag}	2068		4.25
Events	Raw (N_{surv})	Expected (N_{bkg})	
Pre-spectrum	268	825.6 ± 50.4	4.26
Region 1	6	18.5 ± 7.5	-
Region 2	222	683.9 ± 45.9	-
Region 3	14	43.1 ± 11.5	-
Region 4	7	21.6 ± 8.2	-
Region 1 + 4	13	40.0 ± 11.1	-

Table 4.11: Results from kinematic branch of overlap background study. For each type of tagging the number of events in each spectral region is shown. The expected number in each region after all cuts have been applied is obtained by multiplying by the N_R/N_ϵ normalization.

producing a high energy photon, which can then convert in the Barrel Veto. They can therefore satisfy the Barrel Veto energy requirement without depositing energy in Layer 21, which allows them to pass the $K_{\mu\nu\gamma}$ trigger quite efficiently. In fact, the trigger efficiency for K_{e2} in UMC was found to be 3.7 %, this is to be compared with the trigger efficiency for the decay the trigger was designed to find $K_{\mu\nu\gamma}(SD+)$ which is 6.7 %, and with the efficiency for a background process such as $K_{\pi2}$ which is 0.02 %.

Since the CTEX tag requires that the Range Stack track resemble a shower, it is also very effective at detecting electrons. Figure 4.26 shows the momentum spectrum at various stages of analysis. The first plot has had some simple set-up cuts and the photon vetoing applied, except for in the CTEX region. In the second the CTEX tag

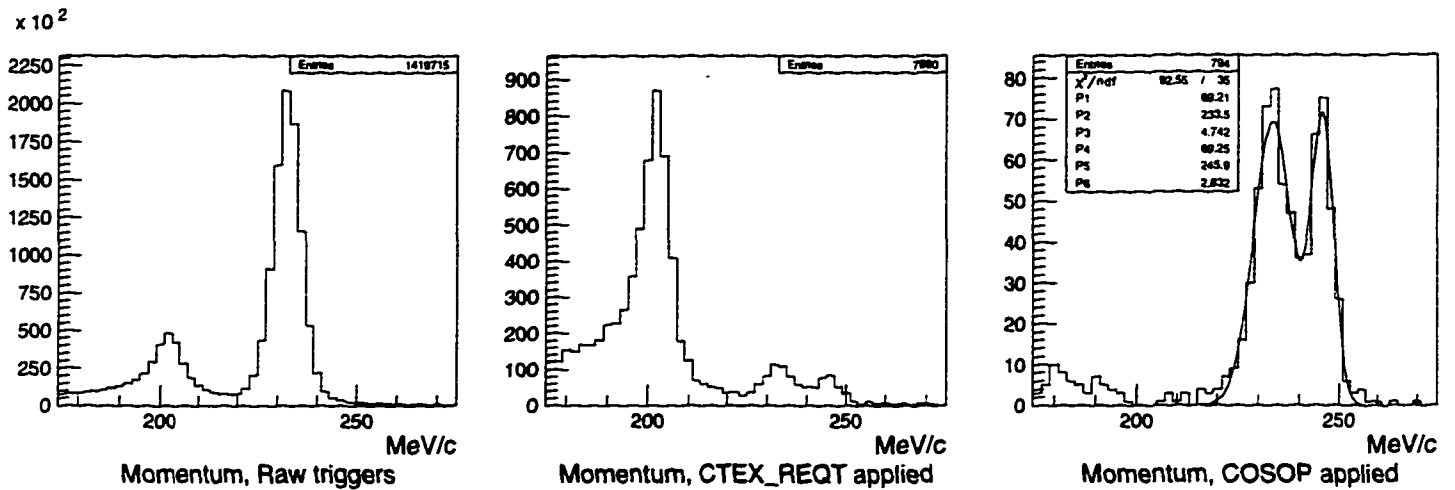


Figure 4.26: Momentum spectrum at different stages of the K_{e2} analysis. Last histogram shows prominent K_{e2} peak.

has been applied. In the third, a cut has been made on the cosine of the opening angle between the “muon” and the “photon” - COSOP:

$$\text{COSOP} > 0.5$$

This requires the cluster in the Barrel Veto to be more or less behind the charged track and therefore is an effective veto against π^0 containing events. The two peaks in the momentum distribution correspond to $K_{\mu 2}$ and K_{e2} . The number of events in the K_{e2} peak is approximately 400. For comparison, the highest number of K_{e2} events accumulated by an experiment to date is 534 [8].

To turn this peak into a branching ratio measurement would require a detailed acceptance calculation and it would probably be quite difficult to get the systematic errors on this down below the current best measurement. Nonetheless, it is interesting

to know that E787 has quite high sensitivity for this process. It may be an avenue for future study.

4.8 Final Photon Energy Cut

While most of the cuts were set to remove background events, the final cut on the measured photon energy (E_{REG_FIN}), was set so that the trigger bit (BVHI) would be fully efficient. Since the efficiency of this bit depends on the analog signal shape of the summed BV energy, it is not well simulated by UMC. We therefore measure the efficiency of the bit as a function of BV energy and place the cut at the top of the plateau. $K_{\pi^2}(1)$ and $K_{\pi^2}(2)$ events are used to produce a histogram of E_{REG} which covers the whole spectrum. Some of the $K_{\pi^2}(1)$ events had photons which converted in the RS and then splashed into the BV to provide small amounts of energy. This is shown in Figure 4.27. The E_{REG_FIN} cut is set at 90 MeV.

4.9 Summary of Background Studies

Table 4.12 gives a summary of all the numbers extracted from the background studies.

N_{surv} is the number of surviving events in Regions 1 and 4. $N_{bkg} \equiv \frac{N_R}{N_c} N_{surv}$ is the number of background events expected in those regions. Mis-tag gives the number of mis-tagged $K_{\mu\nu\gamma}$ events expected in Regions 1 and 4 and is to be compared to

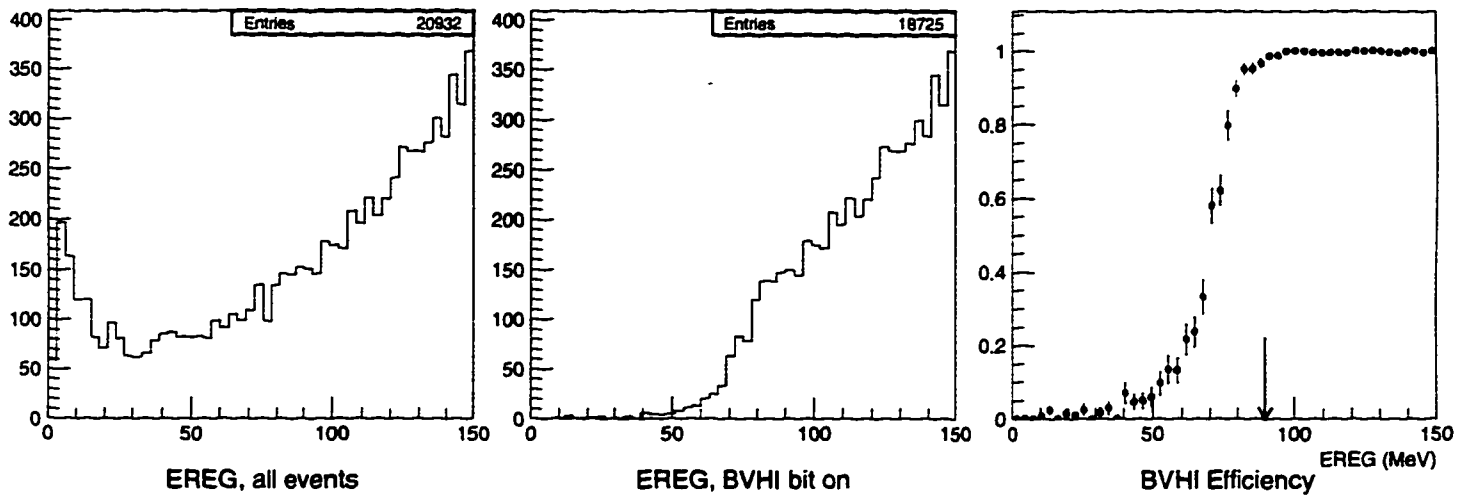


Figure 4.27: Measurement of threshold of BVHI trigger bit as a function of the measured photon energy. The arrow indicates the position of the EREG_FIN cut, which is set so that the BVHI bit is fully efficient.

Study	Tagging				Rejection			Mis-tag
	N_{setup}	N_{ϵ}	N_R	N_R/N_{ϵ}	N_{tag}	N_{surv}	N_{bkg}	
Accidental	-	33243	9600	0.2888	518431	275	79.4 ± 4.8	-
No-Overlap, EC	1677	295	319	1.0814	9289	36	38.9 ± 6.5	15.0
No-Overlap, BV	1677	545	319	0.5853	16577	43	25.2 ± 3.8	4.8
Overlap	600	124	382	3.0806	2068	13	40.0 ± 11.1	11.4

Table 4.12: Summary of all background studies.

N_{surv} . Recall that the two No-overlap studies are redundant measures of the same background

4.10 Detailed Background Study Charts

In this section I present the lists of cuts that were applied for each part of each background study. These are presented mostly for reference.

Cut Name	Events In	Events Out	Rejection
ISKCODE	1517733	1419715	1.069
EREG	1419715	1413652	1.004
TRS	1413652	1364623	1.036
COS3D	1364623	1268871	1.075
TGZ	1268871	1233706	1.029
ETGT	1233706	1146824	1.076
EIC	1146824	1110310	1.033
STLAY	1110310	1070630	1.037

Table 4.13: Setup cuts run on $K_{\mu\nu\gamma}$ triggers for all studies unless noted. Cuts are mostly of the “fiducial volume” type.

Cut Name	Events In	Events Out	Rejection
NOTPROMPT	1070630	518431	2.065

Table 4.14: NOTPROMPT cut used to tag events where photon was not in time with charged track. The result is $N_{tag,acc}$

Cut Name	Events In	Events Out	Rejection
BW1TRS	518431	348953	1.486
BW2TRS	348953	338218	1.032
FRACL	338218	101869	3.320
PRB_TU5	101869	61171	1.665
ZREG	61171	30897	1.980
RSIN	30897	29113	1.061
ECIN	29113	26905	1.082
BVIN	26905	26418	1.018
ICIN	26418	26151	1.010
VCIN	26151	26115	1.001
INTIME2	26115	23640	1.105
RDPE_EXCL	23640	23436	1.009
ETGPHO	23436	23187	1.011
RDPE_TREG	23187	22375	1.036
PHO_CHISQ	22375	21002	1.065
PRB_COM	21002	20575	1.021
PRB_MGN	20575	885	23.249

Table 4.15: Cuts applied in rejection branch of Accidental study. Includes all cuts up to final spectrum cut. The result is $N_{pre-spec,acc}$.

Cut Name	Events In	Events Out	Rejection
ISKCODE	34304	32948	1.041
EREG	32948	28651	1.150
TRS	28651	27861	1.028
COS3D	27861	26522	1.050
TGZ	26522	25796	1.028
ETGT	25796	24157	1.068
EIC	24157	23632	1.022
PROMPT	23632	22909	1.032
BW1TRS	22909	21307	1.075
BW2TRS	21307	20872	1.021
FRACL	20872	19657	1.062
PRB_TU5	19657	18591	1.057
ZREG	18591	18056	1.030
RSIN	18056	14362	1.257
ETGPHO	14362	12648	1.136
PHO_CHISQ	12648	12212	1.036
PTOT_KPI2	12212	11673	1.046
GAM_TRIG	11673	1677	6.961

Table 4.16: Cuts applied for setup of “tagging” branch of No-Overlap study. $K_{\pi^2(2)}$ triggers were used. The result is N_γ .

Cut Name	Events In	Events Out	Rejection
INTIME	1677	399	4.203
INTIME2	399	326	1.224
RDPE_EXCL	326	319	1.022

Table 4.17: Cuts applied to determine photon veto rejection. The result is N_R .

Cut Name	Events In	Events Out	Rejection
ISKCODE	95115	86814	1.096
TRS	86814	66641	1.303
COS3D	66641	64678	1.030
TGZ	64678	61484	1.052
ETGT	61484	53305	1.153
EIC	53305	51992	1.025
STLAY	51992	20215	2.572
BW1TRS	20215	18326	1.103
BW2TRS	18326	17942	1.021
PTOT_KMU2	17942	16781	1.069
GAM_TRIG	16781	16287	1.030

Table 4.18: Setup cuts for No-Overlap mis-tagging study. $K_{\mu 2}(1)$ triggers are used. The result is $N_{K_{\mu 2}, setup}$

Cut Name	Events In	Events Out	Rejection
INTIME	16287	14550	1.119
INTIME2	14550	13590	1.071
RDPE_EXCL	13590	13583	1.001
BVPE_ER	13583	13557	1.002
BVPE2_ER	13557	13538	1.001

Table 4.19: Accidental Photon Veto losses.

Cut Name	Events In	Events Out	Rejection
PROMPT	1070630	470323	2.276
BW1TRS	470323	407682	1.154
BW2TRS	407682	399017	1.022
FRACL	399017	304461	1.311
PRB_TU5	304461	276476	1.101
ZREG	276476	258861	1.068
RSIN	258861	124289	2.083
ETGPHO	124289	88034	1.412
PHO_CHISQ	88034	74373	1.184

Table 4.20: Cuts applied for setup of “rejection” branch of No-Overlap study. They are applied for both the Endcap and the Barrel Veto studies. The result is $N_{other,nov}$.

Cut Name	Events In	Events Out	Rejection
PRB_COM	9289	6564	1.415
PRB_MGN	6564	5225	1.256

Table 4.21: Pre-spectrum cuts for Endcap tagging.

Cut Name	Events In	Events Out	Rejection
PRB_COM	16577	11664	1.421
PRB_MGN	11664	9326	1.251

Table 4.22: Pre-spectrum cuts for Barrel Veto tagging.

Cut Name	Events In	Events Out	Rejection
ISKCODE	5815	5711	1.018
EREG	5711	5711	1.000
COS3D	5711	5685	1.005
ETGT	5685	4884	1.164
EIC	4884	4717	1.035
STLAY	4717	4277	1.103
PROMPT	4277	4271	1.001
BW1TRS	4271	4271	1.000
BW2TRS	4271	4271	1.000
FRACL	4271	4150	1.029
PRB_TU5	4150	4112	1.009
ZREG	4112	4067	1.011
ECIN	4067	3127	1.301
BVIN	3127	2454	1.274
ICIN	2454	2212	1.109
VCIN	2212	2152	1.028
ECIN2	2152	2099	1.025
BVIN2	2099	2099	1.000
RDPE_EXCL	2099	2091	1.004
ETGPHO	2091	1880	1.112
RSIN_CTEX	1880	974	1.930

Table 4.23: Setup cuts applied to UMC events for Overlap tagging branch. Monte Carlo $K_{\pi 2}$ and $K_{\mu 3}$ events are used. The result is $N_{setup,ov}$.

Cut Name	Events In	Events Out	Rejection
ISKCODE	95115	86814	1.096
TRS	86814	66641	1.303
COS3D	66641	64678	1.030
TGZ	64678	61484	1.052
ETGT	61484	53305	1.153
EIC	53305	51992	1.025
STLAY	51992	20215	2.572
BW1TRS	20215	18326	1.103
BW2TRS	18326	17942	1.021
PTOT_KMU2	17942	16781	1.069
GAM_TRIG	16781	16287	1.030
ECIN	16287	15195	1.072
BVIN	15195	15193	1.000
ICIN	15193	14968	1.015
VCIN	14968	14958	1.001
RSIN_CTEX	14958	14733	1.015
PHO_CHISQ	14733	13949	1.056

Table 4.24: Setup cuts applied to $K_{\mu 2}(1)$ events in Overlap mis-tagging study.

Cut Name	Events In	Events Out	Rejection
PROMPT	1070630	470323	2.276
BW1TRS	470323	407682	1.154
BW2TRS	407682	399017	1.022
FRACL	399017	304461	1.311
PRB_TU5	304461	276476	1.101
ZREG	276476	258861	1.068
ECIN	258861	186851	1.385
BVIN	186851	116818	1.600
ICIN	116818	99660	1.172
VCIN	99660	95857	1.040
ECIN2	95857	88337	1.085
BVIN2	88337	86475	1.022
RDPE_EXCL	86475	85733	1.009
ETGPHO	85733	73355	1.169
RSIN_CTEX	73355	41812	1.754
CTEX_REQT	41812	2068	20.219

Table 4.25: Cuts applied to tag overlap events. The result is $N_{tag,ov}$.

Cut Name	Events In	Events Out	Rejection
PRB_MGN	2068	1454	1.422
PRB_COM	1454	748	1.944
PHO_CHISQ	748	268	2.791

Table 4.26: Pre-spectrum cuts applied to CTEX_REQT tagged events.

Spectrum Analysis

Once all of the background studies have been completed, the final event sample can be selected using the cuts determined by those studies. Since we expect this sample to contain a large component of Inner Bremsstrahlung events, we must develop methods to determine whether the sample is composed solely of IB or if there is a Structure Dependent contribution. Since the IB spectrum and branching ratio are well known, we could, in principle, simply calculate the number of IB events we expect in the final sample and compare that to the number observed. However, this method would require precise knowledge of the K^+ flux, reconstruction efficiency and numerous other poorly known factors to calculate an absolute number of IB events.

A better method, and the one we use, is to choose a kinematic variable (such as photon energy) for which the IB and Structure Dependent components have strongly differing distributions. We use the UMC simulation to produce distributions of this variable for each component. We then find the relative strengths of the components

that gives the best fit to the observed distribution. This will yield a branching ratio of SD^+ relative to IB. We are, in effect, normalizing to the known IB branching ratio. Many of the poorly known factors are then irrelevant since they will be the same for the SD^+ and IB components and therefore cancel. For example, it is not necessary to know even the K^+ flux. The main source of systematic error on the SD^+ branching ratio will be inadequacies in the UMC simulation of the detector that cause the relative acceptance between SD^+ and IB components to be inaccurately simulated.

Later, after the fit is done and the Structure Dependent branching ratio calculated, we can use the known K^+ flux to calculate the measured IB branching ratio and use this as a cross-check of the whole procedure.

This chapter will describe the production of the final spectrum, the fitting of this spectrum to different components of $K_{\mu\nu\gamma}$, and various checks of the whole procedure including an estimation of the systematic error associated with it.

5.1 Constructing the Final Spectrum

The first step in the procedure is to apply all the cuts to the full data set to produce the final event sample. The spectrum of this sample is shown in Figure 5.1 and the cuts that led to the sample is shown in Table 5.8. There is a large component of π^0 containing events in region 2 as expected from the π^0 background studies. There is also a large IB component which appears as a band at low photon energy. For the

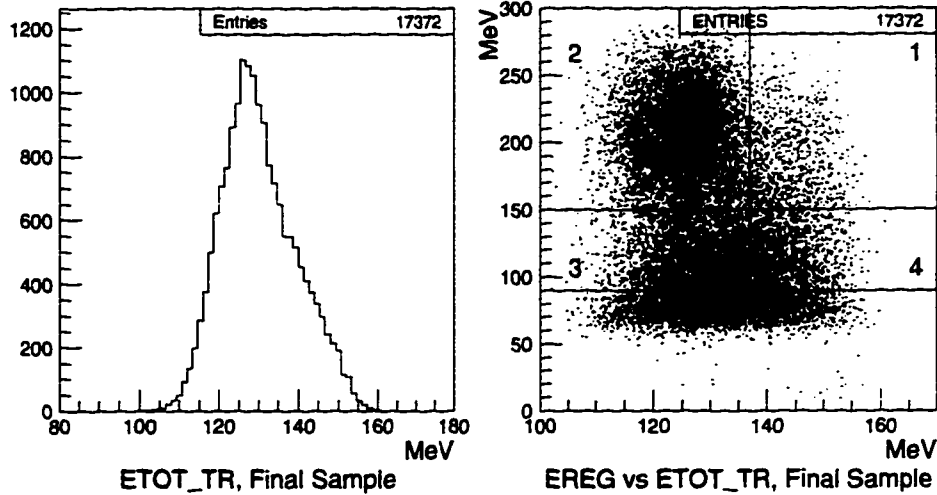


Figure 5.1: Event sample after applying all cuts except the final spectrum cuts.

rest of the analysis, we will be concerned only with events falling in regions 1 and 4 — a total of 2693 events.

While we have applied cuts to remove as much background as possible from this spectrum, we know that small residual backgrounds exist. While we do not know which specific events came from background we can remove background on a statistical basis by subtracting the scaled spectra measured in the background studies from the measured spectrum. The resulting spectrum is called the background-subtracted spectrum. The contents, s_i , of each bin and the error associated with it, e_i , are then given by:

$$s_i = x_i - \sum_{j=1}^m w_j y_{ij}; \quad e_i = \left[x_i + \sum_{j=1}^m w_j^2 y_{ij} \right]^{\frac{1}{2}},$$

where x_i is the spectrum of the raw data, w_j and y_{ij} are the weight and spectrum

associated with the j^{th} background source and m is the number of background sources. The background spectra used were from the Accidental, the Barrel Veto Tagging No-Overlap, and the Overlap background study. Note that the subtraction assumes that the normalization of each background is known perfectly. Uncertainties in the background normalization will be treated in the section on systematic errors.

5.2 Opening Angle Fitting

As a first step in determining what $K_{\mu\nu\gamma}$ components are present in the final spectrum, it is useful to do a fit to a one dimensional histogram assuming that only IB and SD^+ are present. The choice of which kinematic variable to use in the fit is driven by the power it has to distinguish IB from SD^+ . The cosine of the opening angle between the muon and photon (COSOP) is found to have particularly good distinguishing power as shown in Figure 5.2. The cuts applied to the UMC generated data are the same as those applied to the data and are shown in Tables 5.9 and 5.10. Figure 5.3 shows the COSOP distribution for the raw data and for the sum of the three background sources, and the data after background subtraction.

We now wish to find the combination of IB and SD^+ that best fits the background-subtracted distribution. Since we are not interested, at this point, in the overall normalization, we normalize the data and UMC histograms to unit area. We can then write an arbitrary combination p_i of the two UMC components as:

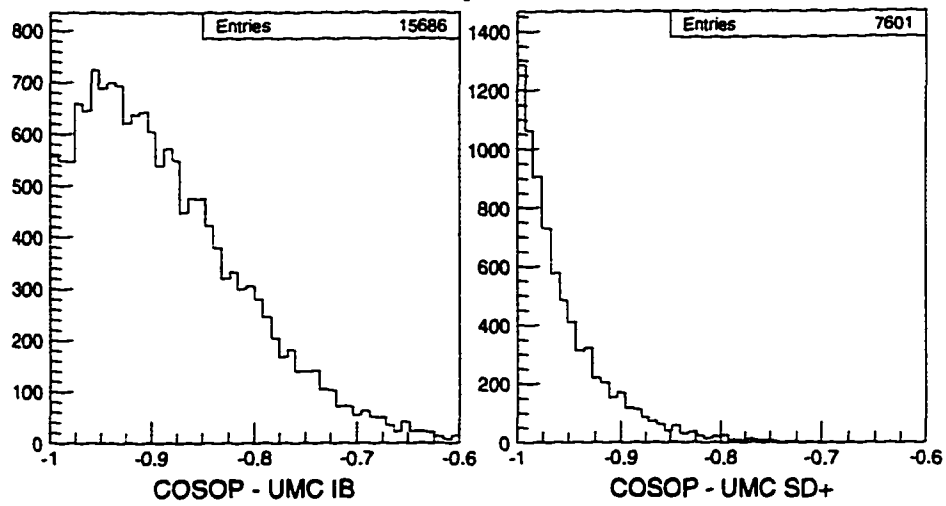


Figure 5.2: Cosine of opening angle between muon and photon (COSOP) for UMC simulated IB and SD^+ components of $K_{\mu\nu\gamma}$ in spectral regions 1 and 4.

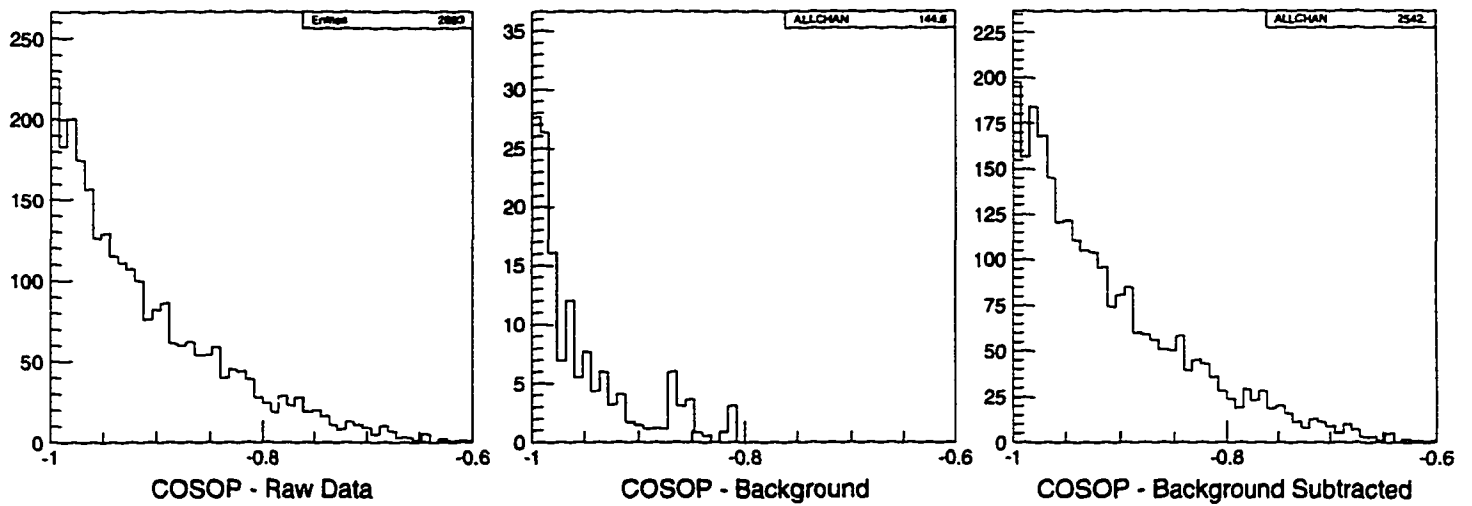


Figure 5.3: COSOP distributions for raw data, the sum of the backgrounds, and background subtracted data.

$$p_i = \frac{1}{1+\gamma} y_i + \frac{\gamma}{1+\gamma} z_i,$$

where y_i and z_i are the unit-normalized IB and SD^+ spectra and γ is the ratio of the two components.

This composite spectrum is then automatically normalized and we can form a χ^2 between it and the normalized measured spectrum, s_i .

$$\chi^2 = \sum_{i=1}^N \frac{(p_i - s_i)^2}{e_i^2} = \sum_{i=1}^N \frac{\left(\left(\frac{1}{1+\gamma} y_i + \frac{\gamma}{1+\gamma} z_i \right) - s_i \right)^2}{e_i^2},$$

where N is the number of bins in the spectrum, e_i is the error of the measured spectrum, normalized by the same factor as the s_i was. The UMC spectra are assumed to have no statistical error associated with them. In practice, this is achieved by using a UMC sample that is approximately ten times larger than the data sample.

We then wish to minimize this χ^2 with respect to γ . This can be done analytically by differentiating with respect to γ (all the other terms are constants), setting equal to 0 and solving for γ . We find:

$$\gamma = \frac{\sum_{i=1}^N \frac{(y_i - s_i)(z_i - y_i)}{e_i^2}}{\sum_{i=1}^N \frac{(s_i - z_i)(z_i - y_i)}{e_i^2}}$$

The error on γ can then be calculated as follows:

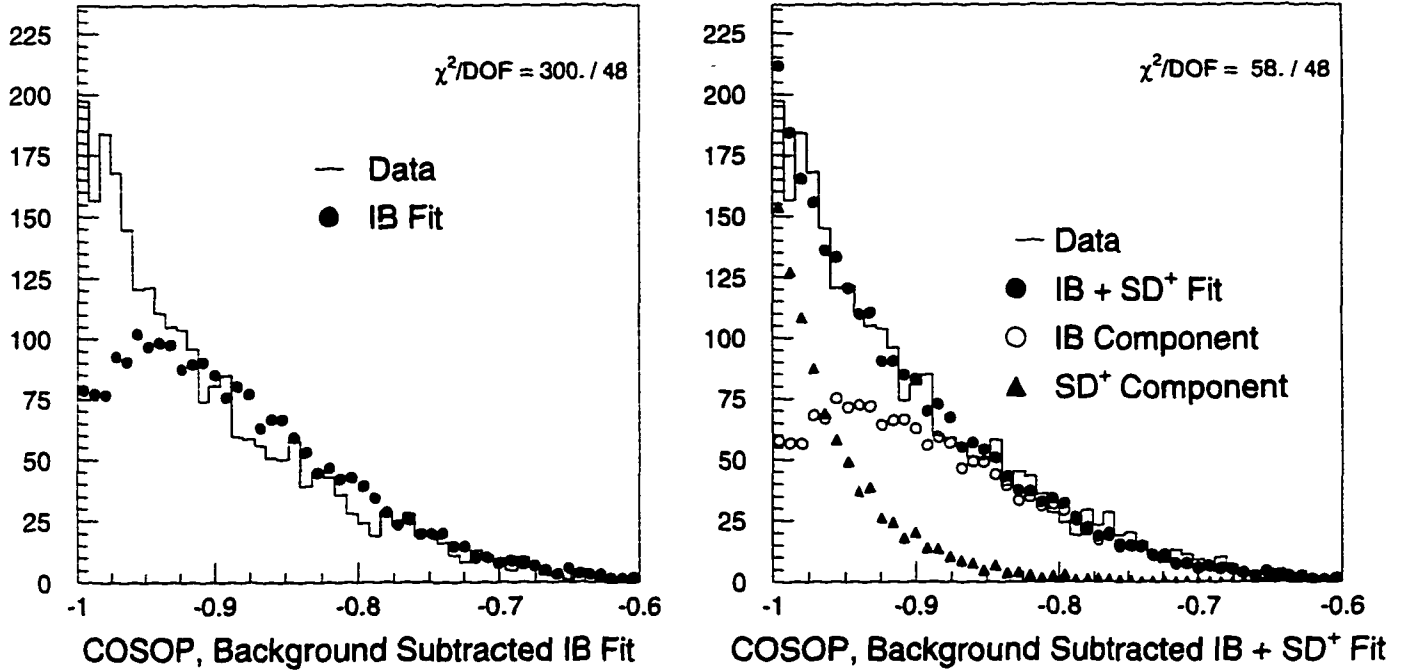


Figure 5.4: Fits of the data COSOP distribution to UMC generated distributions. The first plot uses only the Inner Bremsstrahlung component. The second plot uses both an IB and an SD⁺ component.

$$\begin{aligned}\sigma_\gamma^2 &= \sum_{i=1}^N \left(e_i \frac{\partial \gamma}{\partial s_i} \right)^2 \\ &= \sum_{i=1}^N \left((1 + \gamma)(y_i - z_i) / e_i \sum_{j=1}^N \frac{(s_j - y_j)(z_j - y_j)}{e_j^2} \right)^2\end{aligned}$$

Figure 5.4 shows fits to the background subtracted COSOP distribution. The range of COSOP that is used in the fit is the same as is displayed, $-1. < \text{COSOP} < -0.6$. The IB component alone clearly does not fit the data well, whereas the fit becomes quite good when the SD⁺ component is added.

The fit parameter γ tells us the ratio of the number of SD⁺ events in the final

Parameter	Value
$N_{gen,IB}$	8.390×10^6
N_{gen,SD^+}	3.000×10^5
$N_{spec,IB}$	15686
N_{spec,SD^+}	7601

Table 5.1: Constants used to convert fitted γ to SD^+ branching ratio.

sample N_{SD^+} to the number of IB events in the final sample N_{IB} . We can calculate the SD^+ branching ratio in terms of the this ratio by noting:

$$\frac{BR(IB)\epsilon_{IB}}{N_{IB}} = \frac{BR(SD^+)\epsilon_{SD^+}}{N_{SD^+}},$$

where ϵ_{IB} and ϵ_{SD^+} are given by:

$$\epsilon_{IB} = \frac{N_{spec,IB}}{N_{gen,IB}}; \quad \epsilon_{SD^+} = \frac{N_{spec,SD^+}}{N_{gen,SD^+}},$$

where $N_{gen,IB}$ and N_{gen,SD^+} are the number of IB and SD^+ events generated by UMC and $N_{spec,IB}$ and N_{spec,SD^+} are the number of these events in the final spectrum. The numerical values of these parameters are given in Table 5.1.

The SD^+ branching ratio then becomes:

$$BR(SD^+) = BR(IB)\gamma \frac{N_{spec,IB}}{N_{gen,IB}} \frac{N_{gen,SD^+}}{N_{spec,SD^+}},$$

The numerical values for the calculation are given in Table 5.2.

Parameter	Value
γ	0.5617
σ_γ	0.0510
χ^2/DOF	57.68 / 48
BR(IB)	3.300×10^{-4}
BR(SD ⁺)	$(1.368 \pm 0.124) \times 10^{-5}$
N_{IB}	1631.8 ± 53.3
N_{SD^+}	916.6 ± 53.3

Table 5.2: COSOP Fitting Numbers. Note that BR(IB) is the theoretical value which is used as a normalization.

5.3 Two Dimensional Fitting

From the two-component fit to COSOP it is clear that the Inner Bremsstrahlung component alone is not capable of fitting the data and that adding SD⁺ greatly improves the fit. Nevertheless, the fit is incomplete for two reasons. The first is that the presence of an SD⁺ component necessarily implies the presence of an interference component between the SD⁺ and the IB components. Since the magnitude of the INT⁺ term is proportional to the square root of the magnitude of the SD⁺ term, the fit becomes non-linear. Such non-linearity is difficult to accommodate in the framework of the fit that was done on the COSOP distribution. The second reason that the COSOP fit is incomplete is that it ignores the possibility of an INT⁻ contribution to the distribution. ¹ The shape of COSOP distribution for INT⁻ is quite similar to that of SD⁺, as can be seen in Figure 5.5. In fact, a fit to background subtracted COSOP

¹The SD⁻ component could also be included in the fit, but its magnitude in the relevant region of phase space is negligibly small and so it is left out of the fit.

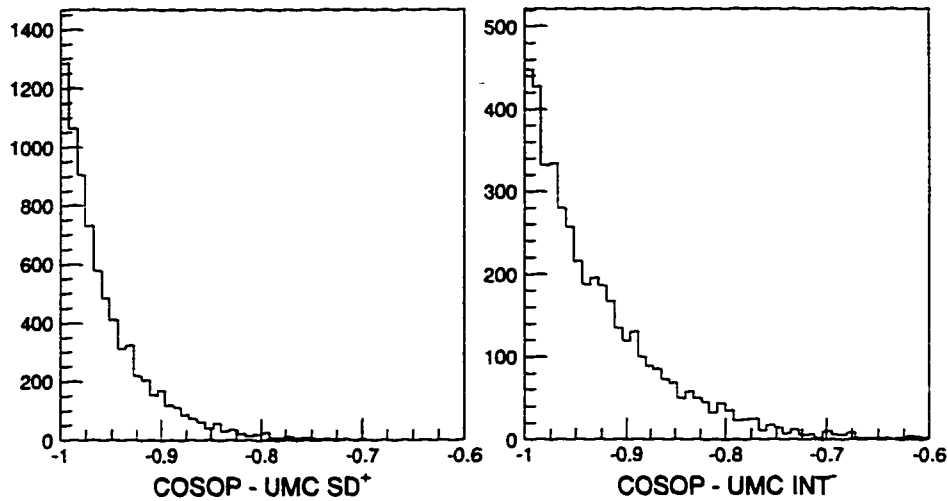


Figure 5.5: COSOP distributions generated by UMC for SD^+ and INT^- . Distributions are quite similar in appearance.

spectrum using IB and INT^- gives only a slightly worse χ^2 than that from the fit to IB and SD^+ .

In contrast to the COSOP distribution, however, the two-dimensional distribution of fitted photon energy (EREG_FIT) vs. muon energy (ETOT_TR) looks quite different for SD^+ and INT^- , as shown in figure 5.6. We use the fitted photon energy, EREG_FIT, rather than the raw measured photon energy, EREG, due to its somewhat better resolution. The cuts used to produce the final INT^- and INT^+ samples are shown in Table 5.11 and Table 5.12. This spectrum is also quite good at distinguishing the backgrounds from the signal as shown in figure 5.7.

To do the fit we again wish to form an arbitrary combination of the components. The parameters of this combination, rather than just being the ratio of the SD^+ component to the IB component, will be the form factors $F_V + F_A$ and $F_V - F_A$. The

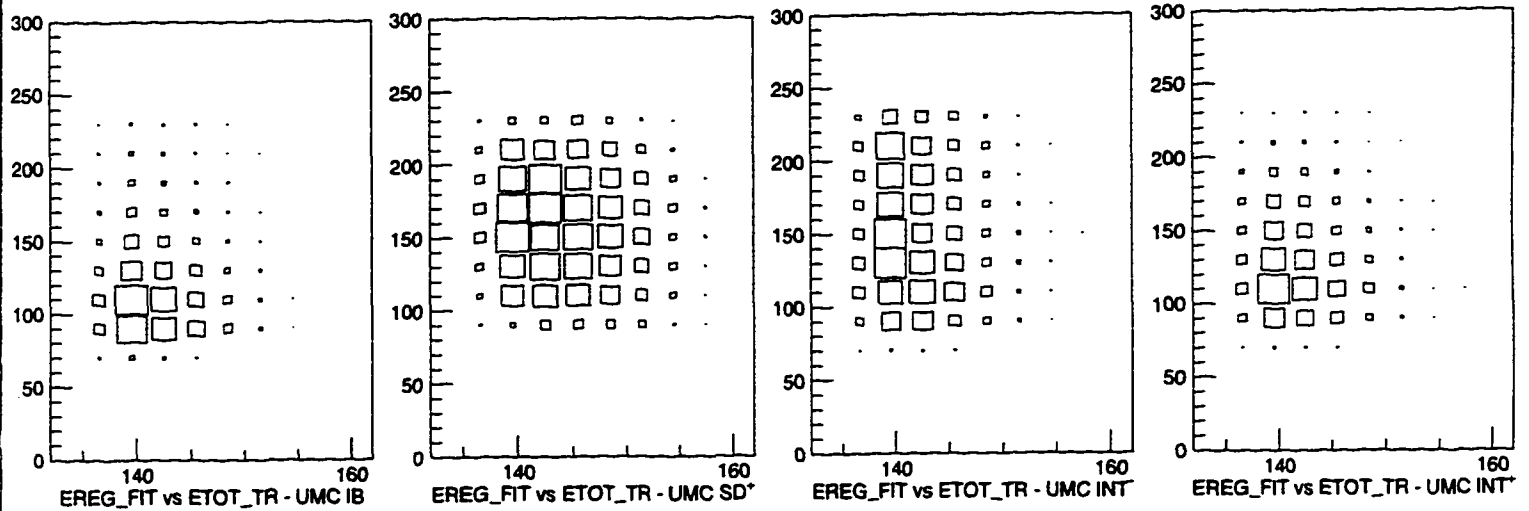


Figure 5.6: EREG_FIT vs. ETOT_TR distributions for UMC generated IB, SD⁺, INT⁻ and INT⁺ components.

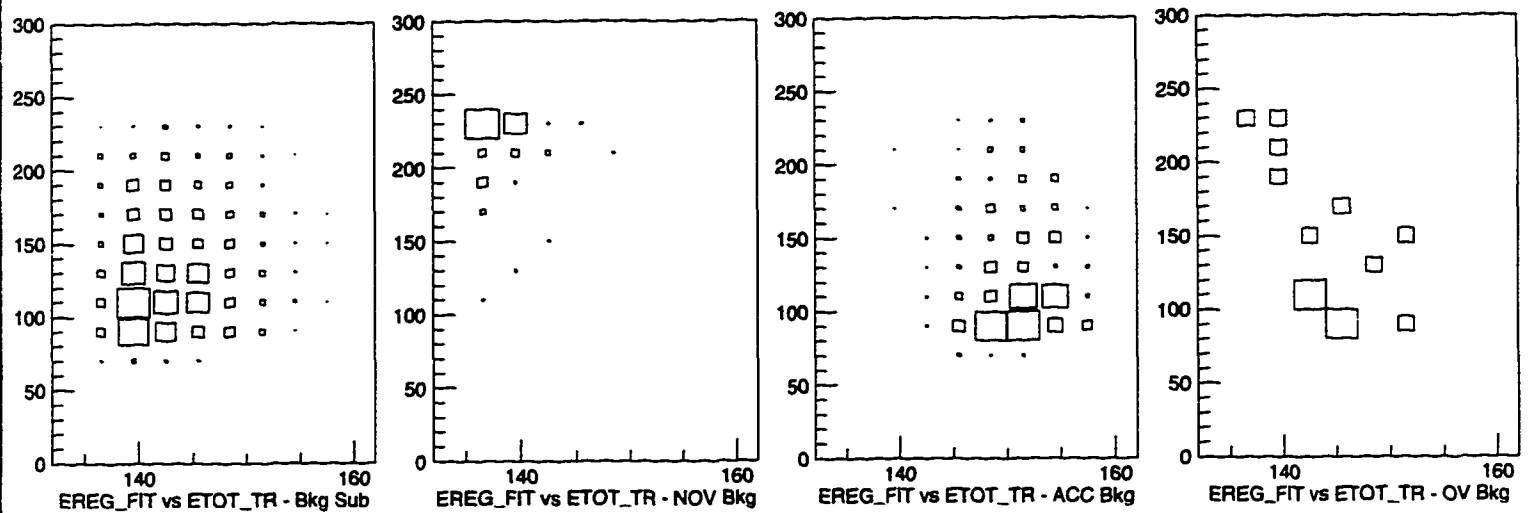


Figure 5.7: EREG_FIT vs. ETOT_TR distributions for background subtracted data, No Overlap background, Accidental background and Overlap background.

first step is to form a spectrum where the UMC components are correctly normalized relative to each other for given values of the parameter, $F_V + F_A$ and $F_V - F_A$. This involves calculating branching ratios for each component for the parameters and dividing by the number of events of each component that were generated in UMC. The relatively normalized spectrum, p_i , thus takes the form: ²

$$p_i = \frac{BR_{IB}}{N_{gen,IB}} IB_i + \frac{BR_{SD^+}}{N_{gen,SD^+}} SD_i^+ + \frac{BR_{INT^+}}{N_{gen,INT^+}} INT_i^+ + \frac{BR_{INT^-}}{N_{gen,INT^-}} INT_i^-,$$

where, for example, BR_{SD^+} is the branching ratio for the SD^+ component and SD_i^+ is the spectrum of the SD^+ component. The branching ratio of each component is then written in terms of the form factors, so that p_i becomes:

$$p_i = \frac{C_{IB}}{N_{gen,IB}} IB_i + \frac{C_{SD^+}(F_V + F_A)^2}{N_{gen,SD^+}} SD_i^+ + \frac{C_{INT^+}(F_V + F_A)}{N_{gen,INT^+}} INT_i^+ + \frac{C_{INT^-}(F_V - F_A)}{N_{gen,INT^-}} INT_i^-,$$

where, for example C_{SD^+} is the constant needed to find the branching ratio of the SD^+ component for a given value of $F_V + F_A$. The constants C and N_{gen} for each component are tabulated in Table 5.3.

We then normalize p_i to unit area and again form the χ^2 between it and the normalized data histogram s_i :

$$\chi^2 = \sum_{i=1}^N \frac{(p_i - s_i)^2}{e_i^2},$$

²Even though p_i is representing a two-dimensional histogram, a second index is not needed, since i is just a bin label.

Component	C	N_{gen}
IB	3.300×10^{-4}	8.390×10^6
SD ⁺	4.912×10^{-4}	3.050×10^5
INT ⁺	1.022×10^{-4}	4.932×10^6
INT ⁻	6.813×10^{-4}	5.809×10^6

Table 5.3: C and N_{gen} numbers used in two-dimensional fit.

where again s_i and e_i are the normalized data and error histograms.

We then wish to minimize this χ^2 with respect to $F_V + F_A$ and $F_V - F_A$. Due to the non-linearity introduced by the INT⁺ term, this cannot be done analytically. Rather we employ the non-linear fitter MINUIT [28] to do the χ^2 minimization.

Figure 5.8 shows the contours of χ^2 from the fit. There are two minima present: one at positive values of $F_V + F_A$ and one at negative values. The minima at negative values is slightly lower (by about one unit of χ^2) but not significantly so. Since the SD⁺ component depends on $(F_V + F_A)^2$ it is independent of the sign of $F_V + F_A$. The only sign dependence is coming through the INT⁺ component. This contribution is not large enough to allow us to distinguish between positive and negative values of $F_V + F_A$. So, the quoted value is the absolute value of $F_V + F_A$:

$$|F_V + F_A| = 0.165 \pm 0.007$$

The error is determined by going to the extreme possible values of $F_V + F_A$ which lie on the $+1 \chi^2$ contour and is statistical only. Systematic errors will be discussed in

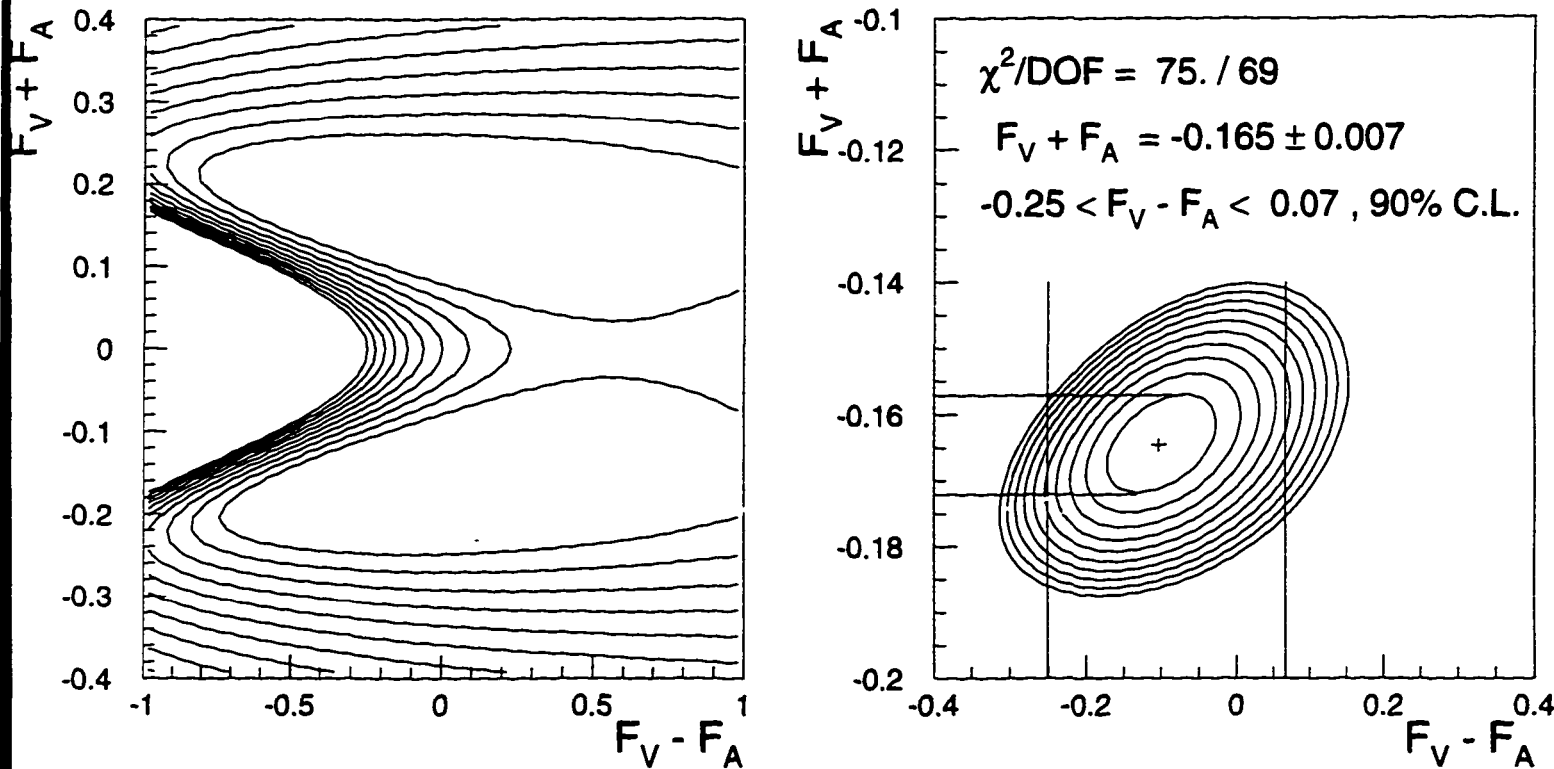


Figure 5.8: χ^2 contours for the two-dimensional fit. The first plot is of the whole range of plausible values of the form factors. Each contour represents 50 units of χ^2 . The second plot narrows the focus to the χ^2 minimum. In this plot, each contour corresponds to one unit of χ^2 . The one standard deviation uncertainty for $F_V + F_A$ and the 90% confidence limit for $F_V - F_A$ are shown.

Parameter	Value
χ^2/DOF	75.113 / 69
$F_V + F_A$	-0.165 ± 0.007
$F_V - F_A$	-0.102 ± 0.074
$BR(SD^+)$	$(1.331 \pm 0.120) \times 10^{-5}$
N_{IB}	1805.2 ± 138.2
N_{SD^+}	970.3 ± 87.7

Table 5.4: Numbers extracted from the two-dimensional fit of Figure 5.8.

the following sections. This $|F_V + F_A|$ measurement corresponds to a measurement of the branching ratio of the SD^+ component of:

$$BR(SD^+) = (1.331 \pm 0.120) \times 10^{-5}$$

The effect of the INT^- component is also not quite large enough to be seen. The “measurement” of $F_V - F_A$ is not significantly different from zero. The best we can do is to place a 90% confidence level on its value. This is done by finding the extreme points of the $+4.61 \chi^2$ contour, which corresponds to the 90% confidence level contour for a χ^2 with two degrees of freedom. The quoted value is

$$-0.25 < F_V - F_A < 0.07, 90\%C.L.$$

The results of this fit are tabulated in Table 5.4.

As a check of the fit we can compare the one-dimensional histograms of the best fit spectrum to those of the background-subtracted spectrum for a number of different variables. A few of these are shown in Figure 5.9. We see that there is quite good

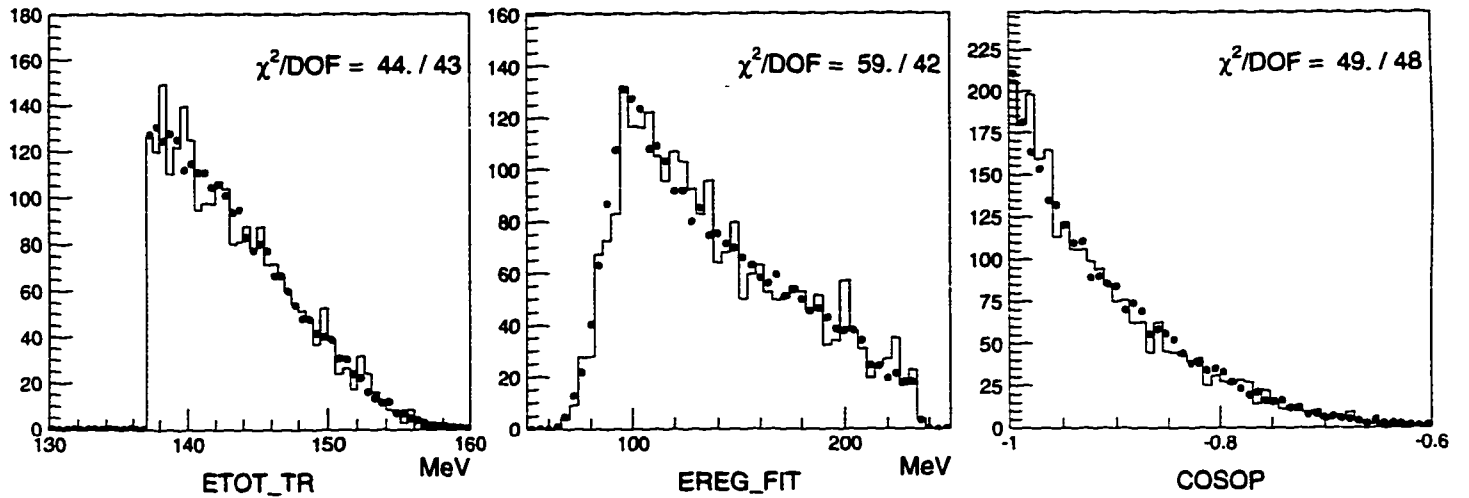


Figure 5.9: Comparison of data spectrum to one composed of $K_{\mu\nu\gamma}$ components weighted by the values of $F_V - F_A$ and $F_V + F_A$ found in the fit to the EREG_FIT vs. ETOT_TR spectrum. In each case the solid histogram is the background-subtracted data and the dots are the $K_{\mu\nu\gamma}$ spectrum.

agreement in all cases.

5.4 Check of Inner Bremsstrahlung Branching Ratio

As a check of the fitting procedure, we can use the number of Inner Bremsstrahlung events observed to get an absolute measure of the IB branching ratio. Note that this measurement is not needed in the calculation of the SD^+ branching ratio, but provides a useful check of the whole procedure. We will use the $K_{\mu 2}(1)$ monitors that were taken at the same time as the main data set to “count” the number of $K_{\mu 2}$ events that occurred and use this number to calculate an absolute IB Branching Ratio. By

applying many of the same cuts to the $K_{\mu 2}(1)$ sample as we did to the main data set, we can automatically account for any acceptance loss due to these cuts.

We can find the IB branching ratio with the following equation:

$$\frac{N_K BR(IB) A_{IB}}{N_{IB}} = \frac{N_K BR(K_{\mu 2}) A_{K_{\mu 2}}}{N_{K_{\mu 2}}},$$

where N_K is the number of kaons in the sample, $BR(IB)$ is the branching ratio of the IB component, A_{IB} is the acceptance for the IB component and N_{IB} is the number of IB events observed. Solving for $BR(IB)$ we find:

$$BR(IB) = BR(K_{\mu 2}) \frac{N_{IB}}{N_{K_{\mu 2}}} \frac{A_{K_{\mu 2}}}{A_{IB}}$$

Since the acceptance comes in only in the ratio $A_{K_{\mu 2}}/A_{IB}$, many acceptance factors that are common to both analyses will cancel. These include accidental photon veto losses, beam system losses, and charged track reconstruction losses. For acceptance factors that do depend on the decay type, such as charged track energy cuts, we will rely on the UMC simulation. Fortunately, these factors are just those that we expect UMC to do a good job of simulating. We call the acceptances as measured in UMC $A_{IB,UMC}$ and $A_{K_{\mu 2},UMC}$.

Unlike the charged track acceptance cuts, the photon requirement cuts will not be addressed by the $K_{\mu 2}$ analysis. Any difference between the UMC simulation of the photon and the real data will therefore not be properly taken into account. ³ For

³The largest known difference involves the PRB.TU5 cut which looks at timing consistency

these, we will make a small correction to A_{IB} based on $K_{\mu 2}$ data,

$$A_{IB} = \epsilon_{\gamma} A_{IB,UMC}$$

where ϵ_{γ} is this relative efficiency of the photon cuts in data and UMC.

Another correction to the above equation is that $K_{\mu 2}(1)$ monitors are “prescaled” by a large factor, P , before being written to tape and so the number of $K_{\mu 2}$ events should be scaled up by this number. We therefore have:

$$BR(IB) = BR(K_{\mu 2}) \frac{N_{IB}}{PN_{K_{\mu 2}}} \frac{A_{K_{\mu 2},UMC}}{\epsilon_{\gamma} A_{IB,UMC}}$$

Figure 5.10 illustrates the structure of this measurement. The $BR(IB)$ that we measure should be compared to the theoretical value corresponding to the conditions under which the UMC data was generated. Recall from Section 2.10 that the conditions for the IB component were

$$E_{\mu} > 100 \text{ MeV}, E_{\gamma} > 20 \text{ MeV}$$

This corresponds to $BR(IB) = 3.300 \times 10^{-4}$.

5.4.1 Calculation of $N_{K_{\mu 2}}$

$N_{K_{\mu 2}}$ is the number of $K_{\mu 2}$ events in the $K_{\mu 2}(1)$ monitor set which pass all of the cuts related to the charged track, the beam system and the photon veto – i.e. all cuts between the BV counters making up a photon. Since the UMC timing is essentially perfect, this cuts very few UMC events. However, in real data, it cuts approximately 5%.

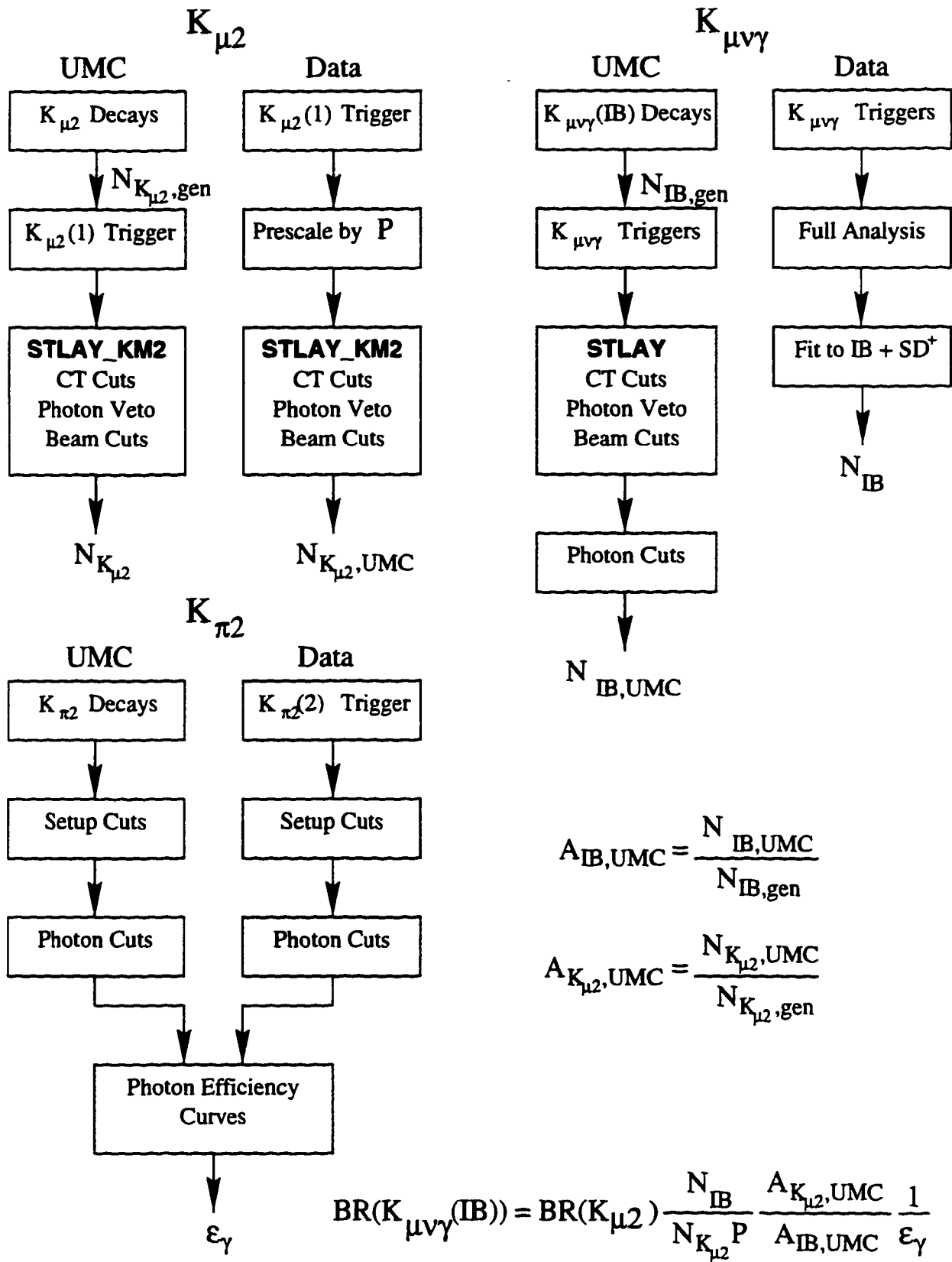


Figure 5.10: Structure of IB branching ratio calculation.

except those pertaining to the BV photon requirement. The cuts applied include a number of trigger requirements that are applied in the $K_{\mu\gamma}$ trigger but not in the $K_{\mu 2}(1)$ trigger. These include DELCO — the delayed coincidence in the trigger and GAM_TRIG which is the AND of all of the photon vetoes used in the trigger. The μ^+ is required to stop before reaching layer 21, so that we can be sure it is “contained” in the RS. By applying all of the charged track cuts to this normalization sample we automatically account for differences between their acceptance on real events and on UMC generated events. While it is possible that some of these cuts will have μ^+ energy dependence and will therefore have different acceptances for the $K_{\mu 2}$ events than for the IB events, these differences should be minimal. The list of cuts that were applied to the $K_{\mu 2}(1)$ sample is shown in Table 5.13.

5.4.2 Calculation of $A_{K_{\mu 2}, UMC}$ and $A_{IB, UMC}$

We then calculate the acceptance of these same cuts on UMC generated $K_{\mu 2}$ events that pass the $K_{\mu 2}(1)$ trigger. The number of $K_{\mu 2}$ events generated is called $N_{K_{\mu 2}, gen}$ and the number passing all of the $K_{\mu 2}$ cuts is called $N_{K_{\mu 2}, UMC}$. We then calculate $A_{K_{\mu 2}, UMC}$ as

$$A_{K_{\mu 2}, UMC} = \frac{N_{K_{\mu 2}, UMC}}{N_{K_{\mu 2}, gen}}$$

A similar procedure is then used to calculate A_{IB} . Except that here, *all* of the cuts, including those having to do with the required BV photon are applied:

$$A_{IB,UMC} = \frac{N_{IB,UMC}}{N_{IB,gen}}$$

The list of cuts leading to $N_{IB,UMC}$ is shown in Table 5.9.

5.4.3 Check of Prescale Factor

The prescale factor P was set at the time of the data taking. To check this, a scaler of raw $K_{\mu 2}(1)$ triggers was compared to the number of $K_{\mu 2}(1)$ events written to tape and found to be consistent with the nominal prescale factor. To check that the $K_{\mu 2}(1)$ monitor events covered the same data taking periods as the main data, the total number of KB's observed while the detector was live (KB_{live}) in each sample was compared. For the main data, the total of KB_{live} was 9.1771×10^9 , and for the $K_{\mu 2}(1)$ sample it was 9.1768×10^9 .

5.4.4 Calculation of ϵ_γ

To calculate ϵ_γ , which measures the difference in efficiency of the photon cuts between data and UMC, we use $K_{\pi 2}$ events. In data we use the $K_{\pi 2}(2)$ monitors, and in UMC we use $K_{\pi 2}$ decays that passed the $K_{\pi 2}(1)$ trigger. Setup cuts are applied to ensure that the events are really $K_{\pi 2}$ decays. Tables 5.15 and 5.16 show the effect of these cuts for data and UMC. The EREG2 cut is then applied which requires that the second photon from π^0 also be found in the BV. Tables 5.17 and 5.18 show the effect of this

cut.

Histograms are then made of EREG_CALC — the calculated photon energy based on the π^+ energy and the opening angle between the photon and the π^+ . This variable is used because it is independent of the BV measurement of the photon energy and so should not bias cuts which are based on this measurement. Each event enters into this histogram twice — once using the higher energy photon and once using the lower energy photon. This allows the low photon energy region to be explored with photons coming from a π^0 and is the reason that the EREG2 cut was applied.

The photon cuts are then applied and the efficiency of all the photon cuts as a function of photon energy is plotted. Tables 5.19 and 5.20 show the effect of these cuts. The efficiency in data in each bin of is then divided by that of the same bin in UMC. This plot is checked for flatness and an average relative efficiency (ϵ_γ) calculated. Figure 5.11 shows this graphically. ϵ_γ is found to be 0.926 .

5.4.5 Calculation of IB Branching Ratio

After plugging in the expressions for $A_{K_{\mu 2}}$ and A_{IB} , we have:

$$BR(IB) = BR(K_{\mu 2}) \frac{N_{IB}}{PN_{K_{\mu 2}}} \frac{N_{K_{\mu 2}, UMC}}{N_{K_{\mu 2}, gen}} \frac{N_{IB, gen}}{N_{IB, UMC}} \frac{1}{\epsilon_\gamma}$$

Table 5.5 shows the numerical values of the parameters in the calculation of the

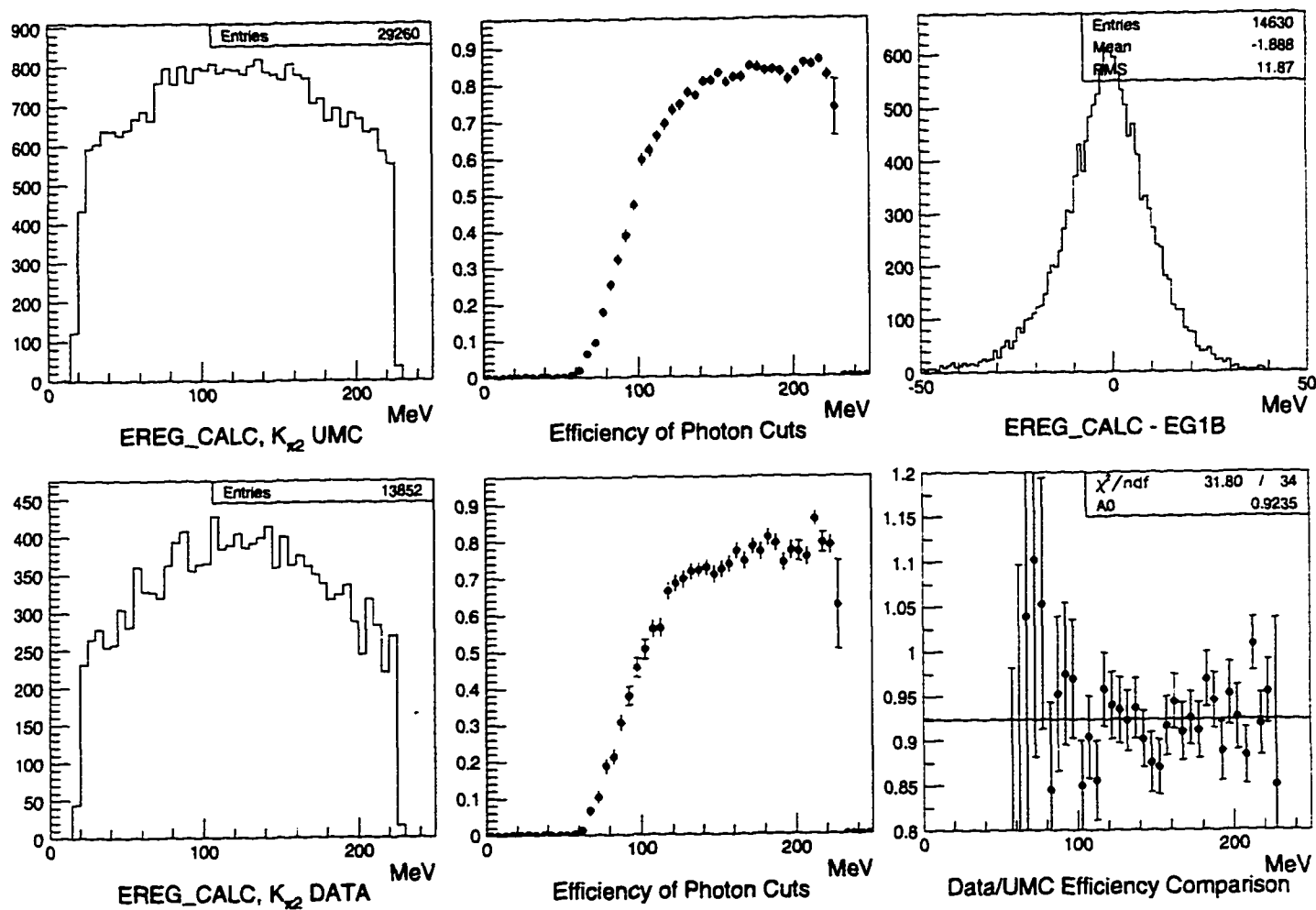


Figure 5.11: Study of relative efficiency of photon cuts as a function of energy. The first column shows raw $EREG_CALC$ histograms for UMC and data. The second column shows the efficiency of the photon cuts as a function of $EREG_CALC$ for UMC and data. The last plot in the first row compares the UMC $EREG_CALC$ variable with the true photon energy in UMC. The last plot in the second row compares the efficiency of the photon cuts in UMC and data. The cuts are found to be 7.4 % less efficient in data than in UMC.

Parameter	Value
$BR(K_{\mu 2})$	0.635
N_{IB}	1805.2 ± 138.2
$N_{K_{\mu 2}}$	11743
P	20160
$N_{K_{\mu 2}, UMC}$	25512
$N_{K_{\mu 2}, gen}$	2.000×10^5
$N_{IB, gen}$	8.390×10^6
$N_{IB, UMC}$	15686
ϵ_{γ}	0.926
$BR(IB)$	$(3.568 \pm 0.273) \times 10^{-4}$

Table 5.5: IB branching ratio calculation.

IB branching ratio. The number of IB events observed (N_{IB}), is taken from the two-dimensional fitting and the error on the branching ratio is taken solely from the error on N_{IB} . The final IB branching ratio is found to be

$$BR(IB) = (3.568 \pm 0.273) \times 10^{-4}$$

This agrees quite well with the theoretically calculated value of 3.300×10^{-4} , and gives us confidence that the fitting procedure is working well in identifying IB events. If the N_{IB} is taken from the the one-dimensional COSOP fit, one obtains a branching ratio of $(3.225 \pm 0.105) \times 10^{-4}$, which is also in good agreement with the theoretical value.

5.5 Systematic Error

We now wish to estimate the systematic error associated with the measurement of the SD^+ branching ratio. As mentioned above, by normalizing the measurement of the SD^+ branching ratio to that of the well known IB decay, we have removed many possible sources of systematic error. However, significant systematic errors still exist due to inaccurate or incomplete simulation of the detector by UMC and to other uncertainties of the analysis. Typically, these errors arise from uncertainty in a particular input parameter of the analysis. The systematic error associated with this uncertainty is estimated by varying this parameter over an “allowed” range of values and assessing its impact on the measured SD^+ branching ratio. While measuring the slope of the SD^+ branching ratio as a function of the various input parameters is usually straightforward, assigning an allowed range of values is more difficult.

In choosing the parameters to study, an attempt is made to “factor” the analysis into a few sections, each of which has a systematic error which is un-correlated with those of the other sections. The following sections are defined and studied: charged track analysis, photon analysis, background subtraction, and final fitting.

5.5.1 Charged Track

Systematic errors due to the measurement of the charged track could in principle come from a number of sources. These include the energy measurement (ETOT_TR) and

the momentum measurement (PTOT_TR). The kinematic measurements, however, are adjusted so that the $K_{\mu 2}$ and $K_{\pi 2}$ peaks come out in the right place. To first order, then, systematic errors in these measurements are not likely to be serious sources of error in the SD^+ branching ratio.

In contrast, it is not possible to empirically adjust the $K_{\mu\nu\gamma}$ trigger requirement that the charged track stop between RS layers 16 and 20. Rather, when calculating the acceptance of this requirement for a given μ^+ energy, we are strongly dependent on *à priori* knowledge of the the Range Stack counter thickness. The nominal value of this thickness is 1.905 cm, but it carries a significant uncertainty with it which leads to uncertainty in the acceptance for a μ^+ of a given energy. Since the IB and SD^+ decays have different μ^+ energy distributions, this uncertainty can lead to an error in measured SD^+ branching ratio. In fact, in other E787 analyses, this effect has been found to be one of the main sources of uncertainty in the acceptance calculation [29]. We believe that the range counter thickness uncertainty provides the dominant source of systematic error associated with the measurement of the charged track.

Sensitivity to Range Stack Counter Thickness

As a first step in understanding the sensitivity of the measured SD^+ branching ratio to the range counter thickness, it is useful to look at the relative acceptance for different decays as a function of RS counter thickness. We did this by generating

in UMC $K_{\mu 2}$, $K_{\mu\nu\gamma}$ (IB) and $K_{\mu\nu\gamma}$ (SD⁺) events at 14 different values of range counter thickness ranging between 1.85 and 1.98 cm. For the $K_{\mu 2}$ events, the $K_{\mu 2}(1)$ trigger was used and for the two types of $K_{\mu\nu\gamma}$, the $K_{\mu\nu\gamma}$ trigger was used. We then applied the full analysis to each sample. For the $K_{\mu 2}$ events we used the cuts in Table 5.13 and for the $K_{\mu\nu\gamma}$ events we used the cuts in Table 5.8. We then counted the events passing all cuts for each sample and plotted the results normalizing to the value found at 1.90 cm, which is close to the nominal thickness of 1.905 cm. The results of this study for the three samples are shown in Figure 5.12 (a).

We can see that for $K_{\mu 2}(1)$ events, the acceptance goes up strongly as a function of range counter thickness; for SD⁺ events it goes up somewhat slower; and for IB events, slower still. The reason for this can be seen in Figure 5.12 (b) where we see that the stopping layer distribution for $K_{\mu 2}(1)$ events is peaked somewhat beyond layer 20. Therefore, as the counters are made thicker, more events are brought into the accepted stopping region. This effect is weaker for SD⁺ events and weaker still for IB events, although it is still there for both types of decay.

To actually calculate the dependence of the measured SD⁺ branching ratio on the range counter thickness, we again use $K_{\mu\nu\gamma}$ samples generated at the different range counter thicknesses. These samples are used to “manufacture” a combination of IB and SD⁺ components, as in real data, at each of the different thicknesses. The ratio of IB to SD⁺ that we used corresponded to an SD⁺ branching ratio of 1.2×10^{-5} . The

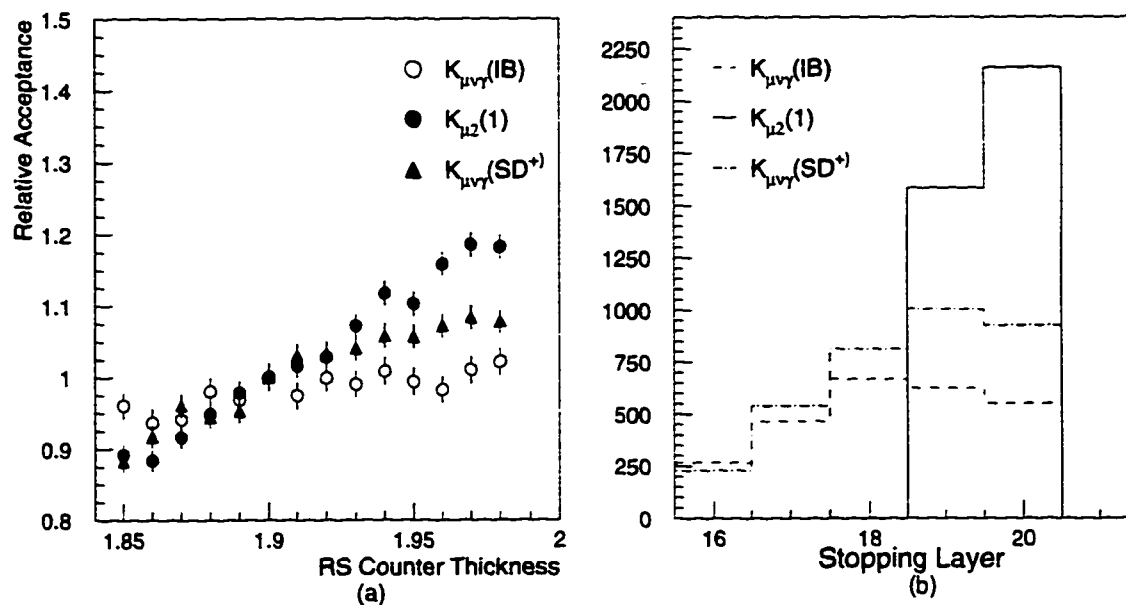


Figure 5.12: Plot (a) shows relative efficiency for three different decay modes as a function of range counter thickness. Plot (b) shows the stopping layer distribution for the three decay modes for a counter thickness of 1.90 cm.

data at each thickness are then fitted using the UMC distributions generated at the nominal thickness of 1.905 cm. The SD^+ branching ratio is then re-calculated at each thickness and the results plotted. This plot is shown in Figure 5.13. The plot gives an estimate of what we would measure for the SD^+ branching ratio using the nominal range counter thickness if the actual range counters were a different thickness. As expected, the measured SD^+ branching ratio grows as the counters become thicker. This is because the acceptance of the SD^+ component is climbing relative to that of the IB component.

A linear fit is performed on the data to find the slope of the dependence. This slope will be combined with the range of counter thickness that is considered possible

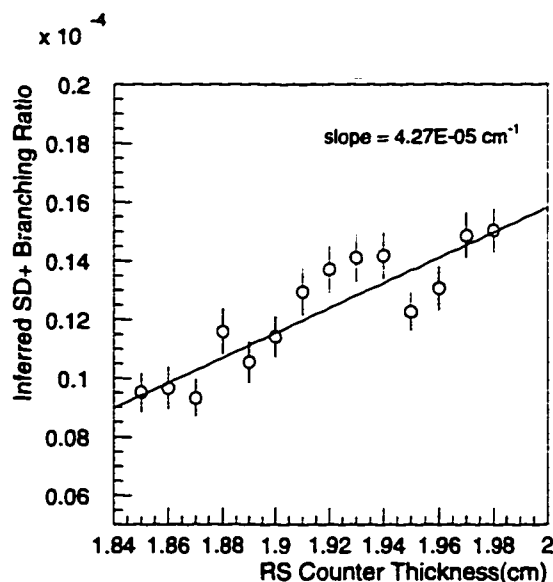


Figure 5.13: Measured SD^+ branching ratio as a function of range counter thickness.

to produce a systematic error associated with this source. This range of possible values of counter thickness will be addressed in the next section.

Allowed Range of Counter Thickness

In previous E787 analyses, the range counter thickness has been assumed to be in the range 1.905 cm to 1.950 cm [29]. These analyses have looked at the stopping layer distribution of $K_{\pi 2}$ and $K_{\mu 2}$ events and tried to match these up with the distributions from UMC data generated at different range counter thicknesses. This effort, however, has been somewhat hampered by the trigger bias inherent in most E787 data. For $K_{\mu 2}$ events, for example, the standard $K_{\mu 2}(1)$ trigger has been used, but this trigger only allows stops in layers 19 through 21, and so does not give a very large “lever

arm" over which to examine the stopping layer distribution.

From the $K_{\mu\nu\gamma}$ trigger, however, we get a source of $K_{\mu 2}$ events in which the stopping layer is allowed to be anywhere in the range from 16 to 20, thereby giving a much better measurement of the stopping layer distribution. These $K_{\mu 2}$ events can be selected with good purity from the $K_{\mu\nu\gamma}$ triggers by simply applying the NOTPROMPT cut along with the fiducial-type cuts. These cuts are shown in Table 5.21. We then generate UMC $K_{\mu 2}$ events at each range counter thickness requiring only a T · A as a trigger. We apply the "fiducial" cuts shown in Table 5.21, including the STLAY cut which imposes the $K_{\mu\nu\gamma}$ trigger requirement of stopping layer 16-20. The stopping layer distribution for the data sample is then compared with that of the UMC samples at several different range counter thicknesses. This is shown in Figure 5.14. From these plots, it is apparent that a range counter thickness of around 1.900 cm is favored.

The radial distribution of the K^+ stopping position in the Target will clearly have some effect on these distributions. While the stopping position distribution is carefully simulated in UMC, it is still a potential problem because the distributions that are used must be corrected for acceptance effects which depend on counter thickness. To address this, the study was repeated with an additional cut requiring that the K^+ stop position be near the center of the Target. Here, the stopping distribution is essentially flat, so the uncertainties of its simulation should be less than for the whole

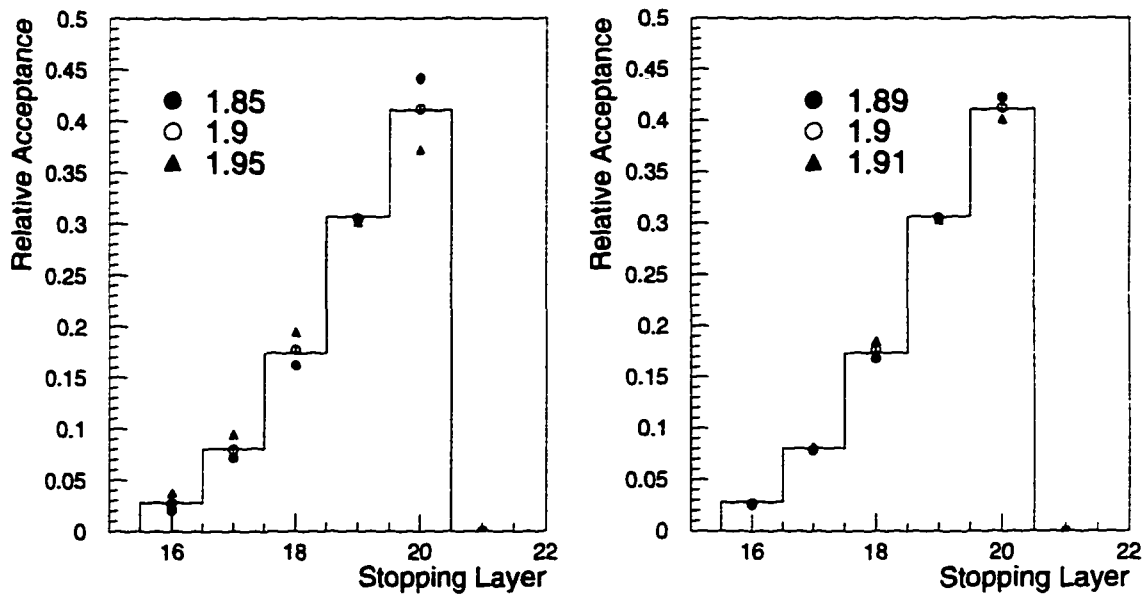


Figure 5.14: Stopping layer distribution for real $K_{\mu 2}$ events compared to UMC generated $K_{\mu 2}$'s at different range counter thicknesses. Solid histogram is data. First plot shows whole range of thicknesses checked. Second narrows down to region around 1.90 cm. All histograms are normalized to unit area.

Target. The cut requires that the distance from the K^+ stopping position to the center of the Target (called TGR) be less than 4 cm. The cut was applied to both the data and the UMC samples and the results are shown in figure 5.15. They are quite consistent with those of the original study.

Assigning an allowed range is not a completely well defined procedure, but a conservative range of ± 0.02 cm is unlikely to be an underestimate. Multiplying this by the slope of the measured SD^+ branching ratio, which in Figure 5.13 was found to be $4.270 \times 10^{-5} \text{ cm}^{-1}$, yields a systematic uncertainty of 0.085×10^{-5} , or 6.4 % of the measured SD^+ branching ratio. This is taken as the total uncertainty from the charged track analysis.

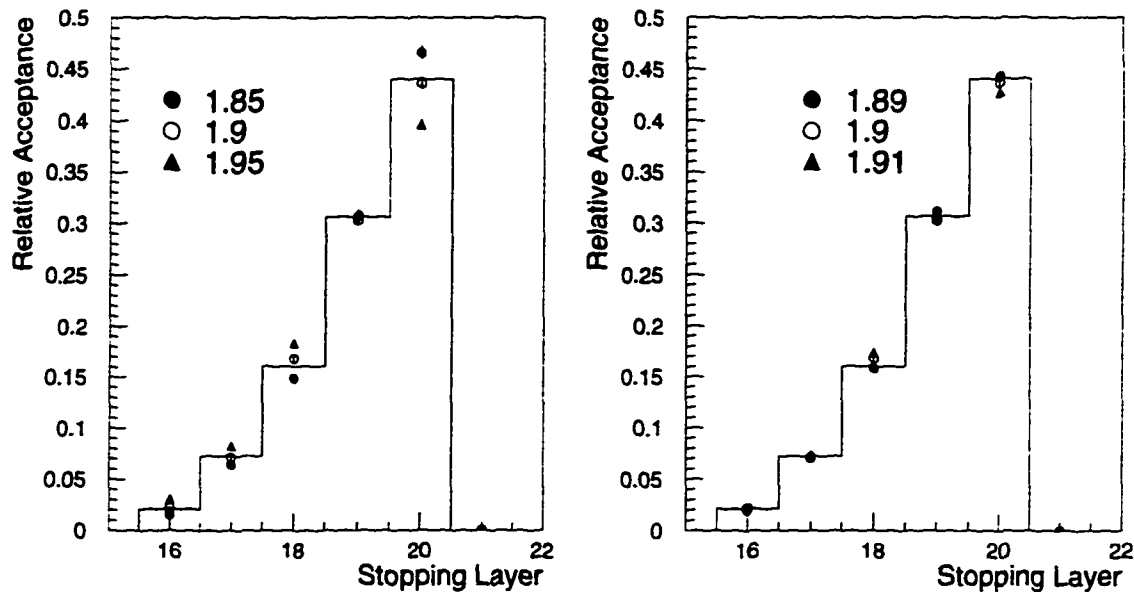


Figure 5.15: Similar plots as in Figure 5.14 but with the additional requirement that the K^+ stop position be near the center of the Target.

5.5.2 Photon Analysis

For the photon analysis, we are concerned with a possible photon-energy-dependent efficiency loss which is not well simulated in UMC. For example, if the analysis were less efficient for photons of high energy than UMC indicates, the result would be to suppress the SD^+ branching ratio relative to that of IB, since its photons tend to be at higher energy. Figure 5.11 indicates that the efficiency of the photon cuts is simulated rather well by UMC, but an independent assessment is still necessary.

While it was possible to identify a single dominant source of error for the charged track analysis, the situation with the analysis of the BV photon is less clear. Since there is no clear single source of disagreement with UMC, we lump all possible sources

all into a single, empirical, photon-energy-dependent disagreement. We will vary this all-encompassing efficiency and measure its effect on the measured SD^+ branching ratio.

Sensitivity to Relative Photon Efficiency

We can simulate a disagreement between real and UMC photon efficiency by randomly cutting events based on the value of `EREG_FIT`. The disagreement is assumed to be linear and to be described by the “shaping parameter” ϵ which is the fractional difference efficiency from one extreme of possible `EREG_FIT` value to the other. For each event a random number between 0 and 1 is generated. If the number lies above the line describing the slope of the efficiency disagreement the event is thrown out. If it lies below the event is kept. This is illustrated in Figure 5.16. In this way, it is possible to “shape” the photon distribution according the parameter ϵ .

To see how this effects the measured SD^+ branching ratio, we apply this shaping function to the data for several different values of ϵ , then redo the two-dimensional fit and recalculate the SD^+ branching ratio. This is shown in Figure 5.17.

Allowed Range of Relative Photon Efficiency

To calculate the allowed range of the ϵ parameter we compare the `EREG_FIT` spectrum of $K_{\pi 2}$ events from UMC with that from data. The $K_{\pi 2}$ samples that are used are the same as those used in the photon efficiency calculation in the IB branching

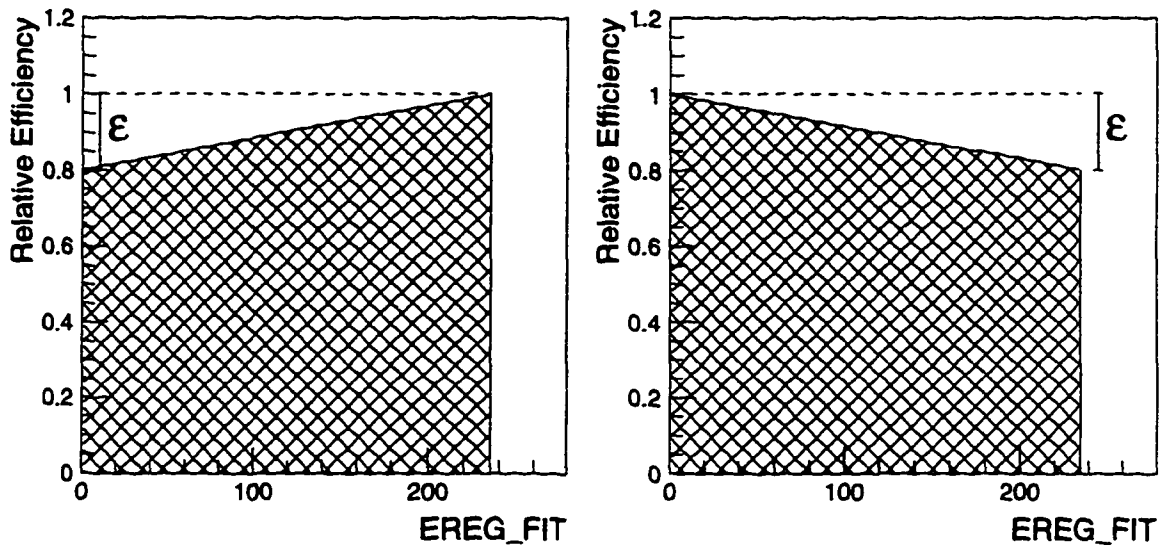


Figure 5.16: Illustration of EREG_RAN technique of simulating a disagreement between UMC and real photon efficiency. The first plot shows the definition of ϵ for positive values and the second shows it for negative values.

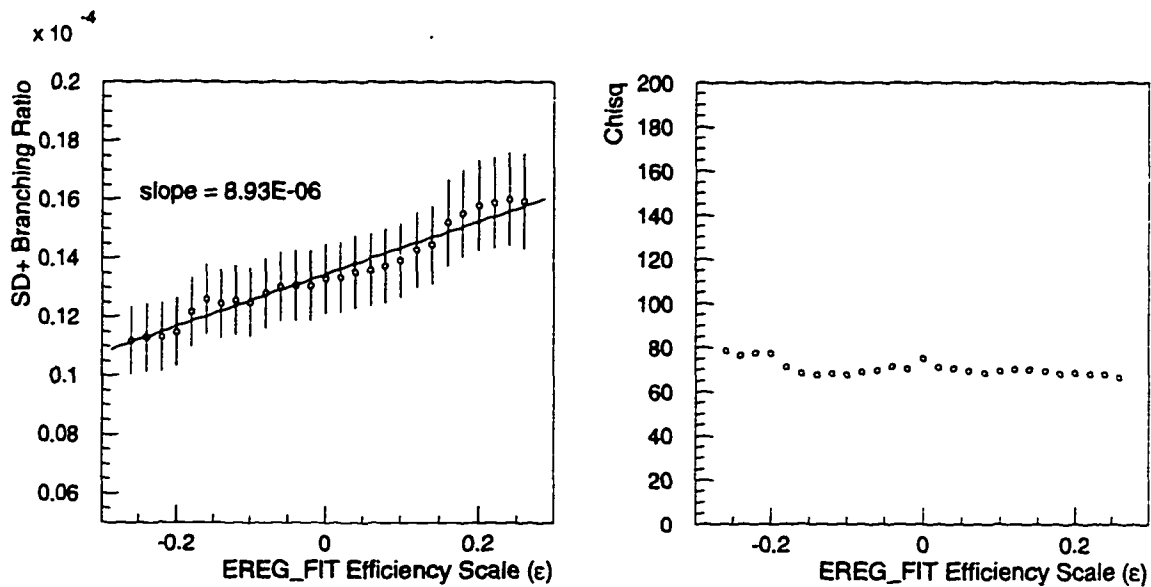


Figure 5.17: The first plot shows the measured SD^+ branching ratio as a function of the photon spectrum shaping parameter ϵ . The second shows the χ^2 of the fit to the spectrum as a function of ϵ .

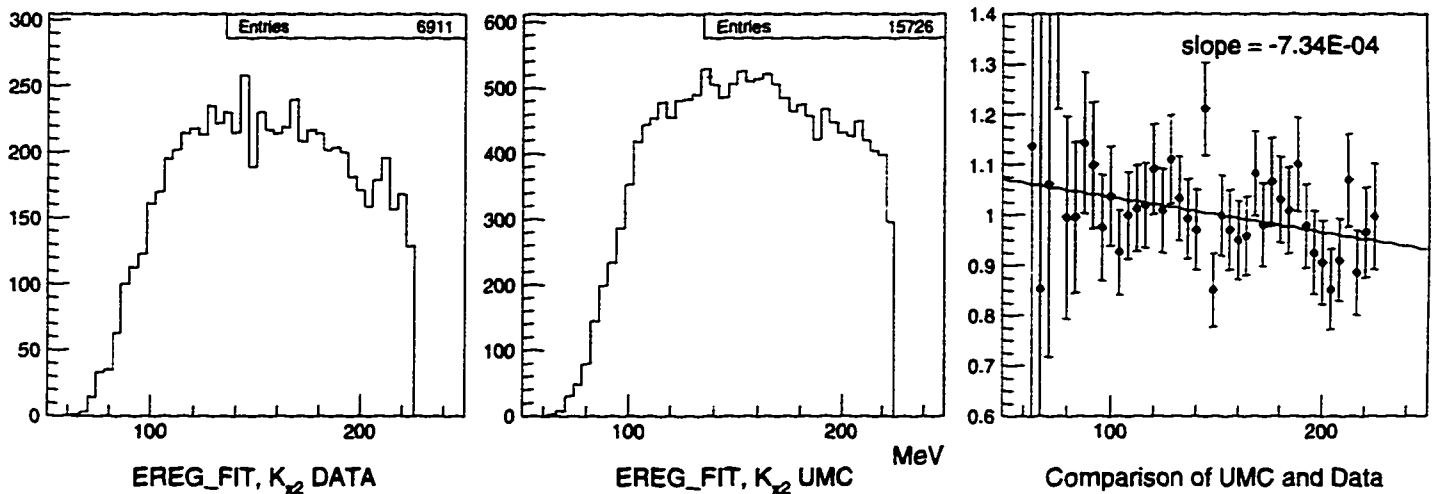


Figure 5.18: Estimation of ϵ parameter. EREG.FIT is plotted for $K_{\pi 2}$ events in data and in UMC. The third plot is the normalized data histogram divided by the normalized UMC histogram.

ratio calculation. The cut tables are shown in Tables 5.19 and 5.20. The EREG.FIT distributions for both data sets are plotted and normalized and a plot is made of the ratio of the data to UMC in each bin. A fit of this plot measures the slope of the disagreement between data and UMC. This is shown in Figure 5.18. There is a downward slope in the third plot indicating that the data falls off faster than UMC as the photon energy is increased. The slope is $-7.340 \times 10^{-4} \text{ MeV}^{-1}$, which corresponds to an ϵ value of 0.172. Multiplying this by the slope of the dependence in Figure 5.17 of 8.932×10^{-6} gives a systematic uncertainty due to this source of 1.54×10^{-6} , or 11.6 % of the measured SD^+ branching ratio.

5.5.3 Background Subtraction

The subtraction of the background involves two possible sources of error: the first is the statistical error in the background distributions and the second is any error in the weight by which the background spectrum is multiplied before being subtracted from the raw spectrum. The first type of error is accounted for by adjusting the error of each bin appropriately as described in Section 5.1. The second type, however, has not yet been accounted for. The calculation of the weight for each type of background certainly has statistical errors and may also have significant systematic error. To assess the effect that these errors can have on the SD^+ branching ratio, we use the same technique as for the other error sources — we find the sensitivity of the measured SD^+ branching ratio to each background's weight, and then define a possible range that the weight could fall into.

As we saw in the mis-tagging checks of the background studies, a significant number of the events in the final background spectra are actually mis-tagged $K_{\mu\nu\gamma}$ events. This was particularly important in the case of Overlap study where the expected number of mis-tagged $K_{\mu\nu\gamma}$ events was 11.4 and the number of events in background sample was 13. One might suggest, then, that the range of weights allowed should be very large to account for the effect of mis-tagging. The mis-tagging, however, does not cause a systematic error, because the mis-tagged events are drawn from the *same* distribution as the signal events. The effect is the same as throwing

out random events of the $K^+ \rightarrow \mu^+ \nu_\mu \gamma$ spectrum which, on average, cannot effect the measured the SD^+ branching ratio. It is only the *real* background events, i.e. those coming from a source other than $K_{\mu\nu\gamma}$ that can effect the result and it is the effect of those that we are checking in the study of the background normalizations. So, in calculating the range of background weights allowed, we will not be concerned with the possibility that many of the events in the background spectra are actually mis-tagged $K_{\mu\nu\gamma}$ events.

Sensitivity to Background Weights

For each background source, the corresponding weight is scaled by a factor ranging from zero to two. The background subtraction is then performed using this new weight, while keeping the weights for the other backgrounds at their nominal values. The two-dimensional fit is then re-done using this new background-subtracted spectrum and the and the SD^+ branching ratio recalculated. The results of this procedure for the three types of background are shown in Figure 5.19. Varying the weight of the accidental background study has by far the largest effect on the measured SD^+ branching ratio.

Allowed Ranges of Background Weights

As can be seen in Figure 5.19 the the slope of the dependence on the background weight for the No Overlap and Overlap background studies is very small. It almost

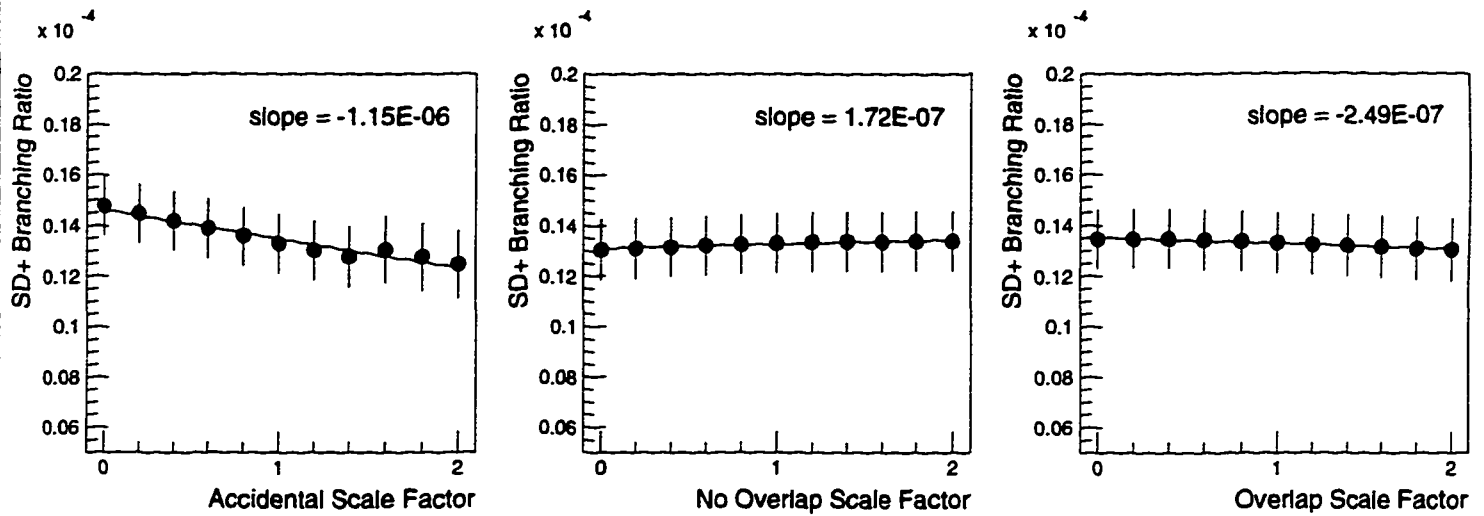


Figure 5.19: Sensitivity of measured SD^+ branching ratio to background weights.

does not matter what range we choose for the weight since the error will be negligibly small regardless. We take the allowed range to be equal to the fractional statistical error of the normalization, N_R/N_ϵ . This is calculated as

$$\begin{aligned}\sigma_{N_R/N_\epsilon}^2 &= \left(\frac{\sigma_{N_R}}{N_R}\right)^2 + \left(\frac{\sigma_{N_\epsilon}}{N_\epsilon}\right)^2 \\ &= \left(\frac{1}{N_R}\right) + \left(\frac{1}{N_\epsilon}\right)\end{aligned}$$

The statistical error on the No Overlap weight is 7.0 %, and for the Overlap weight is 10.3 %. Multiplying these by the appropriate slopes we get an error from No Overlap of 1.21×10^{-8} and from Overlap 2.58×10^{-8} , or 0.1 % and 0.2 % of the measured SD^+ branching ratio, respectively.

For the Accidental background, on the other hand, the slope is larger and it is possible that a significant error could be produced. Fortunately, the accidental weight

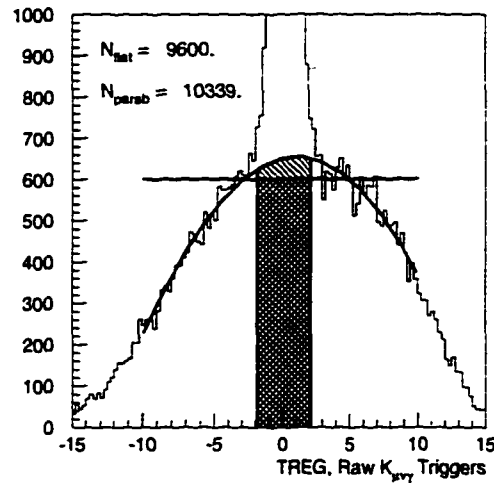


Figure 5.20: Systematic error associated with calculation of Accidental background weight. Expected number of accidental events in the prompt (hatched) region is calculated using a flat and parabolic extrapolation.

is the one in which we have the most confidence, since it just comes from looking at the “side-bands” of the photon time distribution. In the Accidental background study, we had assumed that this distribution was flat and calculated the number of accidental events expected in the prompt region. This was shown in Figure 4.5. To get an idea of the size of the systematic error associated with this, we can instead fit a parabola to the distribution outside of the prompt region and use that to calculate to the number of events in the prompt region. This is shown in figure 5.20. The difference between the two methods is 8% and we take this as the systematic uncertainty of this calculation. Multiplying this by the slope seen in Figure 5.19, we get an error due to the accidental background subtraction of 9.20×10^{-8} , or 0.7 % of the measured SD^+ branching ratio.

ETOT_TR size	EREG_FIT size	BR(SD ⁺)	χ^2 / DOF
3 MeV	20 MeV	1.331×10^{-5}	75.1/69
2 MeV	15 MeV	1.218×10^{-5}	137/123
3 MeV	15 MeV	1.232×10^{-5}	92.9/90
3 MeV	30 MeV	1.304×10^{-5}	54.5/49
2 MeV	30 MeV	1.255×10^{-5}	81.0/68
2 MeV	20 MeV	1.327×10^{-5}	99.5/96

Table 5.6: Measured SD⁺ branching ratio for several different choices of binning of the final EREG_FIT vs. ETOT_TR histogram. The top entry is the nominal binning used in the branching ratio calculation.

5.5.4 Binning

The choice of the binning used in the final plot of EREG_FIT vs. ETOT_TR is somewhat arbitrary. One wants to choose the bins small enough so that the different $K_{\mu\nu\gamma}$ components can be distinguished, yet large enough so that the number of events in each bin is not small. The particular choice that was used in the fit had ETOT_TR bins of 3 MeV and EREG_FIT bins of 20 MeV. To see if the choice of binning had a large effect on the measured branching ratio, a number of other binnings were tried. For all histograms the range of ETOT_TR was between 132 MeV and 162 MeV and for EREG_FIT was between 0 and 300 MeV. The results of this are shown in Table 5.6.

To assess a systematic error to the effect of different choices of binning, we take the RMS of the different measured branching ratios and identify that as the error. This comes out to be 4.93×10^{-7} , or 3.7 % of the measured SD⁺ branching ratio.

While much of this error is probably already accounted for as statistical error, we conservatively include it as a separate systematic error.

5.5.5 Photon Energy Cutoff

Another somewhat arbitrary parameter of the analysis is the minimum photon energy EREG that is accepted in the analysis. EREG was required to be greater than 90 MeV by the EREG_FIN cut. This choice of threshold was motivated by the desire for the trigger photon requirement BVHI to be fully efficient. While it is difficult to lower the minimum value of EREG since that would require simulating the BVHI trigger bit, it is quite easy to raise it.

The procedure, then, is to set the EREG_FIN cut value at a particular value and apply this to all of the samples — including the raw data, the background samples and all the UMC $K_{\mu\nu\gamma}$ component samples. The two-dimensional fitting is then re-applied and the SD^+ branching ratio is recalculated. The results of this are shown in Figure 5.21

As we raise the EREG_FIN cut, we are radically changing the relative sizes of the SD^+ and IB components. At 90 MeV, there is roughly twice as much IB as SD^+ in the final sample, whereas at 150 MeV, there is 30% more SD^+ than IB. Nonetheless, the fitting procedure still returns consistent values of the SD^+ branching ratio. Since there is no apparent systematic effect on the SD^+ branching ratio, no systematic error

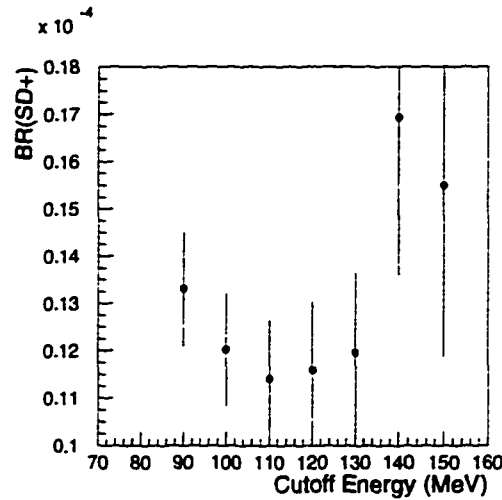


Figure 5.21: Measured SD^+ branching ratio using a number of different values for the minimum value of EREG. Note the suppressed zero of the y -axis.

is associated with this effect and it is presented solely as a check of the stability of the analysis.

5.5.6 Summary of Systematic Errors

Table 5.7 summarizes the sources and magnitudes of the systematic errors that were studied. The table shows the slope of the dependence of each error source on the parameter describing it, the range allowed of the parameter and the total error coming from each source.

The total systematic error from all sources added in quadrature is 1.831×10^{-6} or 13.8 % of the SD^+ branching ratio. This is to be compared with the statistical error which 1.242×10^{-6} .

The systematic error is dominated by the error due to the photon analysis. This

Error Source	Parameter	Slope	Range	BR(SD ⁺) Error
RS Counters	thickness	4.270×10^{-5}	± 0.02 cm	0.085×10^{-5}
Photon Analysis	ϵ	8.932×10^{-6}	± 0.172	0.154×10^{-5}
ACC Bkg Sub	scale factor	-1.150×10^{-6}	± 0.08	0.009×10^{-5}
NOV Bkg Sub	scale factor	1.718×10^{-7}	± 0.0705	0.001×10^{-5}
OV Bkg Sub	scale factor	-2.492×10^{-7}	± 0.1034	0.003×10^{-5}
Binning	-	-	-	0.049×10^{-5}
Total Error Added in Quadrature				0.183×10^{-5}

Table 5.7: Summary of systematic errors.

error came out somewhat large because of the poor agreement of the shape of the EREG.FIT spectrum from $K_{\pi 2}$ events in data and in UMC. It is possible that this agreement can be made better with further study and the error associated with it reduced. Another possibility is to use EREG vs. ETOT_TR as the final fitting histogram rather than EREG.FIT vs ETOT_TR. The EREG spectrum in $K_{\pi 2}$ seems to be better reproduced in UMC and so the systematic error would likely be lower. Due to the poorer resolution of the EREG measurement of photon energy, and the resultant poorer separation between IB and SD⁺ the statistical error would be somewhat higher.

5.6 Conclusion

The final result for the SD⁺ branching ratio is

$$BR(SD^+) = (1.331 \pm 0.120 \pm 0.183) \times 10^{-5}$$

where the first error is statistical and the second systematic. This corresponds to a measurement of $|F_V + F_A|$ of

$$|F_V + F_A| = 0.165 \pm 0.007 \pm 0.011$$

We are also able to set a 90 % confidence level limit on the value of $F_V - F_A$ which is

$$-0.25 < F_V - F_A < 0.07$$

5.7 Detailed Cut Lists

Cut Name	Events In	Events Out	Rejection
ISKCODE	1517733	1419715	1.069
TRS	1419715	1370388	1.036
COS3D	1370388	1274084	1.076
TGZ	1274084	1238784	1.028
ETGT	1238784	1151716	1.076
EIC	1151716	1115115	1.033
PHO_CHISQ	1115115	934246	1.194
PRB.COM	934246	829526	1.126
BW1TRS	829526	612378	1.355
BW2TRS	612378	595926	1.028
RSIN	595926	529703	1.125
ECIN	529703	470802	1.125
BVIN	470802	444290	1.060
ICIN	444290	433492	1.025
VCIN	433492	431124	1.005
INTIME2	431124	391165	1.102
RDPE_EXCL	391165	389465	1.004
ETGPHO	389465	380782	1.023
EREG	380782	377954	1.007
PROMPT	377954	99796	3.787
FRACL	99796	43910	2.273
PRB_TU5	43910	33620	1.306
ZREG	33620	25377	1.325
PRB_MGN	25377	17388	1.459
STLAY	17388	17372	1.001
EREG_FIN	17372	13127	1.323
SPEC14	13127	2693	4.874

Table 5.8: Cuts applied to produce final sample. The last two cuts are the final spectrum cuts in the photon energy EREG and the muon energy ETOT_TR.

Cut Name	Events In	Events Out	Rejection
ISKCODE	142482	142327	1.001
TRS	142327	142327	1.000
COS3D	142327	140142	1.016
TGZ	140142	137092	1.022
ETGT	137092	128722	1.065
EIC	128722	128187	1.004
PHO_CHISQ	128187	125734	1.020
PRB_COM	125734	124304	1.012
BW1TRS	124304	124304	1.000
BW2TRS	124304	124304	1.000
RSIN	124304	120920	1.028
ECIN	120920	120754	1.001
BVIN	120754	115941	1.042
ICIN	115941	115837	1.001
VCIN	115837	115659	1.002
INTIME2	115659	115643	1.000
RDPE_EXCL	115643	115228	1.004
ETGPHO	115228	113059	1.019
EREG	113059	113059	1.000
PROMPT	113059	113052	1.000
FRACL	113052	95816	1.180
PRB_TU5	95816	95367	1.005
ZREG	95367	89822	1.062
PRB_MGN	89822	85602	1.049
STLAY	85602	85446	1.002
EREG_FIN	85446	52585	1.625
SPEC14	52585	15686	3.352

Table 5.9: Cuts applied to produce final UMC IB spectrum.

Cut Name	Events In	Events Out	Rejection
ISKCODE	19343	19319	1.001
TRS	19319	19319	1.000
COS3D	19319	18955	1.019
TGZ	18955	18529	1.023
ETGT	18529	17934	1.033
EIC	17934	17845	1.005
PHO_CHISQ	17845	17502	1.020
PRB_COM	17502	17315	1.011
BW1TRS	17315	17315	1.000
BW2TRS	17315	17315	1.000
RSIN	17315	16685	1.038
ECIN	16685	16664	1.001
BVIN	16664	16198	1.029
ICIN	16198	16181	1.001
VCIN	16181	16153	1.002
INTIME2	16153	16149	1.000
RDPE_EXCL	16149	16100	1.003
ETGPHO	16100	15807	1.019
EREG	15807	15807	1.000
PROMPT	15807	15806	1.000
FRACL	15806	14942	1.058
PRB_TU5	14942	14862	1.005
ZREG	14862	14327	1.037
PRB_MGN	14327	13453	1.065
STLAY	13453	13447	1.000
EREG_FIN	13447	12656	1.062
SPEC14	12656	7601	1.665

Table 5.10: Cuts applied to produce final UMC SD^+ spectrum.

Cut Name	Events In	Events Out	Rejection
ISKCODE	26536	26276	1.010
TRS	26276	26276	1.000
COS3D	26276	25913	1.014
TGZ	25913	25326	1.023
ETGT	25326	23819	1.063
EIC	23819	23715	1.004
PHO_CHISQ	23715	23270	1.019
PRB_COM	23270	23008	1.011
BW1TRS	23008	23008	1.000
BW2TRS	23008	23008	1.000
RSIN	23008	22198	1.036
ECIN	22198	22158	1.002
BVIN	22158	21446	1.033
ICIN	21446	21426	1.001
VCIN	21426	21396	1.001
INTIME2	21396	21395	1.000
RDPE_EXCL	21395	21317	1.004
ETGPHO	21317	20940	1.018
EREG	20940	20940	1.000
PROMPT	20940	20940	1.000
FRACL	20940	19098	1.096
PRB_TU5	19098	19002	1.005
ZREG	19002	18136	1.048
PRB_MGN	18136	16923	1.072
STLAY	16923	16895	1.002
EREG_FIN	16895	14479	1.167
SPEC14	14479	4339	3.337

Table 5.11: Cuts applied to produce final UMC INT⁻ spectrum.

Cut Name	Events In	Events Out	Rejection
ISKCODE	50003	49921	1.002
TRS	49921	49921	1.000
COS3D	49921	49148	1.016
TGZ	49148	47957	1.025
ETGT	47957	45382	1.057
EIC	45382	45188	1.004
PHO_CHISQ	45188	44342	1.019
PRB_COM	44342	43830	1.012
BW1TRS	43830	43830	1.000
BW2TRS	43830	43830	1.000
RSIN	43830	42506	1.031
ECIN	42506	42440	1.002
BVIN	42440	40875	1.038
ICIN	40875	40852	1.001
VCIN	40852	40787	1.002
INTIME2	40787	40780	1.000
RDPE_EXCL	40780	40635	1.004
ETGPHO	40635	39879	1.019
EREG	39879	39879	1.000
PROMPT	39879	39874	1.000
FRACL	39874	34891	1.143
PRB_TU5	34891	34732	1.005
ZREG	34732	32820	1.058
PRB_MGN	32820	31046	1.057
STLAY	31046	30998	1.002
EREG_FIN	30998	23263	1.333
SPEC14	23263	7491	3.105

Table 5.12: Cuts applied to produce final UMC INT⁺ spectrum.

Cut Name	Events In	Events Out	Rejection
ISKCODE	95115	86814	1.096
DELCO	86814	55767	1.557
STLAY_KM2	55767	20480	2.723
TRS	20480	19708	1.039
COS3D	19708	18702	1.054
TGZ	18702	18203	1.027
ETGT	18203	17816	1.022
EIC	17816	17524	1.017
PHO_CHISQ	17524	16517	1.061
PRB_COM	16517	16186	1.020
BW1TRS	16186	14808	1.093
BW2TRS	14808	14518	1.020
GAM_TRIG	14518	14077	1.031
BVTRIG	14077	13997	1.006
RSIN	13997	13667	1.024
ECIN	13667	12767	1.070
BVIN	12767	12767	1.000
ICIN	12767	12654	1.009
VCIN	12654	12647	1.001
BVPE_ER	12647	12620	1.002
BVPE2_ER	12620	12610	1.001
INTIME2	12610	11814	1.067
RDPE_EXCL	11814	11811	1.000
ETGPHO	11811	11743	1.006

Table 5.13: Cuts applied to $K_{\mu 2}(1)$ monitors. The result is $N_{K_{\mu 2}}$.

Cut Name	Events In	Events Out	Rejection
ISKCODE	74219	74147	1.001
DELCO	74147	74147	1.000
STLAY_KM2	74147	29488	2.514
TRS	29488	29488	1.000
COS3D	29488	28150	1.048
TGZ	28150	27495	1.024
ETGT	27495	27114	1.014
EIC	27114	26931	1.007
PHO_CHISQ	26931	26287	1.024
PRB_COM	26287	26059	1.009
BW1TRS	26059	26059	1.000
BW2TRS	26059	26059	1.000
GAM_TRIG	26059	26059	1.000
BVTRIG	26059	26059	1.000
RSIN	26059	26056	1.000
ECIN	26056	26056	1.000
BVIN	26056	26056	1.000
ICIN	26056	26056	1.000
VCIN	26056	26010	1.002
BVPE_ER	26010	26010	1.000
BVPE2_ER	26010	26010	1.000
INTIME2	26010	26010	1.000
RDPE_EXCL	26010	26010	1.000
ETGPHO	26010	25512	1.020

Table 5.14: Cuts applied to UMC $K_{\mu 2}$ events that passed the $K_{\mu 2}(1)$ trigger. The result is $N_{K_{\mu 2}, UMC}$.

Cut Name	Events In	Events Out	Rejection
ISKCODE	34304	32948	1.041
EREG	32948	28651	1.150
PROMPT	28651	27698	1.034
RSIN	27698	21665	1.278
RDPE_EXCL	21665	21321	1.016
EIC	21321	20769	1.027
ETGT	20769	19484	1.066
PTOT_KPI2	19484	18282	1.066
PRB_COM	18282	17394	1.051

Table 5.15: Cuts applied to $K_{\pi_2}(2)$ monitor triggers for the photon efficiency check.

Cut Name	Events In	Events Out	Rejection
ISKCODE	173016	167237	1.035
EREG	167237	155350	1.077
PROMPT	155350	154597	1.005
RSIN	154597	53023	2.916
RDPE_EXCL	53023	40609	1.306
EIC	40609	40208	1.010
ETGT	40208	38756	1.037
PTOT_KPI2	38756	37088	1.045
PRB_COM	37088	35018	1.059

Table 5.16: Cuts applied to UMC K_{π_2} events that passed the $K_{\pi_2}(1)$ trigger for the photon efficiency check.

Cut Name	Events In	Events Out	Rejection
ISKCODE	17394	17394	1.000
EREG2	17394	6926	2.511

Table 5.17: Effect of EREG2 cut on K_{π_2} sample in data.

Cut Name	Events In	Events Out	Rejection
ISKCODE	35018	35018	1.000
EREG2	35018	14630	2.394

Table 5.18: Effect of EREG2 cut on K_{π^2} sample in UMC.

Cut Name	Events In	Events Out	Rejection
EREG	6926	6926	1.000
PROMPT	6926	6926	1.000
FRACL	6926	6556	1.056
PRB_TU5	6556	6223	1.054
ZREG	6223	5927	1.050
PRB_MGN	5927	5339	1.110
EREG_FIN	5339	5320	1.004
BVHI	5320	5309	1.002

Table 5.19: Effect of all photon cuts on K_{π^2} sample in data.

Cut Name	Events In	Events Out	Rejection
EREG	14630	14630	1.000
PROMPT	14630	14630	1.000
FRACL	14630	14011	1.044
PRB_TU5	14011	13913	1.007
ZREG	13913	13328	1.044
PRB_MGN	13328	12261	1.087
EREG_FIN	12261	12229	1.003
BVHI	12229	12229	1.000

Table 5.20: Effect of all photon cuts on K_{π^2} sample in UMC.

Cut Name	Events In	Events Out	Rejection
ISKCODE	95461	89495	1.067
EREG	89495	89005	1.006
TRS	89005	86051	1.034
COS3D	86051	80101	1.074
TGZ	80101	78004	1.027
ETGT	78004	72766	1.072
EIC	72766	70516	1.032
STLAY	70516	68037	1.036
NOTPROMPT	68037	33243	2.047

Table 5.21: Cuts applied to $K_{\mu\nu\gamma}$ data as part of range counter thickness study.

Bibliography

- [1] S.L. Glashow, J. Iliopoulos and L. Maiani, *Physical Review* **D2**, 1285 (1970).
- [2] M.S. Atiya *et al.*, *Nucl. Instrum. Methods* **321**, 129 (1992).
- [3] S. Adler *et al.*, *Phys. Rev. Lett.* **76**, 1421 (1996).
- [4] M. Ardebili, *Measurement of the $K^+ \rightarrow \pi^+ \mu^+ \mu^-$ Branching Ratio*, Princeton University *PhD* thesis, 1995.
- [5] M. A. Selen, *Hunting for the Rare Decay $K^+ \rightarrow \pi^+ \mu^+ \mu^-$* , Princeton University *PhD* thesis, 1989.
- [6] *Weak interactions of leptons and quarks*, E.D. Commins and P.H. Bucksbaum, Cambridge University Press (1983).
- [7] *Quarks and Leptons, An Introductory Course in Modern Particle Physics*, F. Halzen and Alan D. Martin, John Wiley & Sons (1984).
- [8] Review of Particle Properties, *Physical Review* **D 50, Part 1**, 1994 (.)

- [9] D.A. Bryman *et al.*, Physics Reports **88**, 151 (1982).
- [10] P. De Baenst and J. Pestieau, Il Nuovo Cimento **53A**, 407 (1968).
- [11] Y. Akiba *et al.*, Physical Review D **32**, 2911 (1985).
- [12] J. Bijnens, G. Ecker and J. Gasser, Nuclear Physics **B 396**, 81 (1993).
- [13] Ll. Ametller, J. Bijnens, A. Bramon and F. Cornet, Physics Letters **B303**, 140 (1993).
- [14] J. Bijnens, Personal Communication
- [15] V.S. Demidov *et al.*, Soviet Journal of Nuclear Physics **52**, 1006 (1990).
- [16] J. Heintze *et al.*, Nuclear Physics **B 149**, 365 (1979).
- [17] Heard *et al.*, Physics Letters **55 B**, 324 (1975).
- [18] J. Roy, *Search for the Rare Kaon Decay $K^+ \rightarrow \pi^+ \nu \bar{\nu}$* , University of British Columbia *PhD* thesis, 1994.
- [19] D. Akerib, *A Search for the Rare Decay $K^+ \rightarrow \pi^+ \nu \bar{\nu}$* , Princeton University *PhD* thesis, 1994.
- [20] E787 Technical Note 318: Central Tracking Chamber with Inflated Cathode-strip Foils, E.W. Blackmore, *et al.*, 15 August, 1996, To be published in Nuclear Instruments and Methods.

- [21] I-H. Chiang *et al.*, *Proceedings of the Fifth International Conference on Calorimetry in High Energy Physics*, World Scientific, (1995), pg. 103.
- [22] M. Burke *et al.*, *Conference Record of the Eighth Conference on Real-Time Computer Applications in Nuclear, Particle, and Plasma Physics*, (1993), pg. 361-4.
- [23] W.Ralph Nelson, H. Hirayama and David W.O. Rogers, *The EGS4 Code System*, SLAC-0265, (1985).
- [24] E787 Technical Note 228: Target Tracking Using the Drift Chamber Trajectory, Mehran Ardebili, Dan Marlow, Peter Meyers, January 2, 1992.
- [25] E787 Technical Note 310: A First Measurement of the $\pi\gamma\gamma(2)$ Branching Ratio, Takashi Nakano, Richard Soluk, February 19, 1996.
- [26] *Probability and Statistics in Particle Physics*, A.G. Frodesen, O. Skjeggstad, and H. Tøfte, Universitetsforlaget, Bergen, Norway, 1979.
- [27] E787 Technical Note 309: KINFIT: A Program for Non-Linear Least-Squares Fitting with Constraints, Mark M. Ito, November 15, 1995.
- [28] MINUIT Function Minimization and Error Analysis, CERN Program Library Long Writeup D506, 1994.
- [29] R. A. McPherson, *Chasing the Rare Decay $K^+ \rightarrow \pi^+ \nu \bar{\nu}$* , Princeton University *PhD* thesis, 1995.